

1

²A SEARCH FOR LONG-LIVED, CHARGED, SUPERSYMMETRIC PARTICLES
³USING IONIZATION WITH THE ATLAS DETECTOR

4

BRADLEY AXEN

5

September 2016 – Version 0.39

6



⁸ Bradley Axen: *A Search for Long-Lived, Charged, Supersymmetric Particles using*
⁹ *Ionization with the ATLAS Detector*, Subtitle, © September 2016

10

Usually a quotation.

11

Dedicated to.

₁₂ ABSTRACT

₁₃ How to write a good abstract:

₁₄ <https://plg.uwaterloo.ca/~migod/research/beck00PSLA.html>

₁₅ PUBLICATIONS

₁₆ Some ideas and figures have appeared previously in the following publications:

₁₇

₁₈ Put your publications from the thesis here. The packages `multibib` or `bibtopic`
₁₉ etc. can be used to handle multiple different bibliographies in your document.

²¹ ACKNOWLEDGEMENTS

²² Put your acknowledgements here.

²³

²⁴ And potentially a second round.

²⁵

26 CONTENTS

27	I	INTRODUCTION	1
28	1	INTRODUCTION	3
29	II	THEORETICAL CONTEXT	5
30	2	STANDARD MODEL	7
31	2.1	Particles	7
32	2.2	Interactions	8
33	2.3	Limitations	8
34	3	SUPERSYMMETRY	9
35	3.1	Motivation	9
36	3.2	Structure	9
37	3.3	Phenomenology	9
38	4	LONG-LIVED PARTICLES	11
39	4.1	Mechanisms	11
40	4.1.1	Examples in Supersymmetry	11
41	4.2	Phenomenology	11
42	4.2.1	Disimilarities to Prompt Decays	11
43	4.2.2	Characteristic Signatures	11
44	III	EXPERIMENTAL STRUCTURE AND RECONSTRUCTION	13
45	5	THE LARGE HADRON COLLIDER	15
46	5.1	Injection Chain	16
47	5.2	Design	17
48	5.2.1	Layout	17
49	5.2.2	Magnets	18
50	5.2.3	RF Cavities	19
51	5.2.4	Beam	20
52	5.3	Luminosity Parameters	21
53	5.4	Delivered Luminosity	22
54	6	THE ATLAS DETECTOR	25
55	6.1	Coordinate System	25
56	6.2	Magnetic Field	25
57	6.3	Inner Detector	25
58	6.3.1	Pixel Detector	25
59	6.3.2	Semiconductor Tracker	25
60	6.3.3	Transition Radiation Tracker	25
61	6.4	Calorimetry	25
62	6.4.1	Electromagnetic Calorimeters	25
63	6.4.2	Hadronic Calorimeters	25
64	6.4.3	Forward Calorimeters	25
65	6.5	Muon Spectrometer	25

66	6.6	Trigger	25
67	6.6.1	Trigger Scheme	25
68	6.6.2	Missing Transverse Energy Triggers	25
69	7	EVENT RECONSTRUCTION	27
70	7.1	Tracks and Vertices	27
71	7.1.1	Track Reconstruction	27
72	7.1.2	Vertex Reconstruction	27
73	7.2	Jets	27
74	7.2.1	Topological Clustering	27
75	7.2.2	Jet Energy Scale	27
76	7.2.3	Jet Energy Scale Uncertainties	27
77	7.2.4	Jet Energy Resolution	27
78	7.3	Electrons	27
79	7.3.1	Electron Identification	27
80	7.4	Muons	27
81	7.4.1	Muon Identification	27
82	7.5	Missing Transverse Energy	27
83	IV	CALORIMETER RESPONSE	29
84	8	RESPONSE MEASUREMENT WITH SINGLE HADRONS	31
85	8.1	Dataset and Simulation	32
86	8.1.1	Data Samples	32
87	8.1.2	Simulated Samples	32
88	8.1.3	Event Selection	32
89	8.2	Inclusive Hadron Response	33
90	8.2.1	E/p Distribution	33
91	8.2.2	Zero Fraction	34
92	8.2.3	Neutral Background Subtraction	35
93	8.2.4	Corrected Response	37
94	8.2.5	Additional Studies	39
95	8.3	Identified Particle Response	42
96	8.3.1	Decay Reconstruction	42
97	8.3.2	Identified Response	43
98	8.3.3	Additional Species in Simulation	45
99	8.4	Summary	46
100	9	JET ENERGY RESPONSE AND UNCERTAINTY	49
101	9.1	Motivation	49
102	9.2	Uncertainty Estimate	49
103	9.3	Summary	52
104	V	SEARCH FOR LONG-LIVED PARTICLES	55
105	10	LONG-LIVED PARTICLES IN ATLAS	57
106	10.1	Event Topology	57
107	10.1.1	Detector Interactions	58
108	10.1.2	Lifetime Dependence	59
109	10.2	Simulation	62

110	11	EVENT SELECTION	65
111	11.1	Trigger	66
112	11.2	Kinematics and Isolation	67
113	11.3	Particle Species Rejection	71
114	11.4	Ionization	74
115	11.4.1	Mass Estimation	75
116	11.5	Efficiency	76
117	12	BACKGROUND ESTIMATION	79
118	12.1	Background Sources	79
119	12.2	Prediction Method	80
120	12.3	Validation	81
121	12.3.1	Closure in Simulation	81
122	12.3.2	Validation Region in Data	82
123	13	SYSTEMATIC UNCERTAINTIES AND RESULTS	85
124	13.1	Systematic Uncertainties	85
125	13.1.1	Background Estimate	85
126	13.1.2	Signal Yield	86
127	13.2	Final Yields	92
128	13.3	Cross Sectional Limits	93
129	13.4	Mass Limits	95
130	13.5	Context for Long-Lived Searches	97
131	VI	CONCLUSIONS	101
132	14	SUMMARY AND OUTLOOK	103
133	14.1	Summary	103
134	14.2	Outlook	103
135	VII	APPENDIX	105
136	A	INELASTIC CROSS SECTION	107
137	B	EXPANDED R-HADRON YIELDS AND LIMITS	109
138		BIBLIOGRAPHY	115

139 LIST OF FIGURES

140	Figure 1	The particle content of the Standard Model (SM)	8
141	Figure 2	The four collision points and corresponding experiments of the Large Hadron Collider (LHC). The image includes the location of the nearby city of Geneva as well as the border of France and Switzerland.	16
142			
143			
144			
145	Figure 3	The accelerator complex that builds up to the full design energies at the LHC . The protons are passed in order to Linac 2, the PSB , the PS , the SPS and then the LHC	16
146			
147			
148			
149	Figure 4	A schematic of the layout of the LHC , not to scale. The arched and straight sections are illustrated at the bottom of the schematic, and all four crossing sites are indicated with their respective experiments.	18
150			
151			
152			
153	Figure 5	A cross section of the the cryodipole magnets which bend the flight path of protons around the circumference of the LHC . The diagram includes both the superconducting coils which produce the magnetic field and the structural elements which keep the magnets precisely aligned.	19
154			
155			
156			
157			
158			
159	Figure 6	The arrangement of four radiofrequency (RF) cavities within a cryomodule.	20
160			
161	Figure 7	The cumulative luminosity versus time delivered to ATLAS (green), recorded by ATLAS (yellow), and certified to be good quality data (blue) during stable beams for pp collisions at 13 TeV in 2015.	23
162			
163			
164			
165	Figure 8	The luminosity-weighted distribution of the mean number of interactions per crossing for the 2015 pp collision data at 13 TeV.	24
166			
167			
168	Figure 9	An illustration (a) of the E/p variable used throughout this paper. The red energy deposits come from the charged particle targeted for measurement, while the blue energy deposits are from nearby neutral particles and must be subtracted. The same diagram (b) for the neutral-background selection, described in Section 8.2.3.	34
169			
170			
171			
172			
173			
174	Figure 10	The E/p distribution and ratio of simulation to data for isolated tracks with (a) $ \eta < 0.6$ and $1.2 < p/\text{GeV} < 1.8$ and (b) $ \eta < 0.6$ and $2.2 < p/\text{GeV} < 2.8$	34
175			
176			
177	Figure 11	The fraction of tracks as a function (a, b) of momentum, (c, d) of interaction lengths with $E \leq 0$ for tracks with positive (on the left) and negative (on the right) charge.	36
178			
179			
180			

181	Figure 12	$\langle E/p \rangle_{\text{BG}}$ as a function of the track momentum for tracks with (a) $ \eta < 0.6$, (b) $0.6 < \eta < 1.1$, and as a function of the track pseudorapidity for tracks with (c) $1.2 < p/\text{GeV} < 1.8$, (d) $1.8 < p/\text{GeV} < 2.2$	37
182			
183			
184			
185	Figure 13	$\langle E/p \rangle_{\text{COR}}$ as a function of track momentum, for tracks with (a) $ \eta < 0.6$, (b) $0.6 < \eta < 1.1$, (c) $1.8 < \eta < 1.9$, and (d) $1.9 < \eta < 2.3$	38
186			
187			
188	Figure 14	$\langle E/p \rangle_{\text{COR}}$ calculated using LCW-calibrated topological clusters as a function of track momentum for tracks with (a) zero or more associated topological clusters or (b) one or more associated topological clusters.	39
189			
190			
191			
192	Figure 15	Comparison of the $\langle E/p \rangle_{\text{COR}}$ for tracks with (a) less than and (b) greater than 20 hits in the TRT.	40
193			
194	Figure 16	Comparison of the $\langle E/p \rangle_{\text{COR}}$ for (a) positive and (b) negative tracks as a function of track momentum for tracks with $ \eta < 0.6$	40
195			
196			
197	Figure 17	Comparison of the E/p distributions for (a) positive and (b) negative tracks with $0.8 < p/\text{GeV} < 1.2$ and $ \eta < 0.6$, in simulation with the FTFP_BERT and QGSP_BERT physics lists.	41
198			
199			
200			
201	Figure 18	Comparison of the response of the hadronic calorimeter as a function of track momentum (a) at the EM-scale and (b) after the LCW calibration.	41
202			
203			
204	Figure 19	Comparison of the response of the EM calorimeter as a function of track momentum (a) at the EM-scale and (b) with the LCW calibration.	42
205			
206			
207	Figure 20	The reconstructed mass peaks of (a) K_S^0 , (b) Λ , and (c) $\bar{\Lambda}$ candidates.	43
208			
209	Figure 21	The E/p distribution for isolated (a) π^+ , (b) π^- , (c) proton, and (d) anti-proton tracks.	44
210			
211	Figure 22	The fraction of tracks with $E \leq 0$ for identified (a) π^+ and π^- , and (b) proton and anti-proton tracks	44
212			
213	Figure 23	The difference in $\langle E/p \rangle$ between (a) π^+ and π^- (b) p and π^+ , and (c) \bar{p} and π^-	45
214			
215	Figure 24	$\langle E/p \rangle_{\text{COR}}$ as a function of track momentum for (a) π^+ tracks and (b) π^- tracks.	46
216			
217	Figure 25	The ratio of the calorimeter response to single particles of various species to the calorimeter response to π^+ with the physics list FTFP_BERT.	46
218			
219			
220	Figure 26	The spectra of true particles inside anti- k_t , $R = 0.4$ jets with (a) $90 < p_T/\text{GeV} < 100$, (b) $400 < p_T/\text{GeV} < 500$, and (c) $1800 < p_T/\text{GeV} < 2300$	50
221			
222			
223	Figure 27	The jet energy scale (<a>JES) uncertainty contributions, as well as the total <a>JES uncertainty, as a function of jet p_T for (a) $ \eta < 0.6$ and (b) $0.6 < \eta < 1.1$	52
224			
225			

226	Figure 28	The JES correlations as a function of jet p_T and $ \eta $ for jets in the central region of the detector.	53
227			
228	Figure 29	A schematic diagram of an R-Hadron event with a lifetime around 0.01 ns. The diagram includes one charged R-Hadron (solid blue), one neutral R-Hadron (dashed blue), Lightest Supersymmetric Particles (LSPs) (dashed green) and charged hadrons (solid orange). The pixel detector, calorimeters, and muon system are illustrated but not to scale.	59
229			
230			
231			
232			
233			
234			
235	Figure 30	A schematic diagram of an R-Hadron event with a lifetime around 4 ns. The diagram includes one charged R-Hadron (solid blue), one neutral R-Hadron (dashed blue), LSPs (dashed green) and a charged hadron (solid orange). The pixel detector, calorimeters, and muon system are illustrated but not to scale.	60
236			
237			
238			
239			
240			
241	Figure 31	A schematic diagram of an R-Hadron event with a lifetime around 5 ns. The diagram includes one charged R-Hadron (solid blue), one neutral R-Hadron (dashed blue), LSPs (dashed green) and charged hadrons (solid orange). The pixel detector, calorimeters, and muon system are illustrated but not to scale.	61
242			
243			
244			
245			
246			
247	Figure 32	A schematic diagram of an R-Hadron event with a lifetime around 20 ns. The diagram includes one charged R-Hadron (solid blue), one neutral R-Hadron (dashed blue), LSPs (dashed green) and charged hadrons (solid orange). The pixel detector, calorimeters, and muon system are illustrated but not to scale.	61
248			
249			
250			
251			
252			
253	Figure 33	A schematic diagram of an R-Hadron event with a lifetime around 20 ns. The diagram includes one charged R-Hadron (solid blue) and one neutral R-Hadron (dashed blue). The pixel detector, calorimeters, and muon system are illustrated but not to scale.	62
254			
255			
256			
257			
258	Figure 34	The distribution of (a) E_T^{miss} and (b) Calorimeter E_T^{miss} for simulated signal events before the trigger requirement.	66
259			
260			
261	Figure 35	The distribution of E_T^{miss} for data and simulated signal events, after the trigger requirement.	68
262			
263	Figure 36	The trigger efficiency for the HLT_xe70 trigger requirement as a function of (a) E_T^{miss} and (b) Calorimeter E_T^{miss} for simulated signal events.	69
264			
265			
266	Figure 37	The dependence of dE/dx on N_{split} in data after basic track hit requirements have been applied.	70
267			
268	Figure 38	The distribution of dE/dx with various selections applied in data and simulated signal events.	70
269			

270	Figure 39	The distribution of track momentum for data and simulated signal events, after previous selection requirements have been applied.	71
271			
272			
273	Figure 40	The distribution of M_T for data and simulated signal events, after previous selection requirements have been applied.	72
274			
275			
276	Figure 41	The distribution of summed tracked momentum within a cone of $\Delta R < 0.25$ around the candidate track for data and simulated signal events, after previous selection requirements have been applied.	73
277			
278			
279			
280	Figure 42	The normalized, two-dimensional distribution of E/p and f_{EM} for simulated (a) $Z \rightarrow ee$, (b) $Z \rightarrow \tau\tau$, (c) 1200 GeV Stable R-Hadron events, and (d) 1200 GeV, 10 ns R-Hadron events.	74
281			
282			
283			
284	Figure 43	Two-dimensional distribution of dE/dx versus charge signed momentum (qp) for minimum-bias tracks. The fitted distributions of the most probable values for pions, kaons and protons are superimposed.	75
285			
286			
287			
288	Figure 44	The distribution of mass estimated using dE/dx for simulated stable R-Hadrons with masses between 1000 and 1600 GeV.	76
289			
290			
291	Figure 45	The acceptance \times efficiency as a function of R-Hadron (a) mass and (b) lifetime. (a) shows all of the combinations of mass and lifetime considered in this search, and (b) highlights the lifetime dependence for 1000 GeV and 1600 GeV R-Hadrons.	78
292			
293			
294			
295			
296	Figure 46	The distribution of (a) dE/dx and (b) momentum for tracks in data and simulated signal after requiring the event level selection and the track selection on p_T , hits, and N_{split} . Each sub-figure shows the normalized distributions for tracks classified as hadrons, electrons, and muons in data and R-Hadrons in the simulated signal.	80
297			
298			
299			
300			
301			
302			
303	Figure 47	The distribution of $M_{dE/dx}$ (a) before and (b) after the ionization requirement for tracks in simulated W boson decays and for the randomly generated background estimate.	82
304			
305			
306			
307	Figure 48	The distribution of $M_{dE/dx}$ (a) before and (b) after the ionization requirement for tracks in the validation region and for the randomly generated background estimate.	83
308			
309			
310			
311	Figure 49	The trigger efficiency for the HLT_xe70 trigger requirement as a function of Calorimeter E_T^{miss} for simulated data events with a W boson selection. Simulated signal events and simulated W boson events are also included.	88
312			
313			
314			
315			

316	Figure 50	The efficiency of the muon veto for R -hadrons of two different masses, as a function of $\frac{1}{\beta}$ for simulated R-Hadron tracks.	90
317			
318			
319	Figure 51	The average reconstructed MDT β distribution for $Z \rightarrow \mu\mu$ events in which one of the muons is reconstructed as a slow muon, for both data and simulation. A gaussian fit is superimposed.	91
320			
321			
322			
323	Figure 52	The observed mass distribution of events in data and the generated background distribution in (a) the stable and (b) the metastable signal region. A few example simulated signal distributions are superimposed.	92
324			
325			
326			
327	Figure 53	The observed and expected cross section limits as a function of mass for the stable simulated signal. The predicted cross section values for the corresponding signals are included.	95
328			
329			
330			
331	Figure 54	The observed and expected cross section limits as a function of mass for each generated lifetime. The predicted cross section values for the corresponding signals are included.	96
332			
333			
334			
335	Figure 55	The excluded range of masses as a function of gluino lifetime. The expected lower limit (LL), with its experimental $\pm 1\sigma$ band, is given with respect to the nominal theoretical cross-section. The observed 95% LL obtained at $\sqrt{s} = 8$ TeV [61] is also shown for comparison.	98
336			
337			
338			
339			
340	Figure 56	The constraints on the gluino mass as a function of lifetime for a split-supersymmetry model with the gluino R-Hadrons decaying into a gluon or light quarks and a neutralino with mass of 100 GeV. The solid lines indicate the observed limits, while the dashed lines indicate the expected limits. The area below the curves is excluded. The dots represent results for which the particle is assumed to be prompt or stable.	99
341			
342			
343			
344			
345			
346			
347			

349	Table 1	The design parameters of the LHC beam that determines the energy of collisions and the luminosity, for both the injection of protons and at the nominal circulation.	22
350			
351			
352			
353	Table 2	The dominant sources of corrections and systematic uncertainties in the JES estimation technique, including typical values for the correcting shift (Δ) and the associated uncertainty (σ).	51
354			
355			
356			
357	Table 3	The expected number of events at each level of the selection for metastable 1600 GeV, 10 ns R-Hadrons, along with the number of events observed in data, for 3.2 fb^{-1} . The simulated yields are shown with statistical uncertainties only. The total efficiency \times acceptance is also shown for the signal.	77
358			
359			
360			
361			
362			
363	Table 4	A summary of the sources of systematic uncertainty for the data-driven background in the signal region. If the uncertainty depends on the mass, the maximum values are reported.	85
364			
365			
366			
367	Table 5	A summary of the sources of systematic uncertainty for the simulated signal yield. The uncertainty depends on the mass and lifetime, and the maximum negative and positive values are reported in the table.	87
368			
369			
370			
371	Table 6	Example of the contributing systematic variations to the total systematic for the E_T^{miss} Scale, as measured in a 1200 GeV, Stable R-Hadron signal sample.	89
372			
373			
374	Table 7	The estimated number of background events and the number of observed events in data for the specified selection regions prior to the requirement on mass. The background estimates show statistical and systematic uncertainties.	92
375			
376			
377			
378			
379	Table 8	The left and right extremum of the mass window for each generated mass point with a 10 ns lifetime.	93
380			
381	Table 9	The left and right extremum of the mass window used for each generated stable mass point.	93
382			
383	Table 10	The expected number of signal events, the expected number of background events, and the observed number of events in data with their respective statistical errors within the respective mass window for each generated stable mass point	94
384			
385			
386			
387			

388	Table 11	The expected number of signal events, the expected number of background events, and the observed number of events in data with their respective statistical errors within the respective mass window for each generated mass point with a lifetime of 10 ns.	94
389			
390			
391			
392			
393	Table 12	The observed and expected 95% CL lower limit on mass for gluino R-Hadrons for each considered lifetime.	97
394			
395	Table 13	The left and right extremum of the mass window for each generated mass point with a 50 ns lifetime.	109
396			
397	Table 14	The left and right extremum of the mass window for each generated mass point with a 30 ns lifetime.	109
398			
399	Table 15	The left and right extremum of the mass window for each generated mass point with a 10 ns lifetime.	110
400			
401	Table 16	The left and right extremum of the mass window used for each generated mass point with a lifetime of 3 ns.	110
402			
403	Table 17	The left and right extremum of the mass window used for each mass point with a lifetime of 1 ns.	110
404			
405	Table 18	The left and right extremum of the mass window for each generated mass point with a lifetime of 0.4 ns.	111
406			
407	Table 19	The left and right extremum of the mass window used for each generated stable mass point.	111
408			
409	Table 20	The expected number of signal events, the expected number of background events, and the observed number of events in data with their respective statistical errors within the respective mass window for each generated mass point with a lifetime of 50 ns.	111
410			
411			
412			
413			
414	Table 21	The expected number of signal events, the expected number of background events, and the observed number of events in data with their respective statistical errors within the respective mass window for each generated mass point with a lifetime of 30 ns.	112
415			
416			
417			
418			
419	Table 22	The expected number of signal events, the expected number of background events, and the observed number of events in data with their respective statistical errors within the respective mass window for each generated mass point with a lifetime of 10 ns.	112
420			
421			
422			
423			
424	Table 23	The expected number of signal events, the expected number of background events, and the observed number of events in data with their respective statistical errors within the respective mass window for each generated mass point with a lifetime of 3 ns.	113
425			
426			
427			
428			
429	Table 24	The expected number of signal events, the expected number of background events, and the observed number of events in data with their respective statistical errors within the respective mass window for each generated mass point with a lifetime of 1 ns.	113
430			
431			
432			
433			

434	Table 25	The expected number of signal events, the expected number of background events, and the observed num- ber of events in data with their respective statistical er- rors within the respective mass window for each gen- erated mass point with a lifetime of p4 ns.	114
435			
436			
437			
438			
439	Table 26	The expected number of signal events, the expected number of background events, and the observed num- ber of events in data with their respective statistical er- rors within the respective mass window for each gen- erated stable mass point	114
440			
441			
442			
443			

444 LISTINGS

⁴⁴⁵ ACRONYMS

- ⁴⁴⁶ SM Standard Model
⁴⁴⁷ SUSY Supersymmetry
⁴⁴⁸ LSP Lightest Supersymmetric Particle
⁴⁴⁹ LHC Large Hadron Collider
⁴⁵⁰ ATLAS A Toroidal LHC ApparatuS
⁴⁵¹ CMS Compact Muon Solenoid
⁴⁵² ALICE A Large Ion Collider Experiment
⁴⁵³ LHCb Large Hadron Collider beauty experiment
⁴⁵⁴ LEP the Large Electron Positron collider
⁴⁵⁵ PS Proton Synchrotron
⁴⁵⁶ PSB Proton Synchrotron Booster
⁴⁵⁷ SPS Super Proton Synchrotron
⁴⁵⁸ ToT time over threshold
⁴⁵⁹ LCW local cluster weighted
⁴⁶⁰ MIP minimally ionizing particle
⁴⁶¹ EPJC European Physical Journal C
⁴⁶² JES jet energy scale
⁴⁶³ LLP Long-Lived Particle
⁴⁶⁴ CR Control Region
⁴⁶⁵ NLO next-to-leading order
⁴⁶⁶ NLL next-to-leading logarithmic
⁴⁶⁷ PDF parton distribution function
⁴⁶⁸ ISR initial state radiation
⁴⁶⁹ RMS root mean square
⁴⁷⁰ IBL Insertible B-Layer
⁴⁷¹ CP Combined Performance
⁴⁷² MDT Monitored Drift Tube
⁴⁷³ RF radiofrequency

474

PART I

475

INTRODUCTION

476

You can put some informational part preamble text here.

1

477

478 INTRODUCTION

479

PART II

480

THEORETICAL CONTEXT

481

You can put some informational part preamble text here.

2

482

483 STANDARD MODEL

484 The SM of particle physics seeks to explain the symmetries and interactions of
485 all currently discovered fundamental particles. It has been tested by several genera-
486 tions of experiments and has been remarkably successful, no significant de-
487 viations have been found. The SM provides predictions in particle physics for
488 interactions up to the Planck scale (10^{15} - 10^{19} GeV).

489 The theory itself is a quantum field theory grown from an underlying $SU(3) \times$
490 $SU(2) \times U(1)$ that requires the particle content and quantum numbers consist-
491 ent with experimental observations (see Section 2.1). Each postulated symme-
492 try is accompanied by an interaction between particles through gauge invari-
493 ance. These interactions are referred to as the Strong, Weak, and Electromag-
494 netic forces, which are discussed in Section 2.2.

495 Although this model has been very predictive, the theory is incomplete; for
496 example, it is not able to describe gravity or astronomically observed dark matter.
497 These limitations are discussed in more detail in Section 2.3.

498 21 PARTICLES

499 The most familiar matter in the universe is made up of protons, neutrons, and
500 electrons. Protons and neutrons are composite particles, however, and are made
501 up in turn by particles called quarks. Quarks carry both electric charge and color
502 charge, and are bound in color-neutral combinations called baryons. The elec-
503 tron is an example of a lepton, and carries only electric charge. Another type
504 of particle, the neutrino, does not form atomic structures in the same way that
505 quarks and leptons do because it carries no color or electric charge. Collectively,
506 these types of particles are known as fermions, the group of particles with half-
507 integer spin.

508 There are three generations of fermions, although familiar matter is formed
509 predominantly by the first generation. The generations are identical except for
510 their masses, which increase in each generation by convention. In addition, each
511 of these particles is accompanied by an antiparticle, with opposite-sign quantum
512 numbers but the same mass.

513 The fermions comprise what is typically considered matter, but there are
514 additional particles that are mediators of interactions between those fermions.
515 These mediators are known as the gauge bosons, gauge in that their existence
516 is required by gauge invariance (discussed further in Section 2.2) and bosons in
517 that they have integer spin. The boson which mediates the electromagnetic force
518 is the photon, the first boson to be discovered; it has no electric charge, no mass,
519 and a spin of 1. There are three spin-1 mediators of the weak force, the two
520 W bosons and the Z boson. The W bosons have electric charge of ± 1 and a
521 mass of 80.385 ± 0.015 GeV, while the Z boson is neutral and has a mass of

522 91.1876 \pm 0.0021 GeV. The strong force is mediated by eight particles called
 523 gluons, which are massless and electrically neutral but do carry color charge.

524 The final particle present in the SM is the Higgs boson, which was recently
 525 observed for the first time by experiments at CERN in 2012. It is electrically
 526 neutral, has a mass of 125.7 \pm 0.4 GeV, and is the only spin-0 particle yet to be
 527 observed. The Higgs boson is the gauge boson associated with the mechanism
 528 that gives a mass to the W and Z bosons.

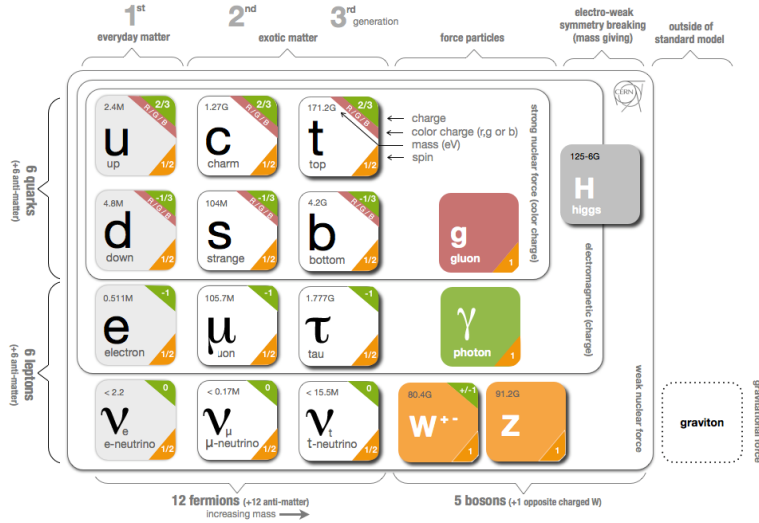


Figure 1: The particle content of the SM.

529 Together these particles form the entire content of the SM, and are summa-
 530 rized in Figure 1. These are the particles that constitute the observable universe
 531 and all the so-far-observed interactions within it.

532 2.2 INTERACTIONS

533 The interactions predicted and described by the SM are fundamentally tied to the
 534 particles within it, both in that they describe the way those particles can influence
 535 each other and also in that the existence of the interactions requires the existence
 536 of some particles (the gauge bosons).

537 2.3 LIMITATIONS

3

538

539 SUPERSYMMETRY

540 3.1 MOTIVATION

541 3.2 STRUCTURE

542 3.3 PHENOMENOLOGY

4

543

544 LONG-LIVED PARTICLES

545 4.1 MECHANISMS

546 4.1.1 EXAMPLES IN SUPERSYMMETRY

547 4.2 PHENOMENOLOGY

548 4.2.1 DISIMILARITIES TO PROMPT DECAYS

549 4.2.2 CHARACTERISTIC SIGNATURES

550

PART III

551

EXPERIMENTAL STRUCTURE AND RECONSTRUCTION

552

You can put some informational part preamble text here.

553

554 THE LARGE HADRON COLLIDER

555 The LHC, a two-ring superconducting hadron accelerator, provides high energy
556 proton-proton collisions for several large experiments at CERN! (CERN!) in Geneva,
557 Switzerland [1, 2]. It is the largest, highest-luminosity, and highest-energy pro-
558 ton collider ever built, and was constructed by a collaboration of more than
559 10,000 scientists from more than 100 countries that contribute to CERN!. The
560 original design of the LHC focused on providing collision energies of up to 14
561 TeV and generating enough collisions to reveal physics beyond the SM predicted
562 to exist at higher energy scales.

563 The LHC was installed in an existing 27 km tunnel at CERN! which was origi-
564 nally designed to house the Large Electron Positron collider (LEP). This allows
565 the collider to use existing accelerators at the same complex to provide the ini-
566 tial acceleration of protons up to 450 GeV before injecting into LHC to accel-
567 erate up to design energies. The injected hadrons can be accelerated up to as
568 much as 14 TeV while being focused into two beams travelling in opposite di-
569 rections. During this process the protons can circulate around the tunnel mil-
570 lions of times, while the beams are intermittently crossed at the four locations
571 of the experiments to provide collisions. These collision points correspond to
572 the four major LHC experiments: A Toroidal LHC ApparatuS (ATLAS), Compact
573 Muon Solenoid (CMS), Large Hadron Collider beauty experiment (LHCb), and
574 A Large Ion Collider Experiment (ALICE), and Figure 2 shows the layout of the
575 experiments both on the surface and below. ATLAS and CMS are both general pur-
576 pose, high-luminosity detectors which search for a wide range of new types of
577 physics [3, 4]. LHCb studies the interactions of b-hadrons to explore the asymme-
578 try between matter and antimatter [5]. ALICE focuses on the collisions of lead
579 ions, which the LHC also provides, in order to study the properties of quark-
580 gluon plasma [6].

581 During the first five years of operation, after the LHC turned on in 2010, the
582 LHC has provided four major data collecting periods. In 2010 the LHC increased
583 the energy from 900 GeV to 2.76 TeV and then subsequently to 7 TeV, with
584 a peak luminosity of $2 \times 10^{32} \text{ cm}^{-2}\text{s}^{-1}$, with a total delivered luminosity of 50
585 pb^{-1} for the ATLAS detector. The next run, during 2011, continued the operation
586 at 7 TeV and provided an additional 5 fb^{-1} with a peak luminosity of 4×10^{33}
587 $\text{cm}^{-2}\text{s}^{-1}$. The energy was then increased to 8 TeV for the data collection during
588 2012, which provided 23 fb^{-1} with a peak luminosity of $7.7 \times 10^{33} \text{ cm}^{-2}\text{s}^{-1}$. Af-
589 ter the first long shutdown for 2013 and 2014, the LHC resumed operation and
590 increased the energy to 13 TeV in 2015, where it delivered 4.2 fb^{-1} with a peak
591 luminosity of $5.5 \times 10^{33} \text{ cm}^{-2}\text{s}^{-1}$.

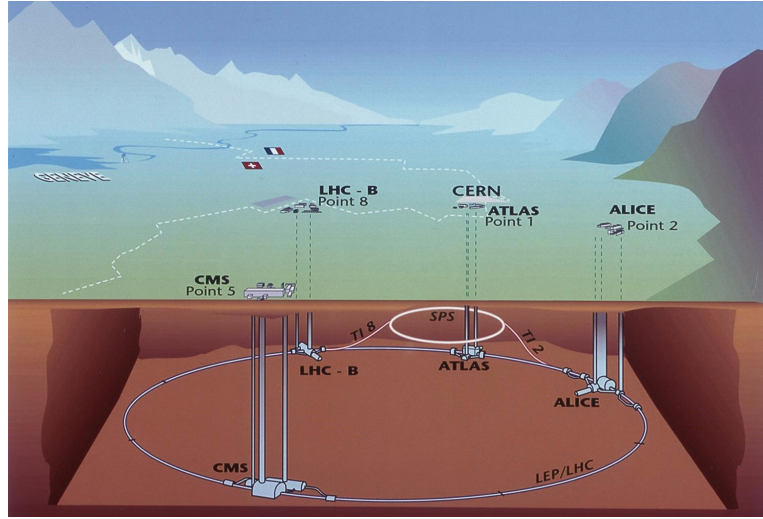


Figure 2: The four collision points and corresponding experiments of the LHC. The image includes the location of the nearby city of Geneva as well as the border of France and Switzerland.

592 5.1 INJECTION CHAIN

593 The LHC takes advantage of the presence of previously built accelerators at CERN!
 594 to work up to the target energy in consecutive stages. The series of accelerators
 595 that feed into the LHC are known collectively as the injection chain, and together
 596 with the LHC form the accelerator complex. The full complex is illustrated in
 597 Figure 3, which details the complex series required to reach collisions of 13 or
 598 14 TeV.

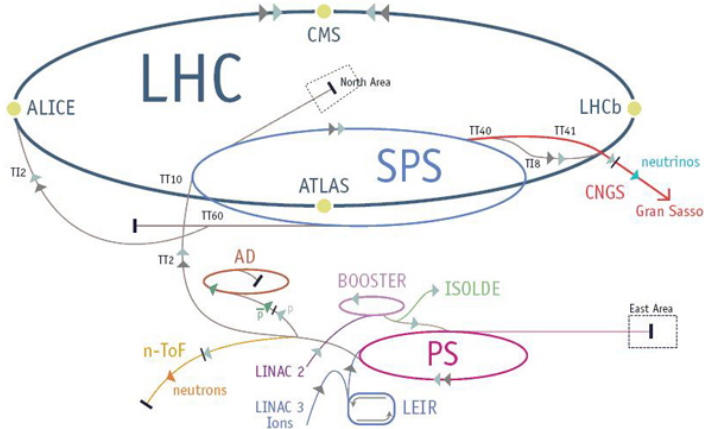


Figure 3: The accelerator complex that builds up to the full design energies at the LHC. The protons are passed in order to Linac 2, the PSB, the PS, the SPS and then the LHC.

599 Protons at the LHC begin as hydrogen atoms in the Linac 2, a linear accelerator
 600 which replaced Linac 1 as the primary proton accelerator at CERN in 1978. In
 601 Linac 2, the hydrogen atoms are stripped of their electrons by a strong magnetic

field, and the resulting protons are accelerated up to 50 MeV by cylindrical conductors charged by radiofrequency cavities. The protons are then transferred to the Proton Synchrotron Booster (**PSB**), which uses a stack of four synchrotron rings to accelerate the protons up to 1.4 GeV. Then the protons are injected into the Proton Synchrotron (**PS**) which again uses synchrotron rings to bring the energy up to 25 GeV. The intermediate step between Linac 2 and the **PS** is not directly necessary, as the **PS** can accelerate protons starting from as low as 50 MeV. The inclusion of the **PSB** allows the **PS** to accept a higher intensity of injection and so increases the deliverable luminosity in the **LHC**. The penultimate stage of acceleration is provided by the Super Proton Synchrotron (**SPS**), a large synchrotron with a 7 km circumference that was commissioned at CERN in 1976. During this step the protons increase in energy to 450 GeV, after which they can be directly injected into the **LHC**.

The final step is the **LHC** itself, which receives protons from the **SPS** into two separate beam pipes which circulate in opposite directions. The filling process at this step takes approximately 4 minutes, and the subsequent acceleration to the final energy (6.5 TeV during 2015 and up to 7 TeV by design) takes approximately half an hour. At this point the protons circulate around the circumference tens of thousands of times a second and continue for up to two hours.

5.2 DESIGN

5.2.1 LAYOUT

Many of the aspects of the **LHC** design are driven by the use of the existing **LEP** tunnel. This tunnel slopes gradually, with a 1.4% decline, with 90% of its length built into molasse rock which is particularly well suited to the application. The circumference is composed of eight 2987 meter arcs and eight 528 meter straight sections which connect them; this configuration is illustrated in Figure 4. The tunnel diameter is 3.7 m throughout its length.

The design energy is directly limited by the size of this tunnel, with its radius of curvature of 2804 m. A significant magnetic field is required to curve the protons around that radius of curvature; the relationship is given by

$$p \approx 0.3BR$$

where p is the momentum of the particle in GeV, B is the magnetic field in Tesla, and R is the radius of curvature in meters. From the target design energy of 14 TeV, or 7 TeV of momentum for protons in each beam, the required magnetic field is 8.33 Tesla. This is too large a field strength to be practical with iron electromagnets, because of the enormous power required and the resulting requirements for cooling. Because of these constraints, the **LHC** uses superconducting magnets which can maintain that field strength with significantly less power consumption.

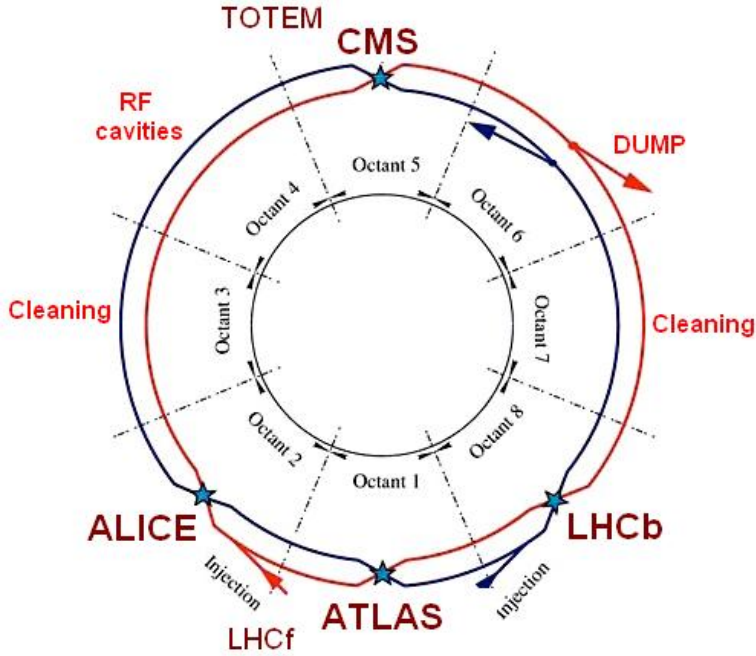


Figure 4: A schematic of the layout of the [LHC](#), not to scale. The arched and straight sections are illustrated at the bottom of the schematic, and all four crossing sites are indicated with their respective experiments.

637 5.2.2 MAGNETS

638 Specifically the magnets chosen were Niobium and Titanium (NbTi) which allow
 639 for field strengths as high as 10 Tesla when cooled down to 1.9 K. Reach 1.9 K
 640 for all of the magnetis requires superfluid helium and a large cryogenic system
 641 along the entire length of the tunnel. During normal operation, the [LHC](#) uses 120
 642 tonnes of helium within the magnetics, and the entire system is cooled by eight
 643 cryogenic helium refrigerators. The temperature increase that occurs during
 644 transit from the refrigerator along the beam necessitates that the refrigerators
 645 cool the helium down to 1.8 K. Any significant increase above this temperature
 646 range can remove the superconductive properties of the magnets, which in turn
 647 generates drastically larger heat losses from the current within the magnets and
 648 causes a rapid rise in temperature called a quench.

649 In all there are approximately 8000 superconducting magnets distributed around
 650 the [LHC](#). The 1232 bending magnets, which keep the protons curving along the
 651 length of the beam, are twin bore cryodipoles, which allow both proton beams to
 652 be accomodated by one magnet and all of the associated cooling structure. Fig-
 653 ure 5 shows the cross section of the design for these dipoles. The magnets are
 654 very large, 16.5 m long with a diameter of 0.57 meters and a total weight of 28
 655 tonnes. They are slightly curved, with an angle of 5.1 mrad, in order to carefully
 656 match the beam path. The twin bore accomodates both magnets inside the two
 657 5 cm diameter holes which are surrounded by the superconducting coils. The
 658 coils require 12 kA of current in order to produce the required magnetic field.
 659 These coils are comprised of NbTi cable wound in two layers; the wire in the

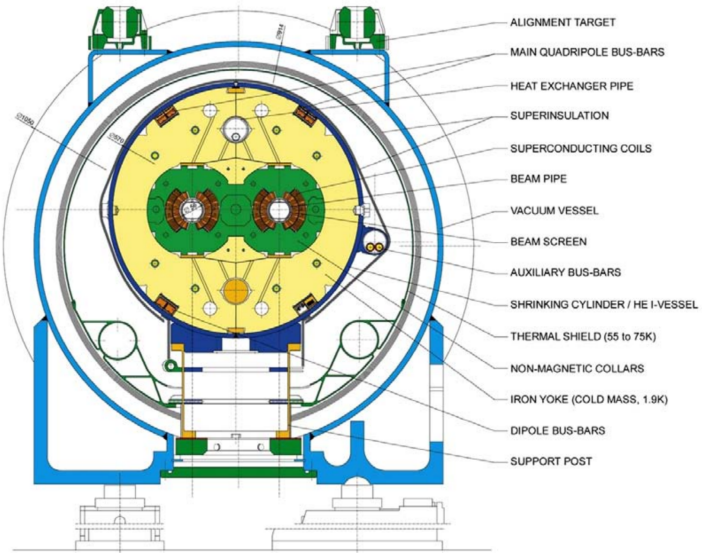


Figure 5: A cross section of the the cryodipole magnets which bend the flight path of protons around the circumference of the LHC. The diagram includes both the superconducting coils which produce the magnetic field and the structural elements which keep the magnets precisely aligned.

660 inner layer has a diameter of 1.065 mm while the wire in the outer layer has a
661 diameter of 0.825 mm.

662 The large current in the wires, along with the magnetic field produced, result
663 in forces on the magnets which would tend to push them apart with over 10,000
664 Newtons per meter. Constraining the magnets requires a significant amount of
665 structure including non-magnetic stainless steel collars. Both the presence of
666 these electromagnetic forces and the varying thermal contraction coefficient of
667 the pieces of the magnet produce significant forces on the cold mass structure.
668 The cold mass is carefully engineered so that these stresses do not significantly
669 alter the magnetic field shape, which must be maintained between magnets to a
670 precision of approximately 10^{-4} for successful operation.

671 The remaining 6800 magnets are a variety of quadrupole, sextapole, octopole,
672 and single bore dipole magnets. These are used to damp oscillations, correct
673 beam trajectories, focus the beams during circulation, and to squeeze the beams
674 before collisions.

675 5.2.3 RF CAVITIES

676 Sixteen RF cavities produce the actual acceleration of the proton beam up to the
677 design energy. These RF cavities are tuned to operate at 400 MHz, and are powered
678 by high-powered electron beams modulated at the same frequency, called
679 klystrons. The resonance within the cavity with the oscillating electric field
680 establishes a voltage differential of 2 MV per cavity. The sixteen cavities are
681 split between the two beams, so combined the cavities provide 16 MV per beam,
682 which accelerate the protons on each consecutive pass through the cavity. This

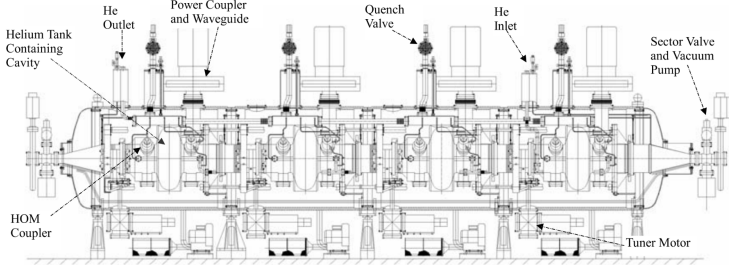


Figure 6: The arrangement of four RF cavities within a cryomodule.

683 acceleration is also necessary during circulation even after the target energy has
684 been reach in order to compensate for losses from synchrotron radiation.

685 The cavities are arranged in cryomodules which contain four cavities, with
686 two cryomodules per beam; this arrangement is illustrated in Figure 6. These
687 cryomodules are necessary to maintain the superconducting state of the cavities,
688 which are also constructed from niobium. The RF cavities use niobium along
689 with copper to allow for low power losses in the superconductors. The copper
690 provides a reduced susceptibility to quenching, as it rapidly conducts away heat
691 generated by imperfections in the niobium, as well as natural shielding from the
692 earth's magnetic field which can interfere with the RF system.

693 The nature of the radio frequency oscillations tends to group protons together
694 into buckets. A proton travelling exactly in phase with the RF oscillations will not
695 be displaced at all during a single circulation, and those slightly ahead or behind
696 of that phase will slightly decelerate or accelerate, respectively. This produces
697 separate clusters of protons which arrive in phase to the cavities every 2.5 ns,
698 corresponding to the 400 MHz frequency.

699 5.2.4 BEAM

700 The beams of protons circulate within 54 km of 5 cm diameter beam pipe. This
701 entire structure is kept under vacuum at 1.9 K to prevent interactions between
702 the beam pipe and the magnets as well as to prevent any interactions between the
703 circulating protons and gas in the pipe. The vacuum within the pipe establishes
704 a pressure as low as 10^{-9} mbar before the protons are introduced.

705 Because of the very high energies of the circulating protons, synchrotron radia-
706 tion is not negligible in the bending regions. The protons are expected to radiate
707 3.9 kW per beam at 14 TeV, with 0.22 W/m, which is enough power to heat the
708 liquid helium and cause a quench were it absorbed by the magnets. To prevent
709 this, a copper screen is placed within the vacuum tube that absorb the emitted
710 photons. This screen is kept between 5 and 20 K by the liquid helium cooling
711 system.

712 5.3 LUMINOSITY PARAMETERS

713 In addition to the high energy of the collisions, the rate of collisions is extremely
 714 important to enabling the discovery of new physics. Many measurements and
 715 searches require a large number of events in order to be able to make statistically
 716 significant conclusions. The rate of collisions is measured using luminosity, the
 717 number of collisions per unit time and unit cross section for the proton-proton
 718 collisions. From the beam parameters, luminosity is given by

$$\mathcal{L} = \frac{N_b^2 n_b f_{rev} \gamma}{4\pi \epsilon_n \beta^*} F$$

719 where N_b is the number of protons per bunch, n_b is the number of bunches per
 720 beam, f_{rev} is the frequency of revolution, γ is the Lorentz factor for the protons
 721 at the circulating energy, ϵ_n is the emittance, β^* is the amplitude function at the
 722 collision point, and F is a geometric factor that accounts for the crossing angle of
 723 the beams at the collision point. The emittance measures the average spread of
 724 particles in both position and momentum space, while the amplitude function
 725 is a beam parameter which measures how much the beam has been squeezed.
 726 Together ϵ_n and β^* give the size of the beam in the transverse direction, $\sigma =$
 727 $\sqrt{\epsilon \beta^*}$. β changes over the length of the beam as the accessory magnets shape the
 728 distribution of protons, but only the value at the point of collisions, β^* , affects
 729 the luminosity.

730 The luminosity is maximized to the extent possible by tuning the parameters
 731 in Equation ???. A number of these are constrained by the design decisions. The
 732 revolution frequency is determined entirely by the length of the tunnel, as the
 733 protons travel at very close to the speed of light. The geometric factor F is de-
 734 termined by the crossing angle of the beams at the collision points, again a com-
 735 ponent of the tunnel design; this angle is already very small at 285 μ rad, which
 736 helps to maximize the geometric factor.

737 The major pieces that can be adjusted are the number of protons per bunch,
 738 N_b , the number of bunches in the beam, n_b , and the amplitude function β . In-
 739 creasing either N_b or n_b increases the amount of energy stored in the beam, which
 740 presents a danger if control of the beam is lost. At design specifications, the beam
 741 stores 362 MJ, which is enough energy to damage the detectors or accelerator if
 742 the beam were to wander out of the beam pipe. So, the luminosity is primarily
 743 controlled at the [LHC](#) by adjusting β^* , where lowering β^* increases the luminos-
 744 ity. β^* is tuned to provide the various values of luminosity used at the [LHC](#) which
 745 can be raised to as much as 10^{34} in design.

746 The nominal bunch structure consists of 3654 bunches, each holding 10^{11} pro-
 747 tons, which cross a collision point in 25 ns. These are further subdivided into the
 748 buckets mentioned in Section 5.2.3 by the clustering properties of the [RF](#) cavities.
 749 The bunches are further grouped into trains of 72 bunches which are separated
 750 by a gap which would otherwise hold 12 bunches. At nominal operation 2808
 751 of the bunches will actually be filled with protons, while the remainder are left
 752 empty to form an abort gap that can be used in case the beam needs to be dumped.

Parameter	Unit	Injection	Nominal
Beam Energy	TeV	0.450	7
Peak Instantaneous Luminosity	$\text{cm}^{-2}\text{s}^{-1}$	-	10^{34}
Bunch Spacing	ns	25	25
Number of Filled Bunches	2808	2808	
Normalized Transverse Emittance	μm	3.75	3.75
Frequency	MHz	400.789	400.790
RF Voltage/Beam	8	16	
Stored Energy	MJ	-	362
Magnetic Field	T	0.54	8.33
Operating Temperature	K	1.9	1.9

Table 1: The design parameters of the [LHC](#) beam that determines the energy of collisions and the luminosity, for both the injection of protons and at the nominal circulation.

753 The various beam parameters are summarized in Table 1 for the designed operation.
 754 In practice the beam has operated at lower energies and lower luminosities
 755 than the design values, but the [LHC](#) is expected to operate at the full design
 756 values during Run 2.

757 5.4 DELIVERED LUMINOSITY

During the data collection of 2015, the [LHC](#) operated at luminosities as large as 5×10^{33} . It is convenient to refer to the integrated luminosity, the integral of the instantaneous luminosity, which corresponds directly to the number of delivered events for a given process.

$$N = \sigma \times \int \mathcal{L}(t) dt$$

758 where σ is the cross section for the process of interest. The integrated luminosity over time is shown in Figure 7. This includes the luminosity delivered
 759 by the [LHC](#) as well as the luminosity that was recorded by [ATLAS](#). Some of the
 760 delivered luminosity is not recorded because [ATLAS](#) is placed in standby until
 761 the [LHC](#) reports that the beam conditions are stable, and only then does [ATLAS](#)
 762 begin recording. The figure also includes the amount of luminosity marked as
 763 good for physics measurements, which includes additional requirements on the
 764 operation of the detector during data collection that are necessary for physics
 765 measurements.

766 In addition to the instantaneous luminosity, the beam conditions also influence
 767 the number of collisions that occur within a single bunch crossing. The
 768 multiple interactions at each crossing are referred to as pileup, often denoted μ ,
 769 and each of these interactions are present in a single measured event. Figure 8
 770 shows the luminosity-weighted distribution of the mean number of interactions

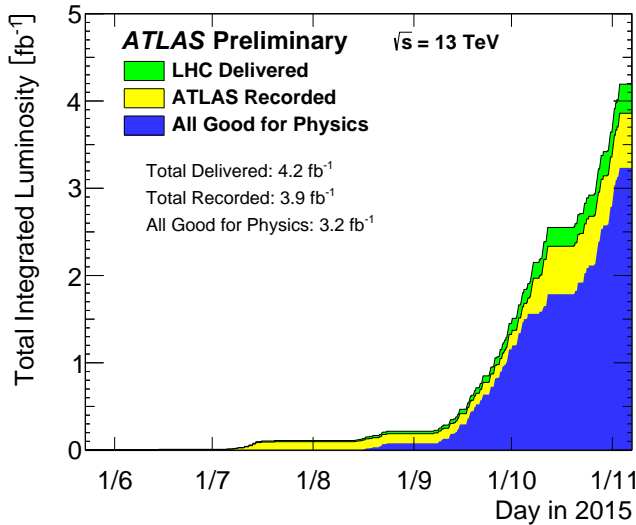


Figure 7: The cumulative luminosity versus time delivered to ATLAS (green), recorded by ATLAS (yellow), and certified to be good quality data (blue) during stable beams for pp collisions at 13 TeV in 2015.

772 for events collected in 2015. The presences of as many as 20 events in a signle
 773 collision provides a significant challenge in reconstructing events and isolating
 774 the targetted physical processes.

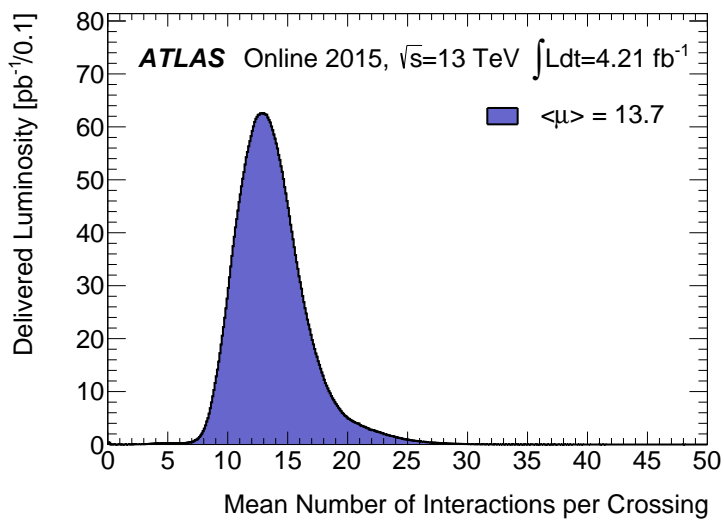


Figure 8: The luminosity-weighted distribution of the mean number of interactions per crossing for the 2015 pp collision data at 13 TeV.

6

775

776 THE ATLAS DETECTOR

777 6.1 COORDINATE SYSTEM

778 6.2 MAGNETIC FIELD

779 6.3 INNER DETECTOR

780 6.3.1 PIXEL DETECTOR

781 6.3.2 SEMICONDUCTOR TRACKER

782 6.3.3 TRANSITION RADIATION TRACKER

783 6.4 CALORIMETRY

784 6.4.1 ELECTROMAGNETIC CALORIMETERS

785 6.4.2 HADRONIC CALORIMETERS

786 6.4.3 FORWARD CALORIMETERS

787 6.5 MUON SPECTROMETER

788 6.6 TRIGGER

789 6.6.1 TRIGGER SCHEME

790 6.6.2 MISSING TRANSVERSE ENERGY TRIGGERS

7

791

792 EVENT RECONSTRUCTION

793 The ATLAS experiment combines measurements in the subdetectors to form a
794 cohesive picture of each physics event.

795 7.1 TRACKS AND VERTICES

796 7.1.1 TRACK RECONSTRUCTION

797 7.1.1.1 NEURAL NETWORK

798 7.1.1.2 PIXEL DE/DX

799 7.1.2 VERTEX RECONSTRUCTION

800 7.2 JETS

801 7.2.1 TOPOLOGICAL CLUSTERING

802 7.2.2 JET ENERGY SCALE

803 7.2.3 JET ENERGY SCALE UNCERTAINTIES

804 7.2.4 JET ENERGY RESOLUTION

805 7.3 ELECTRONS

806 7.3.1 ELECTRON IDENTIFICATION

807 7.4 MUONS

808 7.4.1 MUON IDENTIFICATION

809 7.5 MISSING TRANSVERSE ENERGY

810

PART IV

811

CALORIMETER RESPONSE

812

You can put some informational part preamble text here.

814 RESPONSE MEASUREMENT WITH SINGLE HADRONS

815 As discussed in Section 7.2, colored particles produced in collisions hadronize
816 into jets of multiple hadrons. One approach to understanding jet energy mea-
817 surements in the ATLAS calorimeters is to evaluate the calorimeter response to
818 those individual hadrons; measurements of individual hadrons can be used to
819 build up an understanding of the jets that they form. The redundancy of the
820 momentum provided by the tracking system and the energy provided by the
821 calorimeter provides an opportunity to study calorimeter response using real
822 collisions, as described further in Section 8.2.

823 Calorimeter response includes a number of physical effects that can be ex-
824 tracted to provide insight into many aspects of jet modeling. First, many charged
825 hadrons interact with the material of the detector prior to reaching the calorime-
826 ters and thus do not deposit any energy. Comparing this effect in data and simu-
827 lation is a powerful tool in validating the interactions of particles with the mate-
828 rial of the detector and the model of the detector geometry in simulation, see Sec-
829 tion 8.2.2. The particles which do reach the calorimeter deposit their energy into
830 several adjacent cells, which are then clustered together. The energy of the clus-
831 ter is then the total energy deposited by that particle. Comparing the response of
832 hadrons in data to that of simulated hadrons provides a direct evaluation of the
833 showering of hadronic particles and the energy deposited by particles in matter
(Section 8.2.4).

835 The above studies all use an inclusive selection of charged particles, which are
836 comprised predominantly of pions, kaons, and (anti)protons. It is also possible to
837 measure the response to various identified particle types separately to evaluate
838 the simulated interactions of each particle, particularly at low energies where
839 differences between species are very relevant. Pions and (anti)protons can be
840 identified through decays of long-lived particles, in particular Λ , $\bar{\Lambda}$, and K_S^0 , and
841 then used to measure response as described above. This is discussed in detail in
842 Section 8.3.

843 The results in this chapter use data collected at 7 and 8 TeV collected in 2010
844 and 2012, respectively. Both are included as the calorimeter was repaired and
845 recalibrated between those two data-taking periods. Both sets of data are com-
846 pared to an updated simulation that includes new physics models provided by
847 Geant4 [7] and improvements in the detector description [8, 9]. The present
848 results are published in European Physical Journal C (EPJC) [10] and can be com-
849 compared to a similar measurement performed in 2009 and 2010 [11], which used
850 the previous version of the simulation framework [12].

851 8.1 DATASET AND SIMULATION

852 8.1.1 DATA SAMPLES

853 The two datasets used in this chapter are taken from dedicated low-pileup runs
 854 where the fraction of events with multiple interactions was negligible. These
 855 datasets are used rather than those containing full-pileup events to facilitate mea-
 856 surement of isolated hadrons. The 2012 dataset at $\sqrt{s} = 8$ TeV contains 8 mil-
 857 lion events and corresponds to an integrated luminosity of 0.1 nb^{-1} . The 2010
 858 dataset at $\sqrt{s} = 7$ TeV contains 3 million events and corresponds to an inte-
 859 grated luminosity of 3.2 nb^{-1} . The latter dataset was also used for the 2010 re-
 860 sults [11], but it has since been reanalyzed with an updated reconstruction in-
 861 cluding the final, best understanding of the detector description for the material
 862 and alignment from Run 1.

863 8.1.2 SIMULATED SAMPLES

864 The two datasets above are compared to simulated single-, double-, and non-
 865 diffractive events generated with Pythia8 [13] using the A2 configuration of
 866 hadronization [14] and the MSTW 2008 parton-distribution function set [15,
 867 16]. The admixture of the single-, double-, and non-diffractive events uses the
 868 default relative contributions from Pythia8. The conditions and energies for
 869 the two simulations are chosen so that they match those of the corresponding
 870 dataset.

871 To evaluate the interaction of hadrons with detector material, the simulation
 872 uses two different collections of hadronic physics models, called physics lists, in
 873 Geant4 9.4 [17]. The first, QGSP_BERT, combines the Bertini intra-nuclear
 874 cascade [18–20] below 9.9 GeV, a parametrized proton inelastic model from 9.5
 875 to 25 GeV [21], and a quark-gluon string model above 12 GeV [22–26]. The
 876 second, FTFP_BERT, combines the Bertini intra-nuclear cascade [18–20] below
 877 5 GeV and the Fritiof model [27–30] above 4 GeV. In either list, Geant4 en-
 878 forces a smooth transition between models where multiple models overlap.

879 8.1.3 EVENT SELECTION

880 The event selection for this study is minimal, as the only requirement is selecting
 881 good-quality events with an isolated track. Such events are triggered by requir-
 882 ing at least two hits in the minimum-bias trigger scintillators. After trigger, each
 883 event is required to have exactly one reconstructed vertex, and that vertex is re-
 884 quired to have four or more associated tracks.

885 The particles which are selected for the response measurements are first iden-
 886 tified as tracks in the inner detector. The tracks are required to have at least 500
 887 MeV of transverse momentum. To ensure a reliable momentum measurement,
 888 these tracks are required to have at least one hit in the pixel detector, six hits in
 889 the SCT, and small longitudinal and transverse impact parameters with respect
 890 to the primary vertex [11]. For the majority of the measurements in this chapter,

891 the track is additionally required to have 20 hits in the TRT, which significantly
 892 reduces the contribution from tracks which undergo nuclear interactions. This
 893 requirement and its effect is discussed in more detail in Section 8.2.5. In addition,
 894 tracks are rejected if there is any other reconstructed track which extrapolates
 895 to the calorimeter within a cone of $\Delta R = \sqrt{(\Delta\phi)^2 + (\Delta\eta)^2} < 0.4$. This require-
 896 ment guarantees that the contamination of energy from nearby charged particles
 897 is negligible [11].

898 8.2 INCLUSIVE HADRON RESPONSE

899 The calorimeter response is more precisely defined as the ratio of the measured
 900 calorimeter energy to the true energy carried by the particle, although this true
 901 energy is unknown. For charged particles, however, the inner detector provides
 902 a very precise measurement of momentum (with uncertainty less than 1%) that
 903 can be used as a proxy for true energy. The ratio of the energy deposited by
 904 the charged particle in the calorimeter, E , to its momentum measured in the
 905 inner detector p , forms the calorimeter response measure called E/p . Though
 906 the distribution of E/p contains a number of physical features, this study focuses
 907 on the trends in two aggregated quantities: $\langle E/p \rangle$, the average of E/p for the
 908 selected tracks, and the zero fraction, the fraction of tracks with no associated
 909 energy in the calorimeter for those tracks.

910 The calorimeter energy assigned to a track is defined using clusters. The clus-
 911 ters are formed using a 4–2–0 algorithm [31] that begins with seeds requiring
 912 at least 4 times the average calorimeter cell noise. The neighboring cells with
 913 at least twice that noise threshold are then added to the cluster, and all bound-
 914 ing cells are then added with no requirement. This algorithm minimizes noise
 915 contributions through its seeding process, and including the bounding cells im-
 916 proves the energy resolution [32]. The clusters are associated to a given track
 917 if they fall within a cone of $\Delta R = 0.2$ of the extrapolated position of the track,
 918 which includes about 90% of the energy on average [11]. This construction is
 919 illustrated in Figure 9.

920 8.2.1 E/P DISTRIBUTION

921 The E/p distributions measured in both data and simulation are shown in Fig-
 922 ure 10 for two example bins of track momentum and for tracks in the central
 923 region of the detector. These distributions show several important features of
 924 the E/p observable. The large content in the bin at $E = 0$ comes from tracks that
 925 have no associated cluster, which occurs due to interactions with detector mate-
 926 rial prior to reaching the calorimeter or the energy deposit being insufficiently
 927 large to generate a seed, and are discussed in Section 8.2.2. The small negative
 928 tail also comes from tracks that do not deposit any energy in the calorimeter but
 929 are randomly associated to a cluster with an energy below the noise threshold.
 930 The long positive tail above 1.0 comes from the contribution of neutral parti-
 931 cles. Nearby neutral particles deposit (sometimes large) additional energy in the
 932 calorimeter but do not produce tracks in the inner detector, so they cannot be

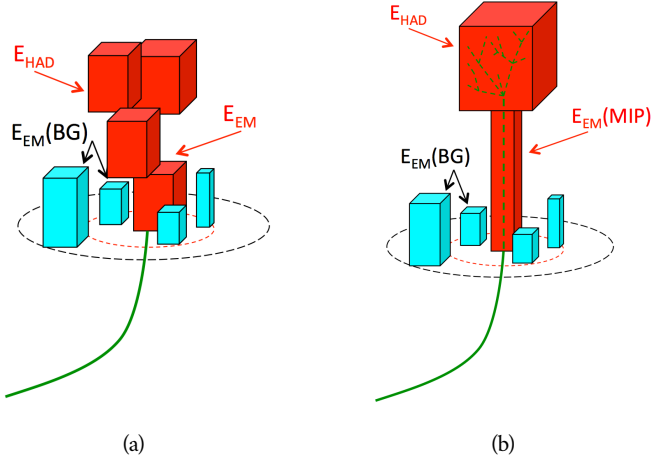


Figure 9: An illustration (a) of the E/p variable used throughout this paper. The red energy deposits come from the charged particle targeted for measurement, while the blue energy deposits are from nearby neutral particles and must be subtracted. The same diagram (b) for the neutral-background selection, described in Section 8.2.3.

933 rejected by the track isolation requirement. Additionally the peak and mean of
 934 the distribution falls below 1.0 because of the loss of energy not found within
 935 the cone as well as the non-compensation of the calorimeter.

936 The data and simulation share the same features, but the high and low tails
 937 are significantly different. The simulated events tend to overestimate the con-
 938 tribution of neutral particles to the long tail, an effect which can be isolated and
 939 removed as discussed in Section 8.2.3. Additionally, the simulated clusters have
 940 less noise on average, although this is a small effect on the overall response.

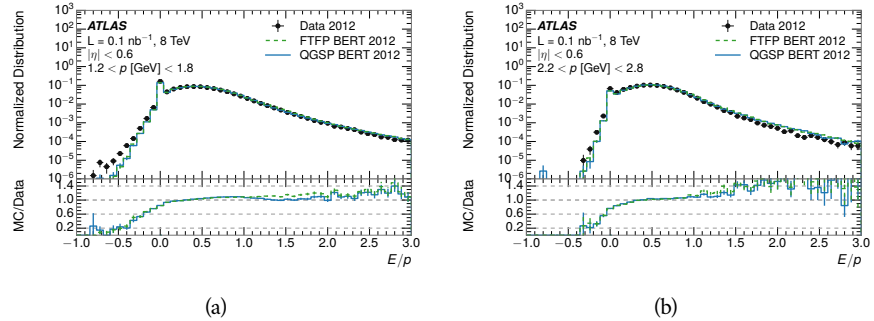


Figure 10: The E/p distribution and ratio of simulation to data for isolated tracks with
 (a) $|\eta| < 0.6$ and $1.2 < p/\text{GeV} < 1.8$ and (b) $|\eta| < 0.6$ and $2.2 < p/\text{GeV} < 2.8$.

941 8.2.2 ZERO FRACTION

942 The fraction of particles with no associated clusters, or similarly those with $E \leq$
 943 0, reflects the modeling of both the detector geometry and hadronic interactions.

944 The zero fraction is expected to rise as the amount of material a particle traverses
 945 increases, while it is expected to decrease as the particle energy increases. This
 946 dependence can be seen in Figure 11, where the zero fraction in data and simulation
 947 is shown as a function of momentum and the amount of material measured
 948 in interaction lengths. The trends are similar between 2010 and 2012 and for
 949 positively and negatively charged particles. The zero fraction decreases with
 950 energy as expected. The absolute discrepancy in zero fraction decreases with
 951 momentum from 5% to less than 1%, but this becomes more pronounced in the
 952 ratio as the zero fraction shrinks quickly with increasing momentum. There is
 953 a small constant difference between the data and simulation in both interaction
 954 models that becomes more pronounced. The amount of material in the detector
 955 increases with η , which is used to obtain results for interaction lengths ranging
 956 between 0.1 and 0.65 λ . As the data and simulation have significant disagree-
 957 ment in the zero fraction over a number of interaction lengths, the difference
 958 must be primarily from the modeling of hadronic interactions with detector ma-
 959 terial and not just the detector geometry. Although two different hadronic in-
 960 teraction models are shown in the figure, they have very similar discrepancies to
 961 data because both use the same description (the BERT model) at low momentum.

962 8.2.3 NEUTRAL BACKGROUND SUBTRACTION

963 The isolation requirement on hadrons is only effective in removing an energy
 964 contribution from nearby charged particles. Nearby neutral particles, predomi-
 965 nantly photons from π^0 decays, also add their energy to the calorimeter clusters,
 966 but mostly in the electromagnetic calorimeter. It is possible to measure this con-
 967 tribution, on average, using late-showering hadrons that minimally ionize in the
 968 electromagnetic calorimeter. Such particles are selected by requiring that they
 969 deposit less than 1.1 GeV in the EM calorimeter within a cone of $\Delta R < 0.1$
 970 around the track. To ensure that these particles are well measured, they are addi-
 971 tionally required to deposit between 40% and 90% of their energy in the hadronic
 972 calorimeter within the same cone.

973 These particles provide a clean sample to measure the nearby neutral back-
 974 ground because they do not deposit energy in the area immediately surrounding
 975 them in the EM calorimeter, as shown in Figure 9. So, the energy deposits in the
 976 region $0.1 < \Delta R < 0.2$ can be attributed to neutral particles alone. To estimate
 977 the contribution to the whole cone considered for the response measurement,
 978 that energy is scaled by a geometric factor of 4/3. This quantity, $\langle E/p \rangle_{BG}$, mea-
 979 sured in aggregate over a number of particles, gives the contribution to $\langle E/p \rangle$
 980 from neutral particles in the EM calorimeter. Similar techniques were used in
 981 the individual layers of the hadronic calorimeters to show that the background
 982 from neutrals is negligible in those layers [11].

983 The distribution of this background estimate is shown in Figure 12 for data
 984 and simulation with the two different physics lists. The contribution from neu-
 985 tral particles falls from 0.1 at low momentum to around 0.03 for particles above
 986 7 GeV. Although the simulation captures the overall trend, it significantly over-
 987 estimates the neutral contribution for tracks with momentum between 2 and 8

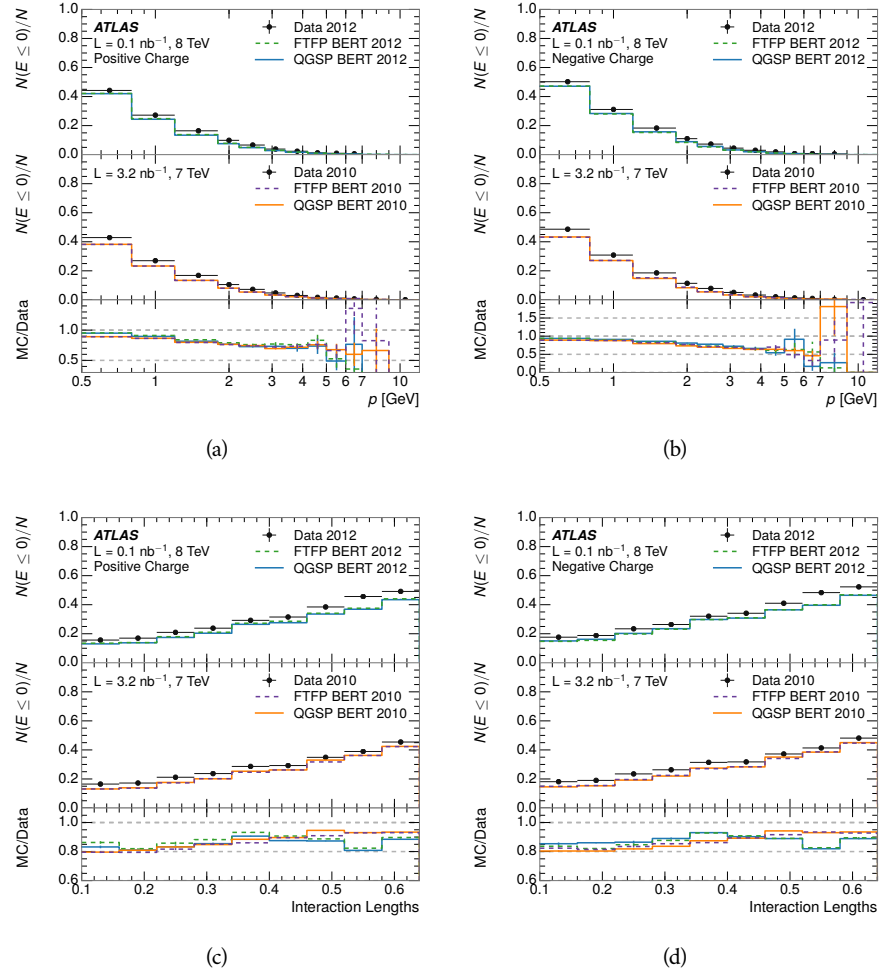


Figure 11: The fraction of tracks as a function (a, b) of momentum, (c, d) of interaction lengths with $E \leq 0$ for tracks with positive (on the left) and negative (on the right) charge.

GeV. This effect was also seen in the tails of the E/p distributions in Figure 10. This difference is likely due to modeling of coherent neutral particle radiation in **Pythia8** that overestimates the production of π^0 near the production of the charged particles. The discrepancy does not depend on η and thus is unlikely to be a mismodeling of the detector. This difference can be subtracted to form a corrected average E/p , as in Section 8.2.4.

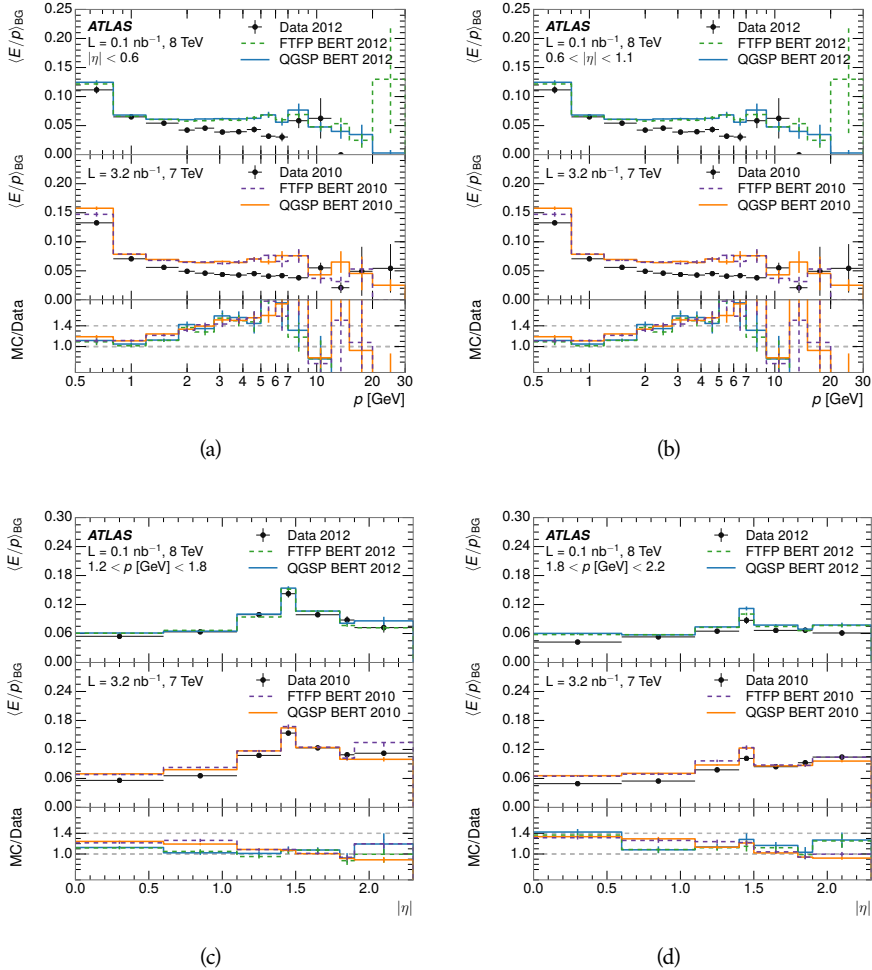


Figure 12: $\langle E/p \rangle_{\text{BG}}$ as a function of the track momentum for tracks with (a) $|\eta| < 0.6$, (b) $0.6 < |\eta| < 1.1$, and as a function of the track pseudorapidity for tracks with (c) $1.2 < p/\text{GeV} < 1.8$, (d) $1.8 < p/\text{GeV} < 2.2$.

8.2.4 CORRECTED RESPONSE

Figure 13 shows $\langle E/p \rangle_{\text{COR}}$ as a function of momentum for several bins of pseudorapidity. This corrected $\langle E/p \rangle_{\text{COR}} \equiv \langle E/p \rangle - \langle E/p \rangle_{\text{BG}}$ measures the average calorimeter response without the contamination of neutral particles. It is the most direct measurement of calorimeter response in that it is the energy measured for fully isolated hadrons. The correction is performed separately in data and simulation, so that the mismodeling of the neutral background in simulation

is removed from the comparison of response. The simulation overestimates the response at low momentum by about 5%, an effect that can be mostly attributed to the underestimation of the zero fraction mentioned previously. For $|\eta| < 0.6$, the data-simulation agreement has a larger discrepancy by about 5% for 2010 than 2012, although this is not reproduced in at higher pseudorapidity.

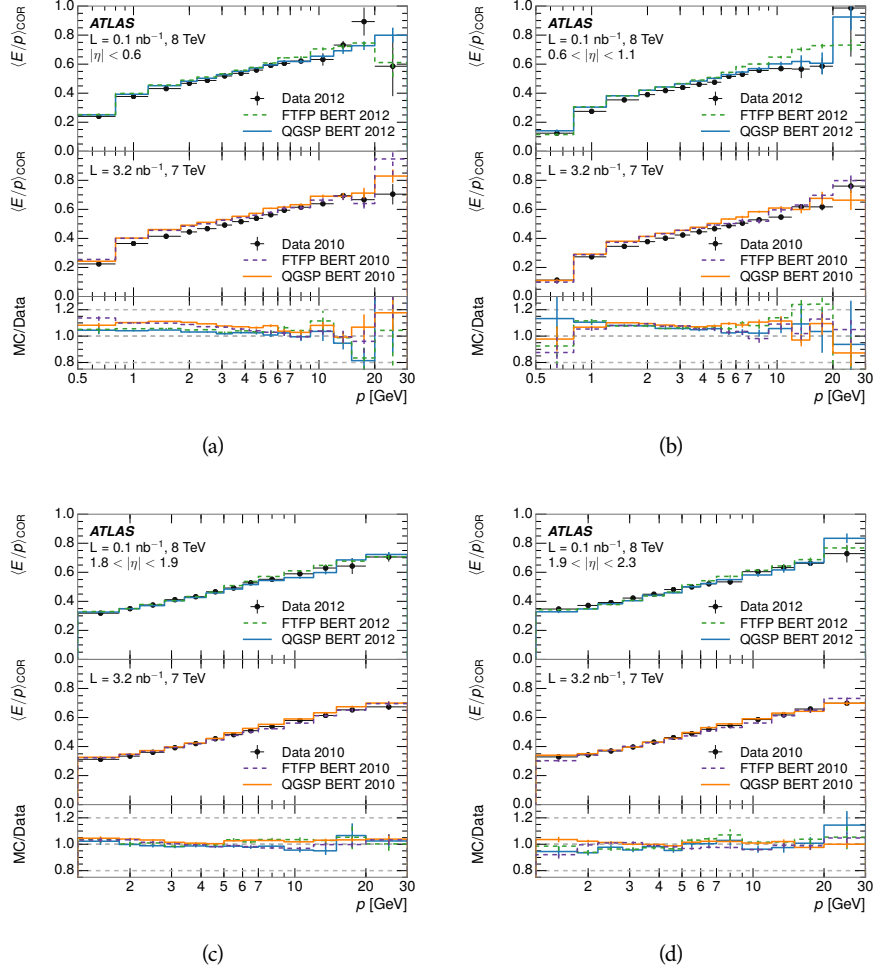


Figure 13: $\langle E/p \rangle_{\text{COR}}$ as a function of track momentum, for tracks with (a) $|\eta| < 0.6$, (b) $0.6 < |\eta| < 1.1$, (c) $1.8 < |\eta| < 1.9$, and (d) $1.9 < |\eta| < 2.3$.

The response measurement above used topological clustering at the EM scale, that is clusters were formed to measure energy but no corrections were applied to correct for expected effects like energy lost outside of the cluster or in uninstrumented material. It is also interesting to measure $\langle E/p \rangle_{\text{COR}}$ using local cluster weighted (LCW) energies, which accounts for those effects by calibrating the energy based on the properties of the cluster such as energy density and depth in the calorimeter. Figure 14 shows these distributions for tracks with zero or more clusters and separately for tracks with one or more clusters. The calibration moves the mean value of $\langle E/p \rangle_{\text{COR}}$ significantly closer to 1.0 as desired. The agreement between data and simulation improves noticeably when at least one cluster is required, as this removes the contribution from the mismodeling of

1017 the zero fraction. The good agreement in that case again demonstrates that the
 1018 difference in $\langle E/p \rangle_{\text{COR}}$ between data and simulation is caused predominantly
 1019 by the difference in zero fraction.

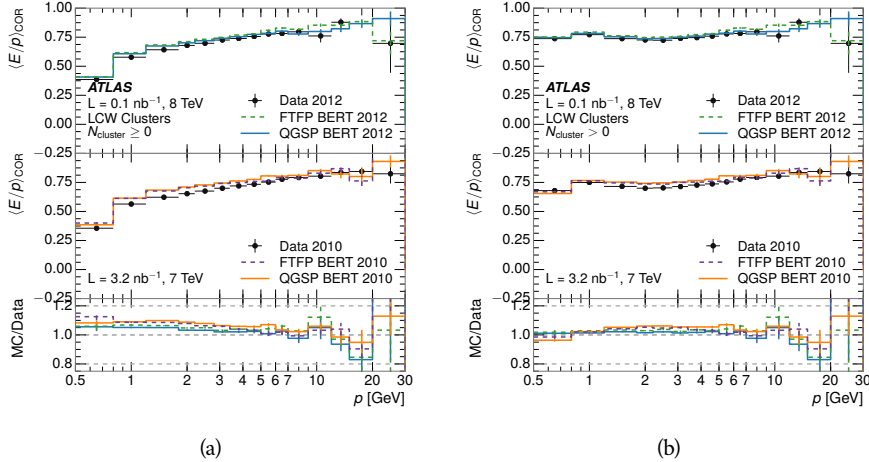


Figure 14: $\langle E/p \rangle_{\text{COR}}$ calculated using LCW-calibrated topological clusters as a function of track momentum for tracks with (a) zero or more associated topological clusters or (b) one or more associated topological clusters.

1020 8.2.5 ADDITIONAL STUDIES

1021 As has been seen in several measurements in previous sections, the simulation
 1022 does not correctly model the chance of a low momentum hadron to reach the
 1023 calorimeter. Because of the consistent discrepancy across pseudorapidity and
 1024 interaction lengths, this can be best explained by incomplete understanding of
 1025 hadronic interactions with the detector [10]. For example, a hadron that scat-
 1026 ters off of a nucleus in the inner detector can be deflected through a significant
 1027 angle and not reach the expected location in the calorimeter. In addition, these
 1028 interactions can produce secondary particles that are difficult to model.

1029 The requirement used throughout the previous sections on the number of
 1030 hits in the TRT reduces these effects by preferentially selecting tracks that do
 1031 not undergo nuclear interactions. It is interesting to check how well the sim-
 1032 ulation models tracks with low numbers of TRT hits, which selects tracks that
 1033 are more likely to have undergone a hadronic interaction. Figure 15 compares
 1034 the distributions with $N_{\text{TRT}} < 20$ to $N_{\text{TRT}} > 20$ for real and simulated particles.
 1035 As expected, the tracks with fewer hits are poorly modeled in the simulation as
 1036 $\langle E/p \rangle_{\text{COR}}$ differs by as much as 25% at low momentum.

1037 Another interesting aspect of the simulation is the description of antiprotons
 1038 at low momentum, where QGSP_BERT and FTFP_BERT have significant differ-
 1039 ences. This can be seen to have an effect in the inclusive response measurement
 1040 when separated into positive and negative charge. The $\langle E/p \rangle_{\text{COR}}$ distributions
 1041 for positive and negative particles are shown in Figure 16, where a small differ-
 1042 ence between QGSP_BERT and FTFP_BERT can be seen in the distribution for

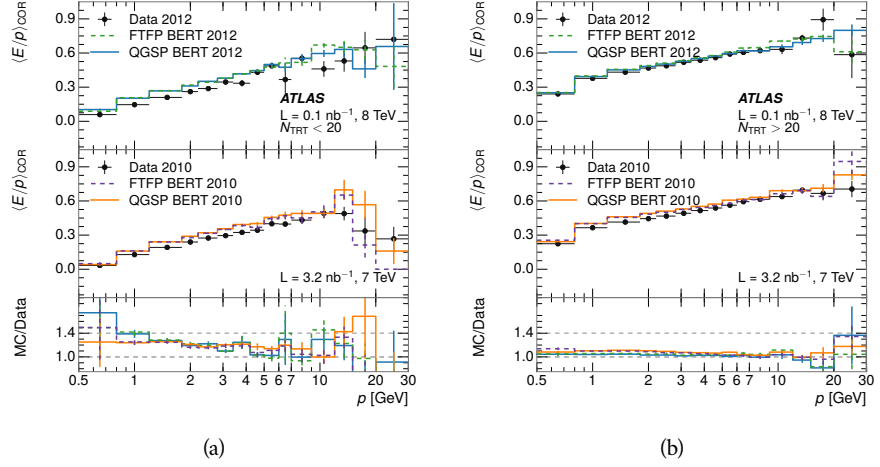


Figure 15: Comparison of the $\langle E/p \rangle_{\text{COR}}$ for tracks with (a) less than and (b) greater than 20 hits in the TRT.

negative tracks. This is demonstrated more clearly in Figure 17, which shows the E/p distribution in the two simulations separated by charge. There is a clear difference around $E/p > 1.0$, which can be explained by the additional energy deposited by the annihilation of the antiproton in the calorimeter that is modeled well only in FTFP_BERT. This is also explored with data using identified antiprotons in Section 8.3.

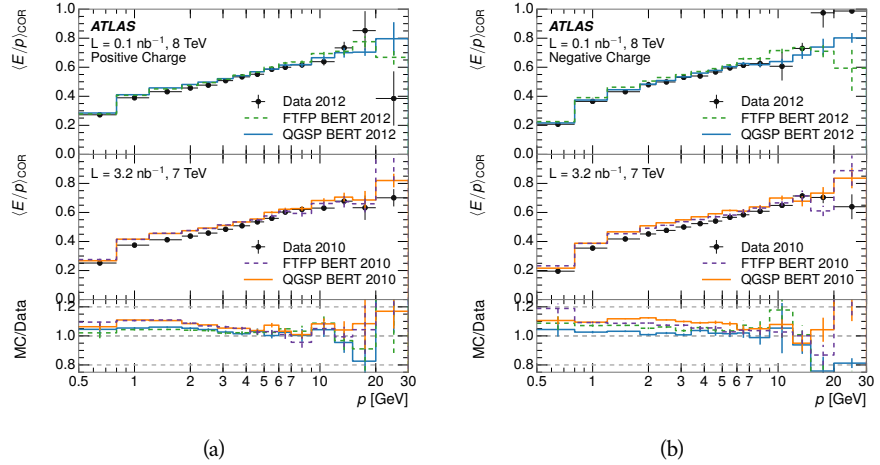


Figure 16: Comparison of the $\langle E/p \rangle_{\text{COR}}$ for (a) positive and (b) negative tracks as a function of track momentum for tracks with $|\eta| < 0.6$.

The $\langle E/p \rangle$ results in previous sections have considered the electromagnetic and hadronic calorimeters together as a single energy measurement, to emphasize the total energy deposited for a given particle. However, the deposits in each calorimeter are available separately and $\langle E/p \rangle$ can be constructed for each layer. As the layers are composed of different materials and are modeled separately in the detector geometry, confirmation that the simulation matches the data well

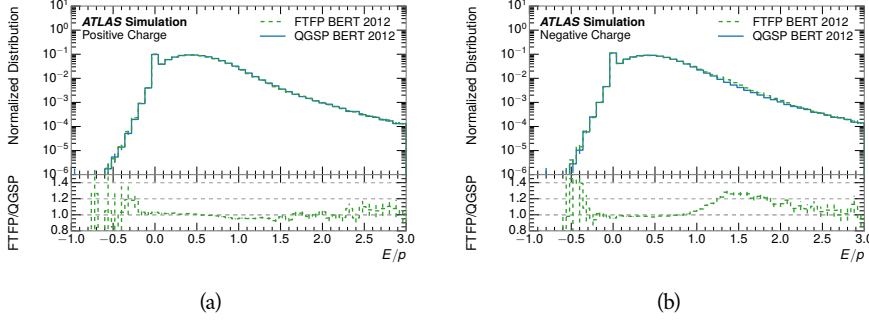


Figure 17: Comparison of the E/p distributions for (a) positive and (b) negative tracks with $0.8 < p/\text{GeV} < 1.2$ and $|\eta| < 0.6$, in simulation with the FTFP_BERT and QGSP_BERT physics lists.

in each layer adds confidence in both the description of hadronic interactions with the two different materials and also the geometric description of each.

The technique discussed in Section 8.2.3 for selecting minimally ionizing particle (MIP)s in the electromagnetic calorimeter is also useful in studying deposits in the hadronic calorimeter. Those MIPs deposit almost all of their energy exclusively in the hadronic calorimeter. Figure 18 shows $\langle E/p \rangle_{\text{RAW}}^{\text{Had}}$, where RAW indicates that no correction has been applied for neutral backgrounds and Had indicates that only clusters for the hadronic calorimeter are included. The RAW and COR versions of $\langle E/p \rangle$ in this case are the same, as the neutral background is negligible in that calorimeter layer. The distributions are shown both for the original EM scale calibration and after LCW calibration. The data and simulation agree very well in this comparison, except in the lowest momentum bin which has 5% discrepancy that has already been seen in similar measurements.

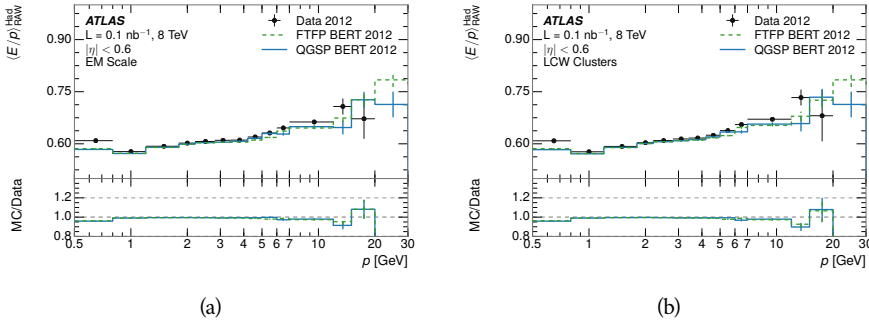


Figure 18: Comparison of the response of the hadronic calorimeter as a function of track momentum (a) at the EM-scale and (b) after the LCW calibration.

A similar comparison can be made in the electromagnetic calorimeter by selecting particles which have no associated energy in the hadronic calorimeter. These results are measured in terms of $\langle E/p \rangle_{\text{COR}}^{\text{EM}}$, where EM designates that only clusters in the electromagnetic calorimeter are included and COR designates that the neutral background is subtracted as the neutral background is present in this case. Figure 19 shows the analogous comparisons to Figure 18 in

1074 the electromagnetic calorimeter. In this case the disagreement between data and
 1075 simulation is more pronounced, with discrepancies as high as 5% over a larger
 1076 range of momenta. This level of discrepancy indicates that the description of
 1077 the electromagnetic calorimeter is actually the dominant source of discrepancy
 1078 in the combined distributions in Section 8.2.4.

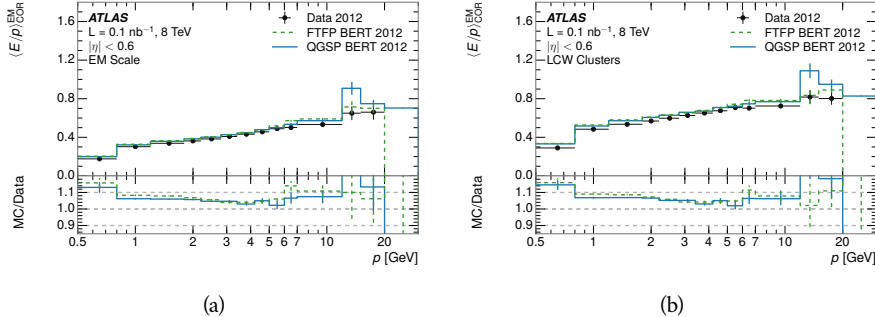


Figure 19: Comparison of the response of the EM calorimeter as a function of track momentum (a) at the EM-scale and (b) with the LCW calibration.

1079 **NOTE: There are more studies that I skipped for brevity that could be in-**
 1080 **cluded if interesting. E/p at different cluster threshold settings, E/p with**
 1081 **pileup, E/p with cells. I also left out a lot of eta bins that appear in the**
 1082 **paper so that this section didn't turn into 20 pages of plots.**

1083 8.3 IDENTIFIED PARTICLE RESPONSE

1084 The inclusive response measurement for hadrons can be augmented by measur-
 1085 ing the response for specific particle species. The simulation models each parti-
 1086 cle type separately, and understanding the properties of each is important in con-
 1087 straining the uncertainty on jets. In order to select and measure specific hadrons,
 1088 this section relies on the displaced decays of long-lived particles. Such decays
 1089 can be identified by reconstructing secondary vertices with a requirement on
 1090 mass. In particular, Λ , $\bar{\Lambda}$, and K_S^0 can be used to select a pure sample of protons,
 1091 antiprotons, and pions, respectively.

1092 8.3.1 DECAY RECONSTRUCTION

1093 The measurement of response for identified particles uses the same selection as
 1094 for inclusive particles (Section 8.1.3) with a few additions. Each event used is
 1095 required to have at least one secondary vertex, and the tracks are required to
 1096 match to that vertex rather than the primary vertex. Pions are selected from
 1097 decays of $K_S^0 \rightarrow \pi^+ \pi^-$, which is the dominant decay for K_S^0 to charged particles.
 1098 Protons are selected from decays of $\Lambda \rightarrow \pi^- p$ and antiprotons from $\bar{\Lambda} \rightarrow \pi^+ \bar{p}$,
 1099 which are similarly the dominant decays of Λ and $\bar{\Lambda}$ to charged particles. The
 1100 species of parent hadron in these decays is determined by reconstructing the
 1101 mass of the tracks associated to the secondary vertex. The sign of the higher

momentum decay particle can distinguish between Λ and $\bar{\Lambda}$, which of course have the same mass, as the proton or antiproton is kinematically favored to have higher momentum. Examples of the reconstructed masses used to select these decays are shown in Figure 20.

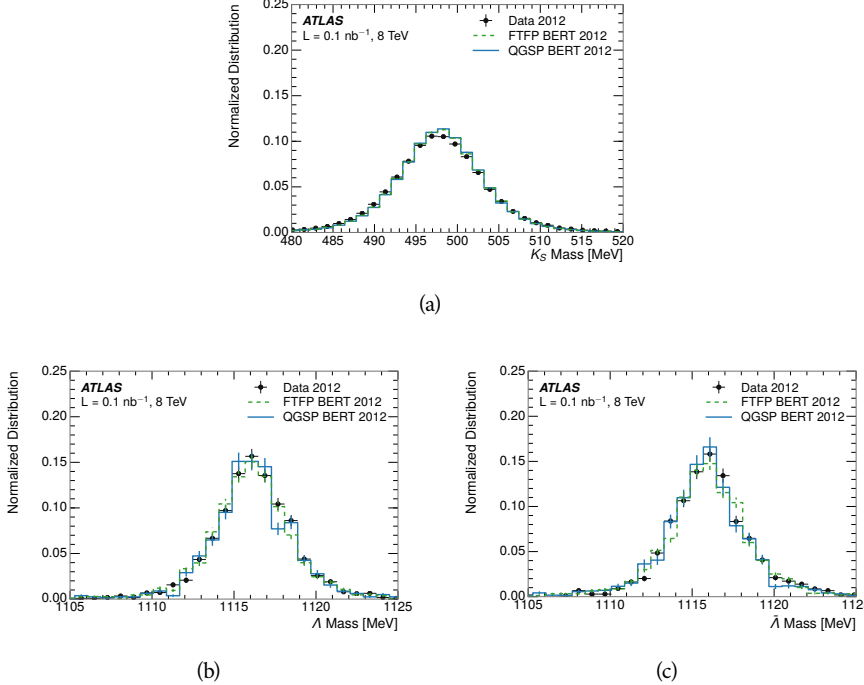


Figure 20: The reconstructed mass peaks of (a) K_S^0 , (b) Λ , and (c) $\bar{\Lambda}$ candidates.

The dominant backgrounds for the identified particle decays are nuclear interactions and combinatoric sources. These are suppressed by the kinematic requirements on the tracks as well as an additional veto which removes candidates that are consistent with both a Λ or $\bar{\Lambda}$ and a K_S^0 hypothesis, which is possible because of the different assumptions on particle mass in each case [11]. After these requirements, the backgrounds are found to be negligible compared to the statistical errors on these measurements.

8.3.2 IDENTIFIED RESPONSE

With these techniques the E/p distributions are extracted in data and simulation for each particle species and shown in Figure 21. These distributions are shown for a particular bin of E_a ($2.2 < E_a/\text{GeV} < 2.8$), rather than p . E_a is the energy available to be deposited in the calorimeter: for pions $E_a = \sqrt{p^2 + m^2}$, for protons $E_a = \sqrt{p^2 + m^2} - m$, and for antiprotons $E_a = \sqrt{p^2 + m^2} + m$. The features of the E/p distributions are similar to the inclusive case. There is a small negative tail from noise and a large fraction of tracks with zero energy from particles which do not reach the calorimeter. The long positive tail is noticeably more pronounced for antiprotons because of the additional energy generated by the annihilation in addition to the neutral background.

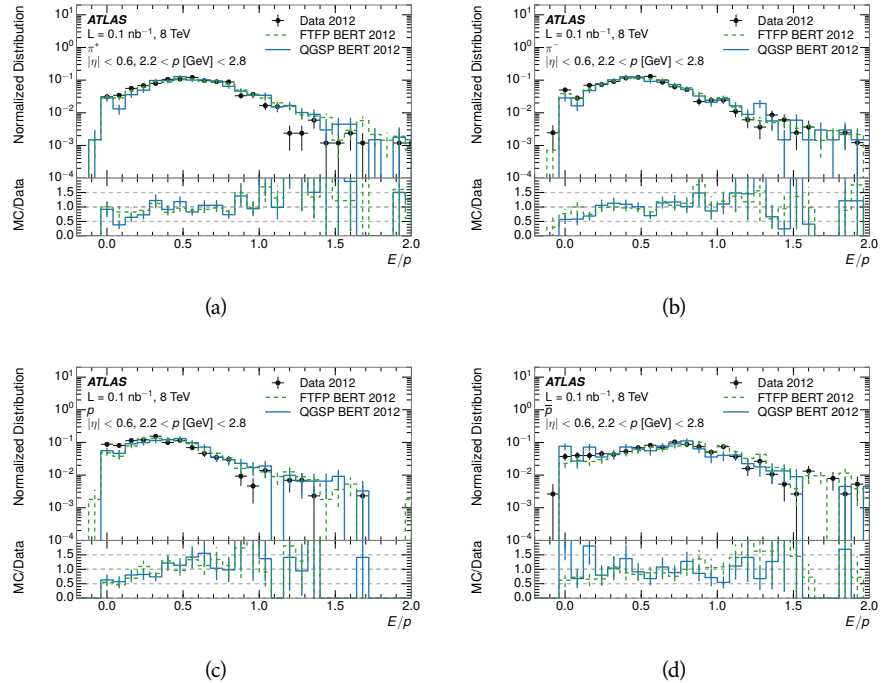


Figure 21: The E/p distribution for isolated (a) π^+ , (b) π^- , (c) proton, and (d) anti-proton tracks.

1124 The zero fraction is further explored in Figure 22 for pions and protons in data
 1125 and simulation. The simulation consistently underestimates the zero fraction
 1126 independent of particle species, which implies that this discrepancy is not caused
 1127 by the model of a particular species but rather a feature common to all.

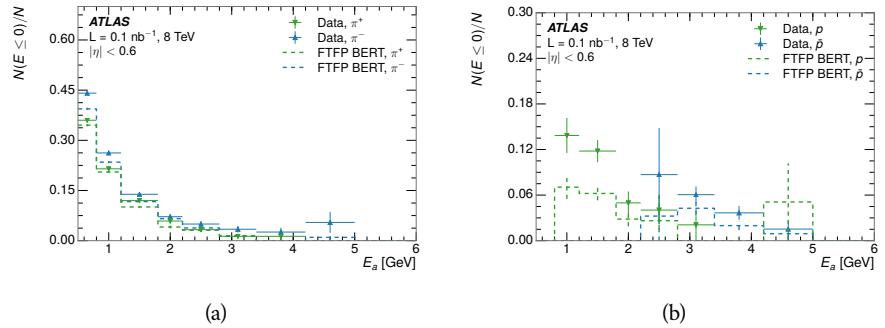


Figure 22: The fraction of tracks with $E \leq 0$ for identified (a) π^+ and π^- , and (b) proton and anti-proton tracks

1128 It is also interesting to compare the response between the different particle
 1129 species. One approach to do this is to measure the difference in $\langle E/p \rangle$ between
 1130 two types, which has the advantage of removing the neutral background. These
 1131 differences are shown in various combinations in Figure 23. The response for
 1132 π^+ is greater on average than the response to π^- because of a charge-exchange
 1133 effect which causes the production of additional neutral pions in the showers of

1134 π^+ [33]. The response for π^+ is also greater on average than the response to p ,
 1135 because a large fraction of the energy of π^+ hadrons is converted to an electro-
 1136 magnetic shower [34, 35]. However, the \bar{p} response is significantly higher than
 1137 the response to π^- because of the annihilation of the antiproton. FTFP_BERT
 1138 does a better job of modeling this effect than QGSP_BERT because of their differ-
 1139 ent descriptions of \bar{p} interactions with material.

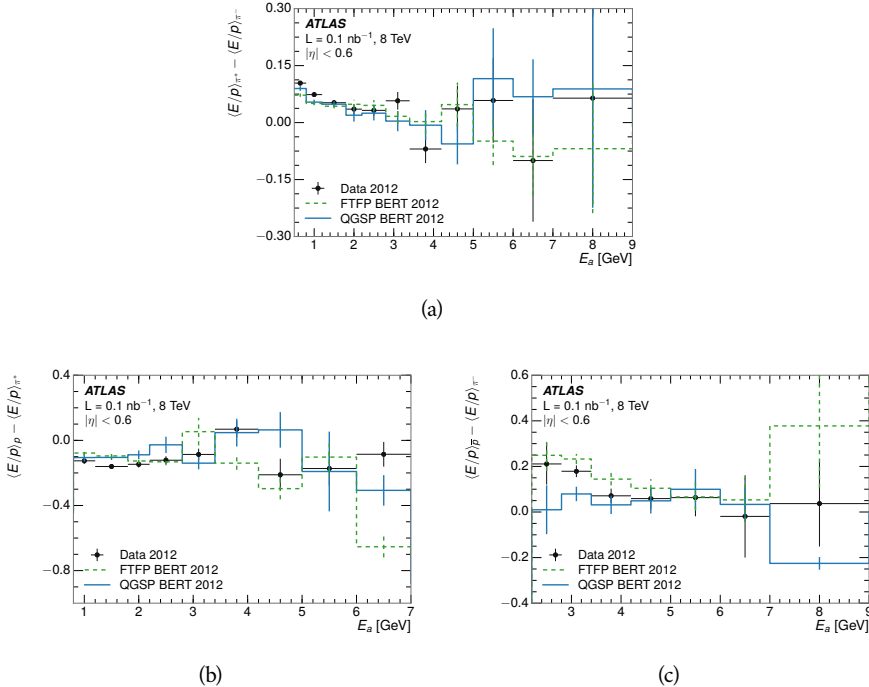


Figure 23: The difference in $\langle E/p \rangle$ between (a) π^+ and π^- (b) p and π^+ , and (c) \bar{p} and π^- .

1140 It is also possible to remove the neutral background from these response dis-
 1141 tributions using the same technique as in Section 8.2.3. The technique is largely
 1142 independent of the particle species and so can be directly applied to $\langle E/p \rangle$ for
 1143 pions. The $\langle E/p \rangle_{\text{COR}}$ distributions for pions are shown in Figure 24, which are
 1144 very similar to the inclusive results. The inclusive hadrons are comprised mostly
 1145 of pions, so this similarity is not surprising. It is also possible to see the small
 1146 differences between π^+ and π^- response here, where $\langle E/p \rangle_{\text{COR}}$ is higher on av-
 1147 erage for π^+ . The agreement between data and simulation is significantly worse
 1148 for the π^- distributions than for the π^+ , with a discrepancy greater than 10%
 1149 below 2-3 GeV.

1150 8.3.3 ADDITIONAL SPECIES IN SIMULATION

1151 The techniques above provide a method to measure the response separately for
 1152 only pions and protons. However the hadrons which forms jets include a num-
 1153 ber of additional species such as kaons and neutrons. The charged kaons are
 1154 an important component of the inclusive charged hadron distribution, which is
 1155 comprised of roughly 60-70% pions, 15-20% kaons, and 5-15% protons. These

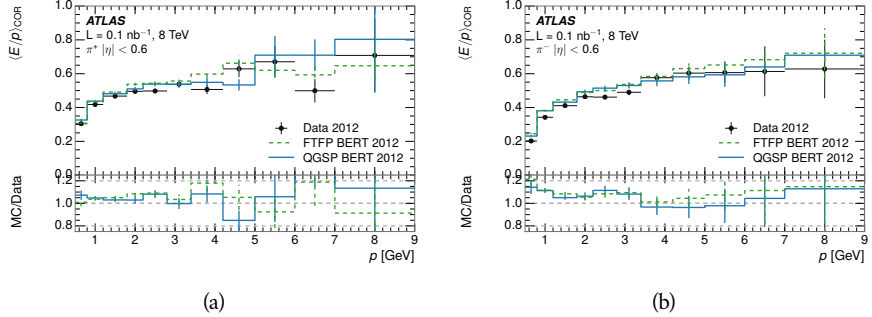


Figure 24: $\langle E/p \rangle_{\text{COR}}$ as a function of track momentum for (a) π^+ tracks and (b) π^- tracks.

are difficult to measure in data at the ATLAS detector, although a template subtraction technique has been proposed which may be effective with larger sample sizes [10]. The simulation of these particles includes noticeable differences in response at low energies, which are shown in Figure 25 for FTFP_BERT. The significant differences in response between low energy protons and antiprotons are accounted for above in the definitions of E_a .

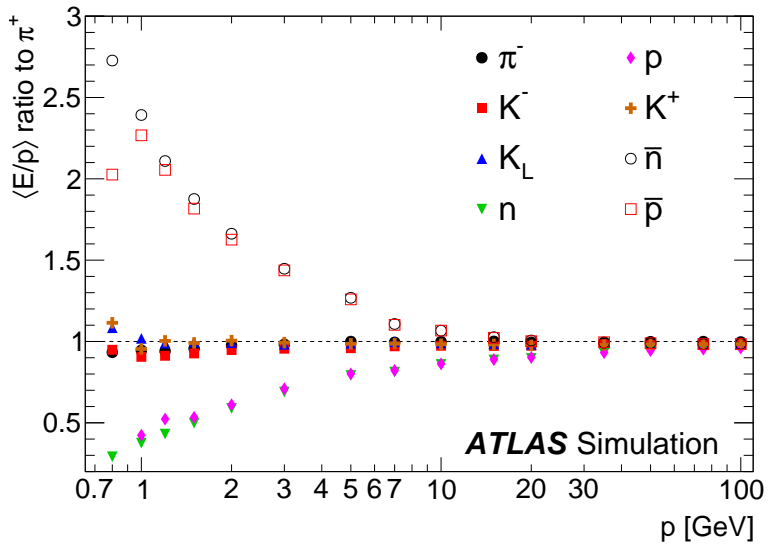


Figure 25: The ratio of the calorimeter response to single particles of various species to the calorimeter response to π^+ with the physics list FTFP_BERT.

1162 8.4 SUMMARY

These various measurements of calorimeter response shown above for data and simulation illuminate the accuracy of the simulation of hadronic interactions at the ATLAS detector. The results were done using 2010 and 2012 data at 7 and 8 TeV, but reflect the most current understanding of the detector alignment and geometry. A number of measurements focusing on a comparison between pro-

1168 tons and antiprotons suggest that FTFP_BERT models those interaction more
1169 accurately than QGSP_BERT. These measurements, among others, were the moti-
1170 vation to switch the default Geant4 simulation from FTFP_BERT to QGSP_BERT
1171 for all ATLAS samples.

1172 Even with these updates, there are a number of small, approximately 5%, dis-
1173 crepancies in response between the data and simulation at low energies. At
1174 higher energies the simulation of hadronic interactions is very consistent with
1175 data. Chapter 9 discusses how to use these observed differences to constrain the
1176 jet energy scale and its associated uncertainties.

1177

1178 JET ENERGY RESPONSE AND UNCERTAINTY

1179 9.1 MOTIVATION

1180 As jets form a major component of many physics analyses at ATLAS, it is crucial
 1181 to carefully calibrate the measurement of jet energies and to derive an uncer-
 1182 tainty on that measurement. These uncertainties have often been the dominant
 1183 systematic uncertainty in high-energy analyses at the LHC. Dijet and multijet
 1184 balance techniques provide a method to constrain the JES and its uncertainty in
 1185 data, and provide the default values used for ATLAS jet measurements at most
 1186 energies [36]. These techniques are limited by their reliance on measuring jets
 1187 in data, so they are statistically limited in estimating the jet energy scale at the
 1188 highest jet energies. This chapter presents another method for estimating the jet
 1189 energy scale and its uncertainty which builds up a jet from its components and
 1190 thus can be naturally extended to high jet momentum. Throughout this chapter
 1191 the jets studied are simulated using Pythia8 with the CT10 parton distribution
 1192 set [37] and the AU2 tune [14], and corrections are taken from the studies includ-
 1193 ing data and simulation in Chapter 8.

1194 As described in Section 7.2, jets are formed from topological clusters of energy
 1195 in the calorimeters using the anti- k_t algorithm. These clusters originate from a
 1196 diverse spectrum of particles, in terms of both species and momentum, leading to
 1197 significantly varied jet properties and response between jets of similar produced
 1198 momentum. Figure 26 shows the simulated distribution of particles within jets
 1199 at a few examples energies. The E/p measurements provide a thorough under-
 1200 standing of the dominant particle content of jets, the charged hadrons.

1201 9.2 UNCERTAINTY ESTIMATE

1202 Simulated jets are not necessarily expected to correctly model the energy de-
 1203 posits in the calorimeters, because of the various discrepancies discussed in Chap-
 1204 ter 8. To evaluate a jet energy response, the simulated jet energies are compared
 1205 to a corrected jet built up at the particle level. Each cluster in a jet is associated
 1206 to the truth particle which deposited it, and the energy in that cluster is then
 1207 corrected for a number of effects based on measurements in data. The primary
 1208 corrections come from the single hadron response measurements in addition to
 1209 response measured using the combined test beam which covers higher momen-
 1210 tum particles [38]. These corrections include both a shift (Δ), in order to make
 1211 the simulation match the average response in data, and an uncertainty (σ) asso-
 1212 ciated with the ability to constrain the difference between data and simulation.
 1213 Some of the dominant sources of uncertainty are itemized in Table 2 with typi-
 1214 cal values, and the full list considered is described in detail in the associated pa-

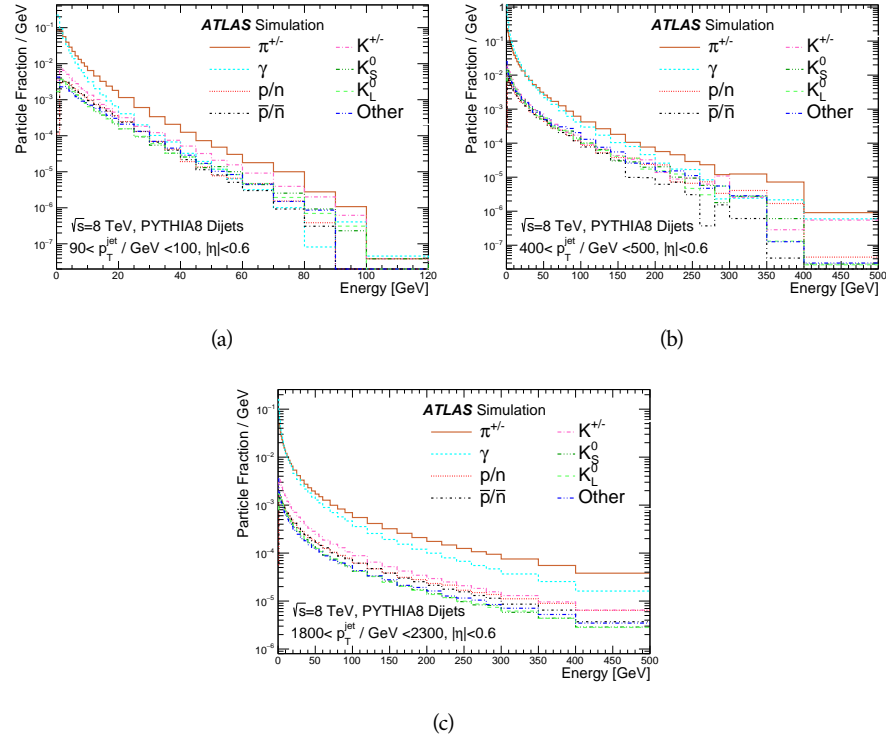


Figure 26: The spectra of true particles inside anti- k_t , $R = 0.4$ jets with (a) $90 < p_T/\text{GeV} < 100$, (b) $400 < p_T/\text{GeV} < 500$, and (c) $1800 < p_T/\text{GeV} < 2300$.

1215 per [10]. These uncertainties cover differences between the data and simulation
 1216 in the modeling of calorimeter response to a given particle. No uncertainties are
 1217 added for the difference between particle composition of jets in data and simu-
 1218 lation.

1219 From these terms, the jet energy scale and uncertainty is built up from indi-
 1220 vidual energy deposits in simulation. Each uncertainty term is treated indepen-
 1221 dently, and are taken to be gaussian distributed. The resulting scale and uncer-
 1222 tainty is shown in Figure 27, where the mean response is measured relative to
 1223 the calibrated energy reported by simulation. The dominant uncertainties come
 1224 from the statistical uncertainties on the E/p measurements at lower energies and
 1225 the additional uncertainty for out of range measurements at higher energies. The
 1226 total uncertainty from this method at intermediate jet energies is comparable to
 1227 other simulation-based methods [39] and is about twice as large as in-situ meth-
 1228 ods using data [36]. This method is the only one which provides an estimation
 1229 above 1.8 TeV, however, and so is still a crucial technique in analyses that search
 1230 for very energetic jets.

1231 These techniques can also be used to measure the correlation between bins of
 1232 average reconstructed jet momentum across a range of p_T and $|\eta|$, where cor-
 1233 relations are expected because of a similarity in particle composition at similar
 1234 energies. Figure 28 shows these correlations, where the uncertainties on jets in
 1235 neighboring bins are typically between 30% and 60% correlated. The uncertainty
 1236 on all jets becomes significantly correlated at high energies and larger pseudora-

Abbrev.	Description	Δ (%)	σ (%)
In situ E/p	The comparison of $\langle E/p \rangle_{\text{COR}}$ as described in Chapter 8 with statistical uncertainties from 500 MeV to 20 GeV.	0-3	1-5
CTB	The main $\langle E/p \rangle$ comparison uncertainties, binned in p and $ \eta $, as derived from the combined test beam results, from 20 to 350 GeV [38].	0-3	1-5
E/p Zero Fraction	The difference in the zero-fraction between data and MC simulation from 500 MeV to 20 GeV.	5-25	1-5
E/p Threshold	The uncertainty in the EM calorimeter response from the potential mismodeling of threshold effects in topological clustering.	0	0-10
Neutral	The uncertainty in the calorimeter response to neutral hadrons based on studies of physics model variations.	0	5-10
K_L	An additional uncertainty in the response to neutral K_L in the calorimeter based on studies of physics model variations.	0	20
E/p Misalignment	The uncertainty in the p measurement from misalignment of the ID.	0	1
Hadrons, $p > 350$ GeV	A flat uncertainty for all particles above the energy range or outside the longitudinal range probed with the combined test beam.	0	10

Table 2: The dominant sources of corrections and systematic uncertainties in the [JES](#) estimation technique, including typical values for the correcting shift (Δ) and the associated uncertainty (σ).

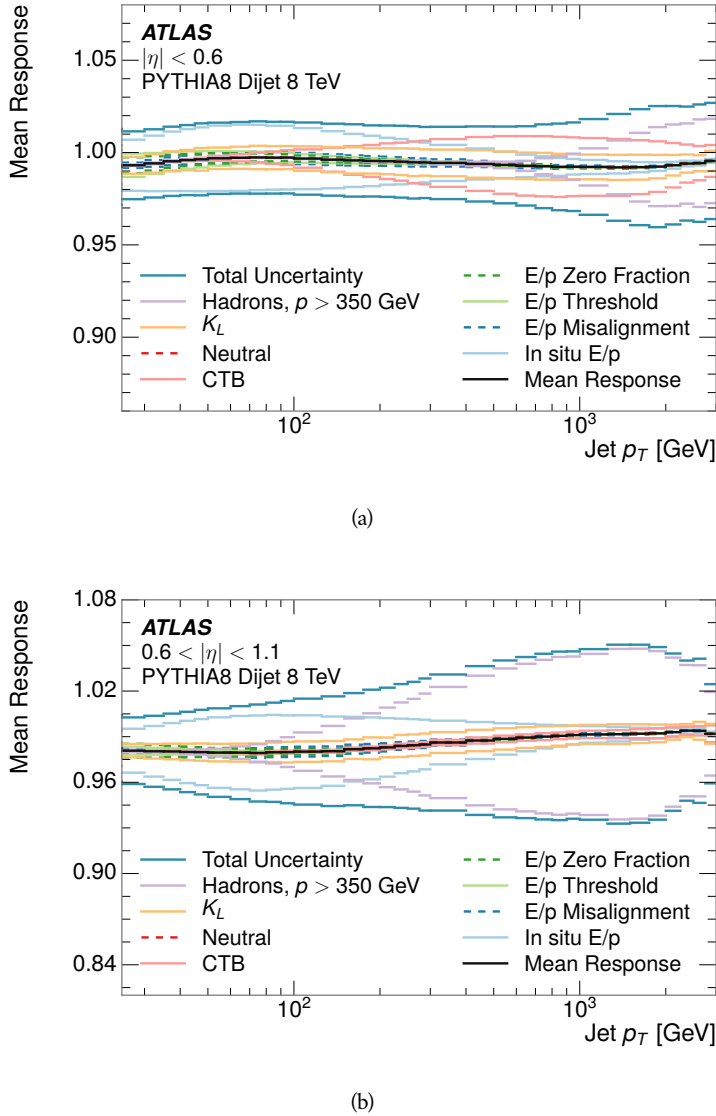


Figure 27: The [JES](#) uncertainty contributions, as well as the total [JES](#) uncertainty, as a function of jet p_T for (a) $|\eta| < 0.6$ and (b) $0.6 < |\eta| < 1.1$.

1237 pidities, when the uncertainty becomes dominated by the single term reflecting
 1238 out of range particles.

1239 9.3 SUMMARY

1240 The technique described above provides a jet energy scale and uncertainty by
 1241 building up jet corrections from the energy deposits of constituent particles. The
 1242 E/p measurements are crucial in providing corrections for the majority of parti-
 1243 cles in the jets. The uncertainty derived this way is between 2 and 5% and is about
 1244 twice as large at corresponding momentum than jet balance methods. However
 1245 this is the only uncertainty available for very energetic jets using 2012 data and
 1246 simulation, and repeating this method with Run 2 data and simulation will be

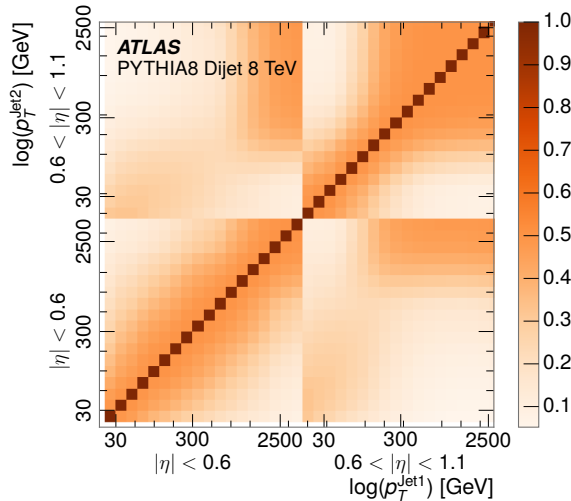


Figure 28: The **JES** correlations as a function of jet p_T and $|\eta|$ for jets in the central region of the detector.

¹²⁴⁷ important in providing an uncertainty for the most energetic jets in 13 TeV collisions.
¹²⁴⁸

1249

PART V

1250

SEARCH FOR LONG-LIVED PARTICLES

1251

You can put some informational part preamble text here.

1252

1253 LONG-LIVED PARTICLES IN ATLAS

1254 As discussed in Section 2.3, various limitations in the SM suggest a need for new
 1255 particles at the TeV scale. A wide range of extensions to the Standard Model
 1256 predict that these new particles can have lifetimes greater than approximately
 1257 one-hundredth of a nanosecond. These include theories with universal extra-
 1258 dimensions [40, 41], with new fermions [42], and with leptoquarks [43]. Many
 1259 Supersymmetry (SUSY) theories also produce these Long-Lived Particles (LLPs),
 1260 in both R-Parity violating [44–46] and R-Parity conserving [47–50] formula-
 1261 tions. Split supersymmetry [51, 52], for example, predicts long-lived gluinos
 1262 with $O(\text{TeV})$ masses. This search focuses specifically on the SUSY case, but many
 1263 of the results are generic to any model with LLPs.

1264 Long-lived gluinos or squarks carry color-charge and will thus hadronize into
 1265 color neutral bound states called R-Hadrons. These are composit particles like
 1266 the usual hadrons but with one supersymmetric constituent, for example $\tilde{g}q\bar{q}$
 1267 and $\tilde{q}\bar{q}$. Through this hadronization process, the neutral gluino can acquire a
 1268 charge. Gluino pair production, $pp \rightarrow \tilde{g}\tilde{g}$ has the largest cross sectional increase
 1269 with the increase in energy to 13 TeV, and so this search focuses on gluino R-
 1270 Hadrons. Planned future updates will extend the case to explicitly include squark
 1271 and chargino models, but the method covers any long-lived, charged, massive
 1272 particle.

1273 10.1 EVENT TOPOLOGY

1274 The majority of SUSY models predict that gluinos will be produced in pairs at
 1275 the LHC, through processes like $pp \rightarrow q\bar{q} \rightarrow \tilde{g}\tilde{g}$ and $pp \rightarrow gg \rightarrow \tilde{g}\tilde{g}$, where the
 1276 gluon mode dominates for the collision energy and gluino masses considered
 1277 for this search. During their production, the long-lived gluinos hadronize into
 1278 color singlet bound states including $\tilde{g}q\bar{q}$, $\tilde{g}qqq$, and even $\tilde{g}g$ [53]. The probability
 1279 to form the gluon-only bound states is a free parameter usually taken to be 0.1,
 1280 while the meson states are favored among the R-Hadrons [54]. The charged and
 1281 neutral states are approximately equally likely for mesons, so the R-Hadrons will
 1282 be charged roughly 50% of the time.

1283 These channels produce R-Hadrons with large p_T , comparable to their mass,
 1284 so that they typically propagate with $0.2 < \beta < 0.9$ [54]. The fragmentation that
 1285 produces that hadrons is very hard, so the jet structure around the R-Hadron
 1286 is minimal, with less than 5 GeV of summed particle momentum expected in a
 1287 cone of $\Delta R < 0.25$ around the R-Hadron [54]. After hadronization, depending
 1288 on the gluino lifetime, the R-Hadrons then decay into hadrons and a LSP [53].

1289 In summary, the expected event for pair-produced long-lived gluinos is very
 1290 simple: two isolated, high-momentum R-Hadrons that propagate through the
 1291 detector before decaying into jets. The observable features of such events depend

1292 strongly on the interaction of the R-Hadron with the material of the detector and
 1293 also its lifetime. Section 10.1.1 describes the interactions of R-Hadrons which
 1294 reach the various detector elements in ATLAS and Section 10.1.2 provides a sum-
 1295 mary of the observable event descriptions for R-Hadrons of various lifetimes.

1296 10.11 DETECTOR INTERACTIONS

1297 After approximately 0.2 ns, the R-Hadron reaches the pixel detector. If charged,
 1298 it deposits energy into the material through repeated single collisions that result
 1299 in ionization of the silicon substrate [55]. Because of its comparatively low β ,
 1300 the ionization energy can be significantly greater than expected for SM particles
 1301 because the most-probable energy loss grows significantly as β decreases [55].
 1302 This large ionization can be measured through the time over threshold (ToT) read
 1303 out from the pixel detector as described in Section 7.1.1.2. Large ionization in
 1304 the inner detector is one of the major characteristic features of LLPs.

1305 Throughout the next few nanoseconds, the R-Hadron propagates through the
 1306 remainder of the inner detector. A charged R-Hadron will provide hits in each
 1307 of these systems as would any other charged particle, and can be reconstructed
 1308 as a track. The track reconstruction provides a measurement of its trajectory
 1309 and thus its momentum as described in Section 7.1. The large momentum is
 1310 another characteristic feature of massive particles produced at the LHC. **Note: At**
 1311 **this point I am failing to mention that the TRT provides a possible dE/dx**
 1312 **measurement, because no one uses it as far as I know.**

1313 As of roughly 20 ns, the R-Hadron enters the calorimeter where it interacts
 1314 hadronically with the material. Because of its large mass and momentum, the
 1315 R-Hadron does not typically stop in the calorimeter, but rather deposits a small
 1316 fraction of its energy through repeated interactions with nucleons. The proba-
 1317 bility of interaction between the gluino itself and a nucleon is low because the
 1318 cross section drops off with the inverse square of its mass, so the interactions are
 1319 primarily governed by the light constituents [56]. Each of these interactions can
 1320 potentially change that quark content and thus change the sign of the R-Hadron,
 1321 so that the charge at exit is typically uncorrelated with the charge at entry [54].
 1322 The total energy deposited in the calorimeters during the propagation is small
 1323 compared to the kinetic energy of the R-Hadron, around 20-40 GeV, so that
 1324 E/p is typically less than 0.1 [54].

1325 Then, 30 ns after the collision, it reaches the muon system, where it again
 1326 ionizes in the material if charged and can be reconstructed as a muon track. Be-
 1327 cause of the charge-flipping interactions in the calorimeter, this track may have
 1328 the opposite sign of the track reconstructed in the inner detector, or there may
 1329 be a track present when there was none in the inner detector and vice-versa. The
 1330 propagation time at the typically lower β results in a significant delay compared
 1331 to muons, and that delay can be assessed in terms of a time-of-flight measure-
 1332 ment. Because of the probability of charge-flip and late arrival, there is a signif-
 1333 icant chance that an R-Hadron which was produced with a charge will not be
 1334 identified as a muon. The long time-of-flight is another characteristic feature of
 1335 R-Hadrons which are reconstructed as muons.

1336 10.1.2 LIFETIME DEPENDENCE

1337 The above description assumed a lifetime long enough for the R-Hadron to exit
 1338 the detector, which through this search is referred to as “stable”, even though
 1339 the particle may decay after exiting the detector. There are several unique sig-
 1340 natures at shorter lifetimes where the R-Hadron decays in various parts of the
 1341 inner detector; these lifetimes are referred to as “metastable”.

1342 The shortest case where the R-Hadron is considered metastable is for life-
 1343 times around 0.01 ns, where the particle decays before reaching any of the de-
 1344 tector elements. Although the R-Hadrons are produced opposite each other in
 1345 the transverse plane, each R-Hadron decays to a jet and an [LSP](#). The [LSPs](#) are not
 1346 measured, so the produced jets can be significantly imbalanced in the transverse
 1347 plane which results in large missing energy. That missing energy can be used
 1348 to trigger candidate events, and provides the most efficient trigger option for
 1349 shorter lifetimes. Additionally, the precision of the tracking system allows the
 1350 displaced vertex of the R-Hadron decay to be reconstructed from the charged
 1351 particles in the jet. The distance of that vertex from the interaction point can
 1352 be used to distinguish R-Hadron decays from other processes. Figure 29 shows
 1353 a schematic diagram of an example R-Hadron event with such a lifetime. The
 1354 diagram is not to scale, but instead illustrates the detector interactions in the
 1355 pixel detector, calorimeters, and muon system. It includes a representation of
 1356 the charged R-Hadron and the neutral R-Hadron, as well as the [LSPs](#) and jets
 1357 (shown as charged hadrons) produced in the decay. Neutral hadrons may also
 1358 be produced in the decay but are not depicted. Previous searches on [ATLAS](#) have
 1359 used the displaced vertex to target [LLP](#) decays [57].

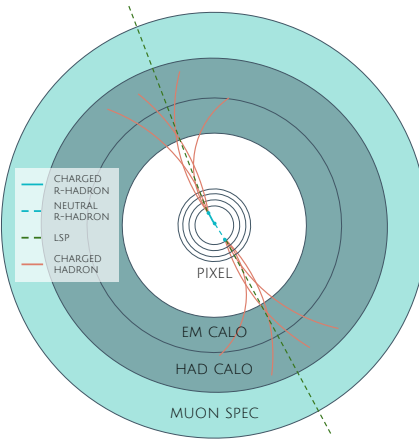


Figure 29: A schematic diagram of an R-Hadron event with a lifetime around 0.01 ns.
 The diagram includes one charged R-Hadron (solid blue), one neutral R-Hadron (dashed blue), [LSPs](#) (dashed green) and charged hadrons (solid orange).
 The pixel detector, calorimeters, and muon system are illustrated but not to scale.

1360 The next distinguishable case occurs at lifetimes greater than 0.1 ns, where
 1361 the R-Hadron forms a partial track in the inner detector. If the decay products
 1362 are sufficiently soft, they may not be reconstructed, and this forms a unique sig-

1363 nature of a disappearing track. An example of such an event is illustrated in
 1364 Figure 30, which shows the short track in the inner detector and the undetected
 1365 soft charged hadron and LSP that are produced. A dedicated search on ATLAS used
 1366 the disappearing track signature to search for LLP in Run 1 [58]. **zNote: might**
 1367 **not be worth mentioning the disappearing track here since it is actually a**
 1368 **chargino search, the soft pion is pretty unique to charginos.**

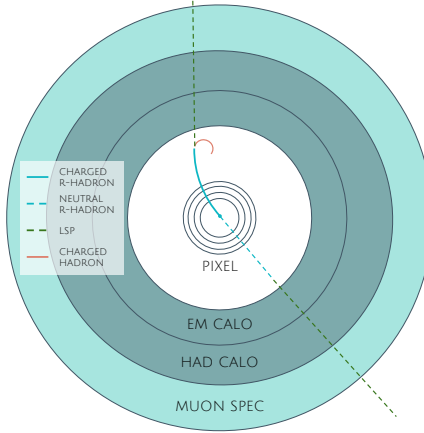


Figure 30: A schematic diagram of an R-Hadron event with a lifetime around 4 ns. The diagram includes one charged R-Hadron (solid blue), one neutral R-Hadron (dashed blue), LSPs (dashed green) and a charged hadron (solid orange). The pixel detector, calorimeters, and muon system are illustrated but not to scale.

1369 If the decay products are not soft, the R-Hadron daughters form jets, resulting
 1370 in an event-level signature of up to two high-momentum tracks, jets, and signif-
 1371 icant missing energy. The missing energy has the same origin as in the case of
 1372 0.01 ns lifetimes, from the decay to unmeasured particles, and again can be large.
 1373 The high-momentum tracks will also have the characteristically high-ionization
 1374 of massive, long-lived particles in the inner detector. Figure 31 illustrates an ex-
 1375 ample event with one charged R-Hadron which decays after approximately 10 ns,
 1376 and shows how the jets from the decay can still be reconstructed in the calorime-
 1377 ter. Several previous searches on ATLAS from Run 1 have used this signature to
 1378 search for R-Hadrons [59, 60], including a dedicated search for metastable parti-
 1379 cles [61].

1380 If the lifetime is longer than several nanoseconds, in the range of 15-30 ns,
 1381 the R-Hadron decay can occur in or after the calorimeters, but prior to reaching
 1382 the muon system. This case is similar to the above, although the jets may not be
 1383 reconstructed, and is covered by many of the same search strategies. The events
 1384 still often have large missing energy, although it is generated through different
 1385 mechanisms. The R-Hadrons do not deposit much energy in the calorimeters, so
 1386 a neutral R-Hadron will not enter into the missing energy calculation. A charged
 1387 R-Hadron opposite a neutral R-Hadron will thus generate significant missing en-
 1388 ergy, and close to 50% of pair-produced R-Hadron events fall into this category.
 1389 If both R-Hadrons are neutral then the missing energy will be low because nei-
 1390 ther is detected. Two charged R-Hadrons will also result in low missing energy
 1391 because both are reconstructed as tracks and will balance each other in the trans-

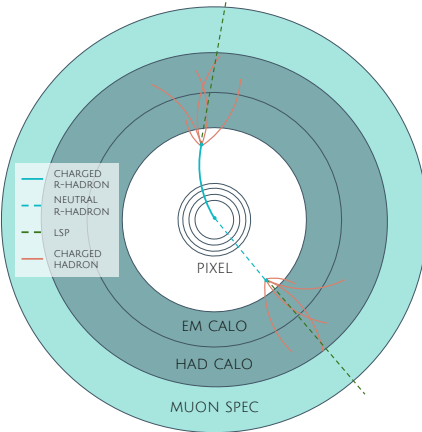


Figure 31: A schematic diagram of an R-Hadron event with a lifetime around 5 ns. The diagram includes one charged R-Hadron (solid blue), one neutral R-Hadron (dashed blue), LSPs (dashed green) and charged hadrons (solid orange). The pixel detector, calorimeters, and muon system are illustrated but not to scale.

1392 verse plane. A small fraction of the time, one of the charged R-Hadron tracks may
 1393 fail quality requirements and thus be excluded from the missing energy calcula-
 1394 tion and again result in significant missing energy. Figure 32 illustrates another
 1395 example event with one charged R-Hadron which decays after approximately 20
 1396 ns, and shows how the jets from the decay might not be reconstructed.

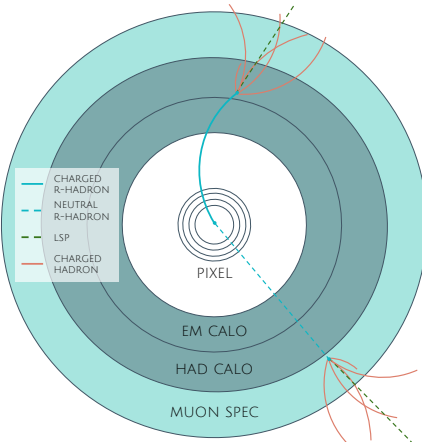


Figure 32: A schematic diagram of an R-Hadron event with a lifetime around 20 ns. The diagram includes one charged R-Hadron (solid blue), one neutral R-Hadron (dashed blue), LSPs (dashed green) and charged hadrons (solid orange). The pixel detector, calorimeters, and muon system are illustrated but not to scale.

1397 The longest lifetimes, the stable case, has all of the features of the 30-50 ns case
 1398 but with the addition of muon tracks for any R-Hadrons that exit the calorimeter
 1399 with a charge. That muon track can provide additional information from time-
 1400 of-flight measurements to help identify LSPs. An example of the event topology
 1401 for one charged and one neutral stable R-Hadron is shown in Figure 33. Some
 1402 searches on ATLAS have included this information to improve the search reach
 1403 for stable particles [60, 62].

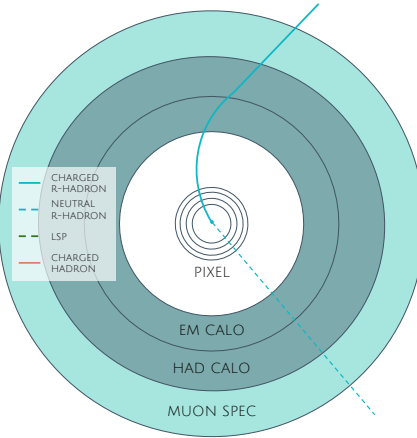


Figure 33: A schematic diagram of an R-Hadron event with a lifetime around 20 ns. The diagram includes one charged R-Hadron (solid blue) and one neutral R-Hadron (dashed blue). The pixel detector, calorimeters, and muon system are illustrated but not to scale.

1404 10.2 SIMULATION

1405 All of the event topologies discussed above are explored by simulations of R-
 1406 Hadron events in the [ATLAS](#) detector. A large number of such samples are gen-
 1407 erated to determine signal efficiencies, to measure expected yields, and to esti-
 1408 mate uncertainties. The primary interaction, pair production of gluinos with
 1409 masses between 400 and 3000 GeV, is simulated using [Pythia 6.4.27](#) [63]
 1410 with the AUET2B [64] set of tuned parameters for the underlying event and
 1411 the CTEQ6L1 [37] parton distribution function ([PDF](#)) set. The simulated inter-
 1412 actions include a modeling of pileup by adding secondary, minimum bias in-
 1413 teractions from both the same (in-time pileup) and nearby (out-of-time pileup)
 1414 bunch crossings. This event generation is then augmented with a dedicated
 1415 hadronization routine to hadronize the long-lived gluinos into final states with
 1416 R-Hadrons [65], with the probability to form a gluon-gluino bound set at 10% [66].

1417 The cross sections used for these processes are calculated at next-to-leading
 1418 order ([NLO](#)) in the strong coupling constant with a resummation of soft-gluon
 1419 emmission at next-to-leading logarithmic ([NLL](#)) [67–71]. The nominal predic-
 1420 tions and the uncertainties for each mass point are taken from an envelope of
 1421 cross-section predictions using different [PDF](#) sets and factorization and renor-
 1422 malization scales [72].

1423 The R-Hadrons then undergo a full detector simulation [], where the interac-
 1424 tions of the R-Hadrons with the material of the detector are described by dedi-
 1425 cated [Geant4](#) [7] routines. These routines model the interactions described in
 1426 Section 10.1.1, including the ionizing interactions in the silicon modules of the
 1427 inner detector and the R-Hadron-nucleon interactions in the calorimeters [73,
 1428 74]. The specific routine chosen to describe the interactions of the R-Hadrons
 1429 with nucleons, the “generic model”, uses a pragmatic approach where the scatter-
 1430 ing cross section is taken to be a constant 12 mb per light quark. In this model

1431 the gluino itself does not interact at all except through its role as a reservoir of
1432 kinetic energy.

1433 The lifetimes of these R-Hadrons are then simulated at several working points,
1434 $\tau = 0.1, 1.0, 3.0, 10, 30, 50$ and detector stable, where the particle is required to
1435 decay after propagating for a time compatible with its lifetime. Only one decay
1436 mode is simulated for these samples, $\tilde{g} \rightarrow q\bar{q}\tilde{\chi}_1^0$ with the neutralino mass set to
1437 100 GeV, which is chosen because it has the highest sensitivity among all of the
1438 modes studied in previous searches [61]. Heavier neutralinos have similar results
1439 but generate less missing energy which reduces the efficiency of triggering.

1440 All of the simulated events are then reconstructed using the same software
1441 used for collision data. The fully reconstructed events are then reweighted to
1442 match the distribution of initial state radiation in an alternative sample of events,
1443 generated with MG5_aMC@NLO [75], which has a more accurate description of ra-
1444 diate effects than Pythia6. This reweighting provides a more accurate descrip-
1445 tion of the momentum of the gluino-gluino system and is important in modeling
1446 the efficiency of triggering and offline event selection.

1447

1448 EVENT SELECTION

1449 The [LLPs](#) targeted by this search differ in their interactions with the detector from
 1450 [SM](#) particles primarily because of their large mass. When produced at the ener-
 1451 gies available at the [LHC](#), that large mass results in a low β (typically $0.2 < \beta <$
 1452 0.9). Such slow-moving particles heavily ionize in detector material. Each layer
 1453 of the pixel detector provides a measurement of that ionization, through [ToT](#), as
 1454 discussed in Section 6.3.1. The ionization in the pixel detector, quantified in
 1455 terms of dE/dx , provides the major focus for this search technique, along with
 1456 the momentum measured in the entire inner detector. It is effective both for its
 1457 discriminating power and its use in reconstructing a particle's mass, and it can
 1458 be used for a wide range of masses and lifetimes as discussed in Section 10.1.2.
 1459 However dE/dx needs to be augmented with a few additional selection require-
 1460 ments to provide a mechanism for triggering and to further reduce backgrounds.

1461 Ionization itself is not currently accessible for triggering, so this search in-
 1462 stead relies on E_T^{miss} to trigger signal events. Although triggering on E_T^{miss} can
 1463 be inefficient, E_T^{miss} is often large for many production mechanisms of [LLPs](#), as
 1464 discussed in Section 10.1.

1465 The use of ionization to reject [SM](#) backgrounds relies on well-measured, high-
 1466 momentum tracks, so some basic requirements on quality and kinematics are
 1467 placed on the tracks considered in this search. These quality requirements have
 1468 been significantly enhanced in Run 2 by a newly introduced tracking variable
 1469 that is very effective in removing highly-ionizing backgrounds caused by over-
 1470 lapping tracks. A few additional requirements are placed on the tracks consid-
 1471 ered for [LLP](#) candidates that increase background rejection by targeting specific
 1472 types of [SM](#) particles. These techniques provide a significant analysis improve-
 1473 ment over previous iterations of ionization-based searches on ATLAS by provid-
 1474 ing additional background rejection with minimal loss in signal efficiency.

1475 The ionization measurement with the Pixel detector can be calibrated to pro-
 1476 vide an estimator of $\beta\gamma$. That estimate, together with the momentum measure-
 1477 ment provided by tracking, can be used to reconstruct a mass for each track
 1478 which traverses the pixel detector. That mass variable will be peaked at the [LLP](#)
 1479 mass for any signal, and provides an additional tool to search for an excess. In
 1480 addition to an explicit requirement on ionization, this search constructs a mass-
 1481 window for each targeted signal mass in order to evaluate any excess of events
 1482 and to set limits.

1483 The strategy discussed here is optimized for lifetimes of $O(1) - O(10)$ ns.
 1484 Pixel ionization is especially useful in this regime as particles only need to prop-
 1485 agate through the first seven layers of the inner detector, about 37 cm from the
 1486 beam axis. The search is still competitive with other searches for [LLPs](#) at longer
 1487 lifetimes, because the primary discriminating variables are still applicable even
 1488 for particles that do not decay within the detector [62]. Although the majority of

1489 the requirements will be the same for all lifetimes, two signal regions are defined
 1490 to optimize separately for intermediate and long lifetime particles.

1491 11.1 TRIGGER

1492 Triggering remains a significant difficulty in defining an event selection with
 1493 high signal efficiency in a search for LLPs. There are no triggers available in
 1494 the current ATLAS system that can fire directly from a high momentum track
 1495 with large ionization (Section 6.6). Although in some configurations a charged
 1496 LLP can fire muon triggers, this requirement introduces significant model depen-
 1497 dence on both the allowed lifetimes and the interactions in the calorimeter [54],
 1498 as discussed in Section 10.1.1.

1499 For a search targeting particles which may decay prior to reaching the muon
 1500 system, the most efficient available trigger is based on missing energy [54]. As
 1501 discussed in Section 10.1, signal events can produce significant E_T^{miss} by a few
 1502 mechanisms. At the trigger level however, the missing energy is only calculated
 1503 using the calorimeters (Section 6.6) where the R-Hadrons deposit little energy.
 1504 So, at short lifetimes, E_T^{miss} measured in the calorimeter is generated by an im-
 1505 balance between the jets and undetected LSPs produced in R-Hadron decays. At
 1506 longer lifetimes, without the decay products, missing energy is only produced in
 1507 the calorimeters when the R-Hadrons recoil against an initial state radiation (ISR)
 1508 jet.

1509 These features are highlighted in Figure 34, which shows the E_T^{miss} distribu-
 1510 tions for simulated short lifetime (3 ns) and stable R-Hadron events. The figure
 1511 includes both the offline E_T^{miss} , the missing energy calculated with all available
 1512 information, and Calorimeter E_T^{miss} , the missing energy calculated using only
 1513 information available at the calorimeter which approximates the missing energy
 1514 available at the trigger. The short lifetime sample has significantly greater E_T^{miss}
 1515 and Calorimeter E_T^{miss} than the stable sample as expected. For the stable sam-
 1516 ple, a small fraction of events with very large E_T^{miss} (about 5%) migrate into the
 1517 bin with very small Calorimeter E_T^{miss} because the E_T^{miss} produced by a charged
 1518 R-Hadron track opposite a neutral R-Hadron track does not contribute any miss-
 1519 ing energy in the calorimeters.

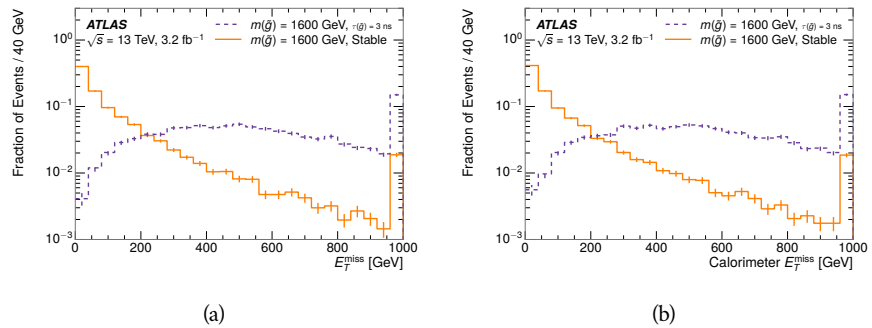


Figure 34: The distribution of (a) E_T^{miss} and (b) Calorimeter E_T^{miss} for simulated signal events before the trigger requirement.

1520 So, either case to some extent relies on kinematic degrees of freedom to pro-
 1521 duce missing energy, as the pair-produced LLPs tend to balance each other in
 1522 the transverse plain. That balance results in a relatively low efficiency for long-
 1523 lifetime particles, roughly 40%, and efficiencies between 65% and 95% for shorter
 1524 lifetimes depending on both the mass and the lifetime. For long lifetimes in par-
 1525 ticular, the presence of ISR is important in providing an imbalance in the trans-
 1526 verse plane, and is an important aspect of modeling the selection efficiency for
 1527 R-Hadron events.

1528 The missing energy trigger with the lowest threshold available is chosen for
 1529 this selection in order to maximize the trigger efficiency. During 2015 data col-
 1530 lection this was the HLT_xe70 trigger, which used a 50 GeV threshold on miss-
 1531 ing energy at LVL1 and a 70 GeV threshold on missing energy at the HLT. These
 1532 formation of the trigger decision for missing energy was discussed in more detail
 1533 in Section 6.6.

1534 11.2 KINEMATICS AND ISOLATION

1535 After the trigger requirement, each event is required to have a primary vertex
 1536 reconstructed from at least two well-measured tracks in the inner detector, each
 1537 with $p_T > 400$ MeV. If more than one such vertex exists, the primary vertex
 1538 is taken to be the one with the largest summed track momentum for all tracks
 1539 associated to that vertex. The offline reconstructed E_T^{miss} is required to be above
 1540 130 GeV to additionally reject SM backgrounds. The transverse missing energy
 1541 is calculated using fully reconstructed and calibrated offline objects, as described
 1542 in Section 7.5. In particular the E_T^{miss} definition in this selection uses jets recon-
 1543 structed with the anti- k_t algorithm with radius $R = 0.4$ from clusters of energy
 1544 in the calorimeter (Section 7.2) and with $p_T > 20$ GeV, as well as reconstructed
 1545 muons, electrons, and tracks not identified as another object type.

1546 The E_T^{miss} distributions are shown for data and a few simulated signals in Fig-
 1547 ure 35, after the trigger requirement. The cut placed at 130 GeV is 95% effi-
 1548 cient for metastable and 90% efficient for stable particles, after the trigger re-
 1549 quirement, because of the missing energy generating mechanisms discussed pre-
 1550 viously. The distribution of data in this figure and subsequent figures in this sec-
 1551 tion can be interpreted as the distribution of backgrounds, as any signal contam-
 1552 ination would be negligible if present at these early stages of the selection (prior
 1553 to the final requirement on ionization). The background falls rapidly with miss-
 1554 ing energy, motivating the direct requirement on E_T^{miss} for the signal region. Al-
 1555 though a tighter requirement than the specified value of 130 GeV would seem to
 1556 increase the search potential from these early distributions, other requirements
 1557 are more optimal when taken as a whole. The specific values for each require-
 1558 ment in signal region were optimized considering the increase in discovery reach
 1559 for tightening the requirement on each discriminating variable. **NOTE: If space**
 1560 **and time permit, I will add a whole section about signal region optimiza-**
 1561 **tion..**

1562 It is typically the practice for searches for new physics on ATLAS to place an
 1563 offline requirement on the triggering variable that is sufficiently tight to guar-

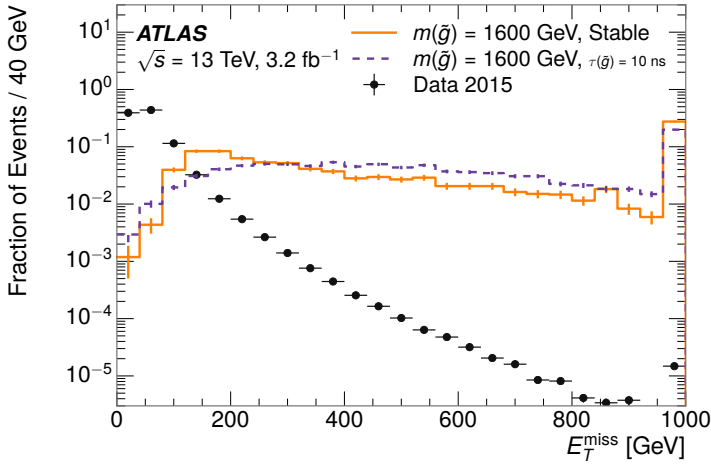


Figure 35: The distribution of E_T^{miss} for data and simulated signal events, after the trigger requirement.

1564 antee that the event would pass the trigger. Such a tight requirement makes the
 1565 uncertainty on the trigger efficiency of the simulation negligible, as modeling the
 1566 regime where the trigger is only partially efficient can be difficult. In this analy-
 1567 sis, however, because of the atypical interactions of R-Hadrons with the tracker
 1568 and the calorimeter, the offline requirement on E_T^{miss} is not sufficient to guar-
 1569 antee a 100% trigger efficiency even at large values, as can be seen in Figure 36.
 1570 This figure shows the efficiency for passing the HLT_xe70 trigger as a function
 1571 of the requirement on E_T^{miss} , which plateaus to roughly 85% even at large values.
 1572 This plateau does not reach 100% because events which have large offline miss-
 1573 ing energy from a neutral R-Hadron produced opposite of a charged R-Hadron
 1574 can have low missing energy in the calorimeters. The Calorimeter E_T^{miss} , on the
 1575 other hand, does not have this effect and reaches 100% efficiency at large values
 1576 because it is the quantity that directly corresponds to the trigger threshold. In
 1577 both cases the efficiency of triggering is greater for the short lifetime sample be-
 1578 cause the late decays to hadrons and LSPs produce an imbalance in the calorime-
 1579 ters even though they may not be reconstructed offline as tracks or jets. For this
 1580 reason, the requirement on E_T^{miss} is determined by optimizing the background
 1581 rejection even though it corresponds to a value of trigger efficiency significantly
 1582 below 1.0.

1583 Potential signal events are then required to have at least one candidate LLP
 1584 track. Although the LLPs are produced in pairs, many models do not consistently
 1585 yield two charged particles. For example, in the R-Hadron model highlighted
 1586 here, only 20% of events have two charged R-Hadrons while 47% of events have
 1587 just one. A signal region requiring two charged candidates could be a powerful
 1588 improvement in background rejection for a larger dataset, but it is not consid-
 1589 ered in this version of the analysis as it was found to be unnecessary to reject the
 1590 majority of backgrounds.

1591 For a track to be selected as a candidate, it must have $p_T > 50 \text{ GeV}$ and pass
 1592 basic quality requirements. The track must be associated to the primary vertex.

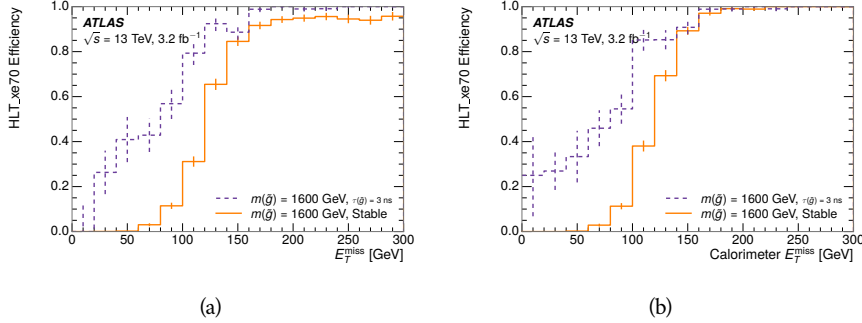


Figure 36: The trigger efficiency for the HLT_xe70 trigger requirement as a function of (a) E_T^{miss} and (b) Calorimeter E_T^{miss} for simulated signal events.

It must also have at least seven clusters in the silicon layers in the inner detector to ensure an accurate measurement of momentum. Those clusters must include one in the innermost layer if the extrapolated track is expected to pass through that layer. And to ensure a reliable measurement of ionization, the track is required to have at least two clusters in the pixel detector that provide a measurement of dE/dx .

At this point in the selection, there is a significant high-ionization background from multiple tracks that significantly overlap in the inner detector. Previous version of this analysis have rejected these overlaps by an explicit overlap rejection between pairs of fully reconstructed tracks, typically by requiring no additional tracks within a cone around the candidate. This technique, however, fails to remove the background from tracks that overlap so precisely that the tracks cannot be separately resolved, which can be produced in very collimated photon conversions or decays of pions.

A new method, added in Run 2, identifies cluster shapes that are likely formed by multiple particles based on a neural network classification algorithm. The number of clusters that are classified this way in the pixel detector for a given track is called N_{split} . As the shape of clusters requires significantly less spatial separation to identify overlaps than it does to reconstruct two fully resolved tracks, this variable is more effective at rejecting backgrounds from overlaps. Figure 37 shows the dependence of ionization on N_{split} ; as N_{split} increases the most probable value of dE/dx grows significantly up to twice the expected value when $N_{\text{split}} = 4$.

This requirement is very successful in reducing the long positive tail of the dE/dx distributions, as can be seen in Figure 38. Comparing the distribution for “baseline tracks”, tracks with only the above requirements on clusters applied and before the requirement on N_{split} , to the distribution with $N_{\text{split}} = 0$, it is clear that the fraction of tracks with large dE/dx is reduced by several orders of magnitude. The tracks without split hits are very close to the dE/dx distribution of identified muons, which are extremely well isolated on average. Figure 38 also includes the distribution of dE/dx in an example signal simulation to demonstrate how effective dE/dx is as a discriminating variable with this isolation applied. The background falls rapidly for $dE/dx > 1.8 \text{ MeVg}^{-1}\text{cm}^2$

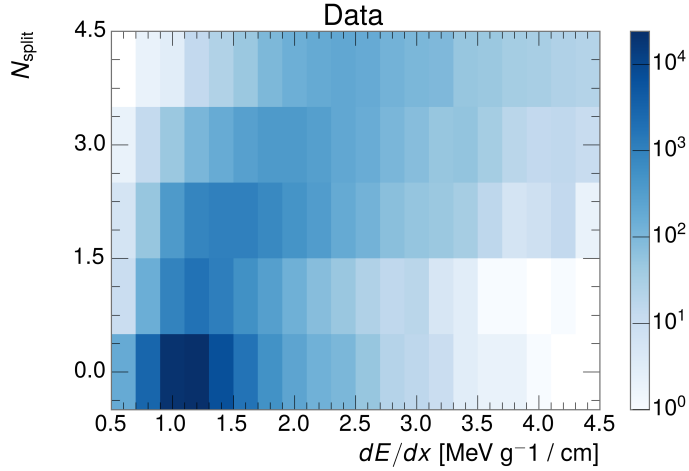


Figure 37: The dependence of dE/dx on N_{split} in data after basic track hit requirements have been applied.

1626 while the majority of the signal, approximately 90% depending on the mass, falls
 1627 above that threshold. Over 90% of [LLP](#) tracks in simulated signal events pass the
 1628 N_{split} -based isolation requirement.

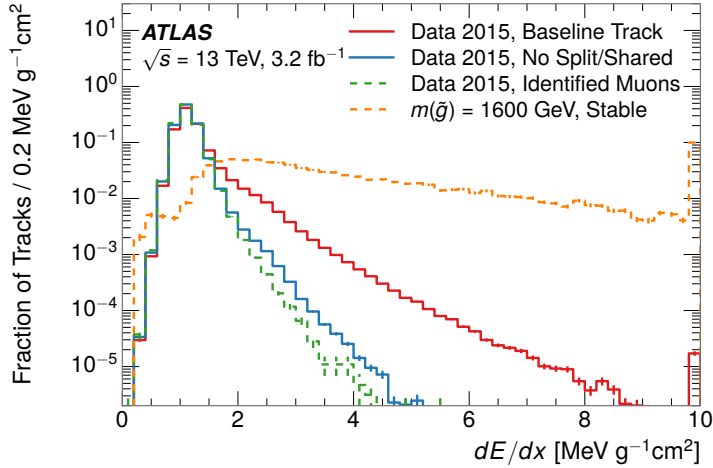


Figure 38: The distribution of dE/dx with various selections applied in data and simulated signal events.

1629 A few additional kinematic requirements are imposed to help reduce [SM](#) back-
 1630 grounds. The momentum of the candidate track must be at least 150 GeV, and
 1631 the uncertainty on that measurement must be less than 50%. The distribution of
 1632 momentum is shown in Figure 39 for tracks in data and simulated signal events
 1633 after the previously discussed requirements on clusters, transverse momentum,
 1634 and isolation have been imposed. The signal particles are much harder on aver-

age than their backgrounds because of the high energy interactions required to produce them. The transverse mass, M_T , defined as

$$M_T = \sqrt{2p_T E_T^{\text{miss}}(1 - \cos(\Delta\phi(E_T^{\text{miss}}, \text{track})))} \quad (1)$$

estimates the mass of a decay of to a single charged particle and an undetected particle and is required to be greater than 130 GeV to reject contributions from the decay of W bosons. Figure 40 shows the distribution of M_T for data and simulated signal events. The signal is distributed over a wide range of M_T , with about 90% above the threshold value of 130 GeV. The data shows a dual-peaked structure, where the first peak comes from W boson decays and the second peak is a kinematic shaping from the requirements on E_T^{miss} and the track p_T in dijet events.

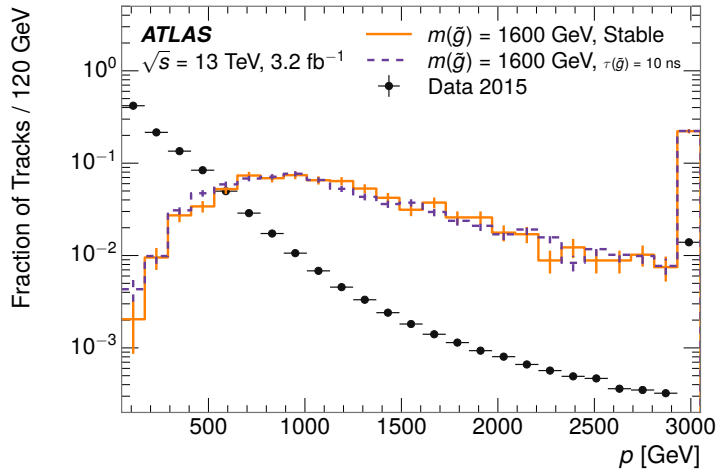


Figure 39: The distribution of track momentum for data and simulated signal events, after previous selection requirements have been applied.

11.3 PARTICLE SPECIES REJECTION

The amount of ionization deposited by particles with low mass and high momentum has a large positive tail [55], so backgrounds can be formed by a wide variety of SM processes when various charged particles have a few randomly large deposits of energy in the pixel detector. Those backgrounds can be additionally reduced by targeting other interactions with the detector where they are expected to have different behavior than R-Hadrons. The interactions with the detector depend on the types of particles produced rather than the processes which produce them, so this search forms a series of rejections to remove backgrounds from individual particle species. These rejections focus on using additional features of the event, other than the kinematics of the candidate track, as they can provide a powerful source of background rejection with very high signal efficiency. However, the lifetime of an R-Hadron can significantly change its

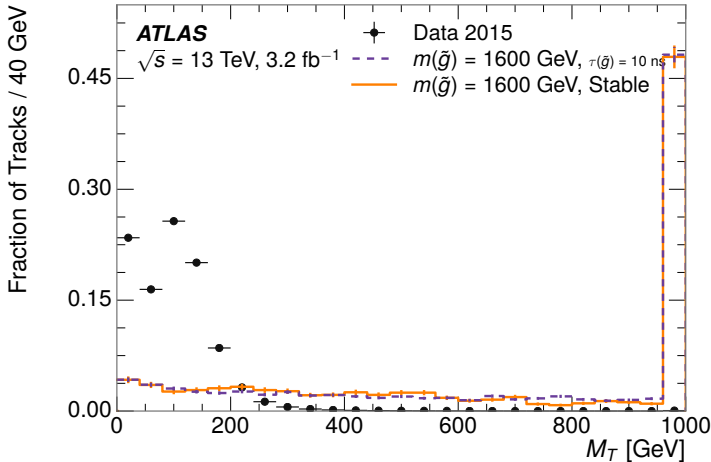


Figure 40: The distribution of M_T for data and simulated signal events, after previous selection requirements have been applied.

1658 detector characteristics, as discussed in Section 10.1.2. To accommodate these
 1659 differences, the SM rejections defined in this section are split to form two signal
 1660 regions, one for long-lifetimes particles, the stable region ($50 \leq \tau[\text{ns}] < \infty \text{ ns}$),
 1661 and one for intermediate lifetime particles, the metastable region ($0.4 < \tau[\text{ns}] <$
 1662 50).

1663 Jets can be very effectively rejected by considering the larger-scale isolation of
 1664 the candidate track. In this case the isolation focuses on the production of nearby
 1665 particles as a jet-veto, rather than the isolation from overlapping tracks based on
 1666 N_{split} that was used to reduce high-ionization backgrounds. As explained in Sec-
 1667 tion 10.1, the fragmentation process which produces an R-Hadron is very hard
 1668 and thus is not expected to produce additional particles with a summed momen-
 1669 tum of more than 5 GeV. The jet-veto uses the summed momentum of tracks
 1670 with a cone of $\Delta R < 0.25$, referred to as p_T^{Cone} , which is shown in Figure 41 for
 1671 data and simulated signal events. In the data this value has a peak at zero from
 1672 isolated tracks such as leptons, and a long tail from jets which contains as much
 1673 as 80% of the background above 20 GeV at this stage of the selection. In signal
 1674 events p_T^{Cone} is strongly peaked at zero and significantly less than 1% of signal
 1675 events have p_T^{Cone} above 20 GeV. This makes a requirement of $p_T^{\text{Cone}} < 20 \text{ GeV}$
 1676 a very effective method to reject background without losing signal efficiency.
 1677 For the stable signal region, this cut is further tightened to $p_T^{\text{Cone}} < 5 \text{ GeV}$ as
 1678 it is the most effective variable remaining to extend the search reach for long
 1679 lifetimes.

1680 Even for fully isolated particles, there are additional methods to reject each
 1681 type of particle using information in the muon system and calorimeters. Muons
 1682 can be identified very reliably using the tracks in the muon system, as described
 1683 in Section 7.4. For intermediate lifetimes the LLPs do not survive long enough
 1684 to reach the muon system, and so muons are vetoed by rejecting tracks that as-
 1685 sociate to a muon with medium muon identification requirements (Section 7.4).
 1686 For longer lifetimes, this rejection is not applied because LLPs which reach the

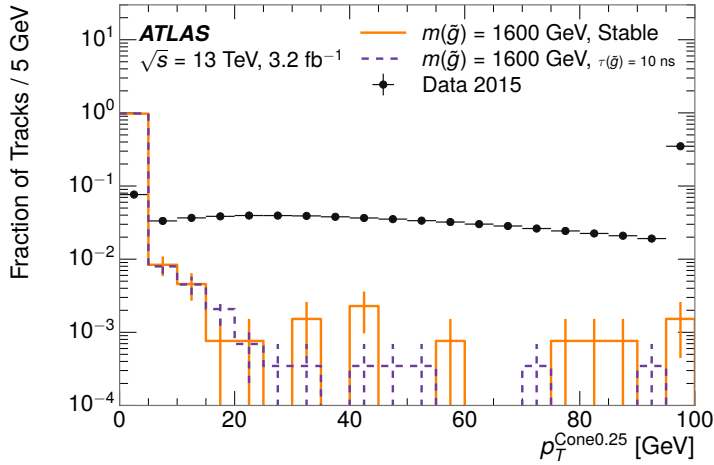


Figure 41: The distribution of summed tracked momentum within a cone of $\Delta R < 0.25$ around the candidate track for data and simulated signal events, after previous selection requirements have been applied.

muon system can be identified as muons as often as 30% of the time in simulated samples.

Calorimeter-based particle rejection relies on the expected small deposits of energy from LLPs. When the lifetime is long enough to reach the calorimeter, a LLP deposits little of its energy as it traverses the material, as discussed in Section 10.1. Even when the particle does decay before the calorimeter, the majority of its energy is carried away by the LSP and not deposited in the calorimeter. In both cases the energy is expected to be distributed across the layers of the calorimeters and not peaked in just one layer. This can be quantified in terms of E/p , the ratio of calorimeter energy of a nearby jet to the track momentum, and f_{EM} , the fraction of energy in that jet within the electromagnetic calorimeter. When no jets fall within a cone of 0.05 of the particle, E/p and f_{EM} are both defined as zero. E/p is expected to be above 1.0 for typical SM particles because of calibration and the contributions from other nearby particles, as discussed in Chapter ???. At these momenta there is no significant zero fraction due to interactions with the detector or insufficient energy deposits (see Section 8.2.2). f_{EM} is peaked close to 1.0 for electrons, and distributed between 10% and 90% for hadrons.

These trends can be seen in the two dimensional distribution for signal in Figure 42 for stable and metastable (10 ns) events. The majority of R-Hadrons in both samples fall into the bin for $E/p = 0$ and $f_{\text{EM}} = 0$ because the majority of the time there is no associated jet. In the stable sample, when there often is an associated jet, E/p is typically still below 0.1, and the f_{EM} is predominantly under 0.8. In the metastable sample, on the other hand, E/p is larger but still typically below 0.1 because of actual jets produced during the decay. The f_{EM} is much lower on average in this case, below 0.1, because the 10 ns lifetime particles rarely decay before passing through the electromagnetic calorimeter. Figure 42 also includes simulated Z decays to electrons or tau leptons. From the decays

1715 to electrons it is clear that the majority of electrons have f_{EM} above 0.9. The
 1716 tau decays include a variety of products. Muons can be seen in the bin where
 1717 $E/p = 0$ and $f_{\text{EM}} = 0$ because they do not have an associated jet. Electrons fall
 1718 into the range where $E/p > 1$ and $f_{\text{EM}} > 0.9$. Hadronic tau decays are the most
 1719 common, and fall in the range of $0.1 < f_{\text{EM}} < 0.9$ and $E/p > 1.0$.

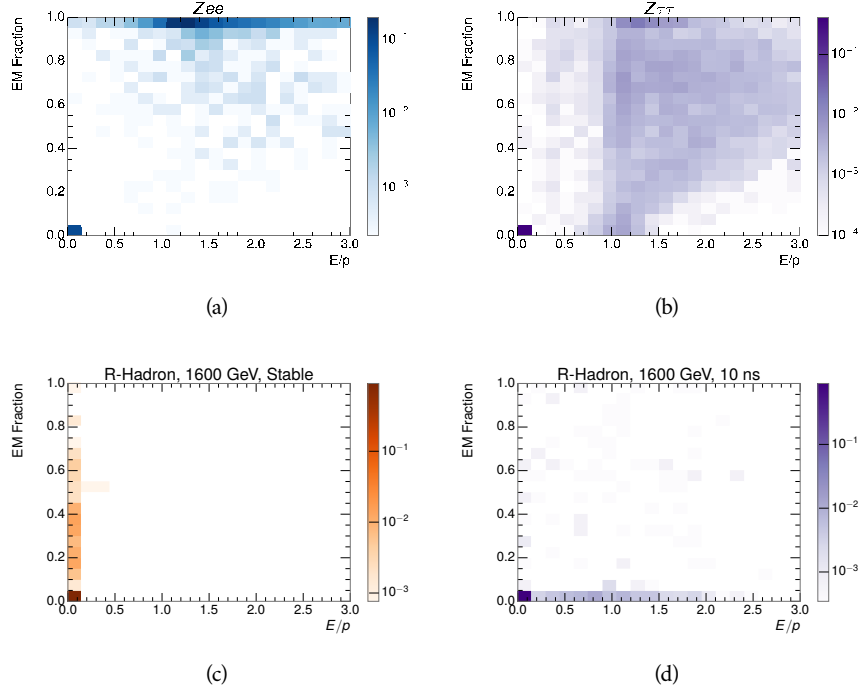


Figure 42: The normalized, two-dimensional distribution of E/p and f_{EM} for simulated
 (a) $Z \rightarrow ee$, (b) $Z \rightarrow \tau\tau$, (c) 1200 GeV Stable R-Hadron events, and (d) 1200
 GeV, 10 ns R-Hadron events.

1720 These differences motivate an electron rejection by requiring an f_{EM} below
 1721 0.9. Similarly, isolated hadrons are rejected by requiring $E/p < 1.0$. These re-
 1722 quirements combine to remove the majority of isolated electrons and hadrons
 1723 but retain over 95% of the simulated signal across a range of masses and lifetimes.

1724 11.4 IONIZATION

1725 The final requirement on the candidate track is the primary discriminating vari-
 1726 able, the ionization in the pixel detector. That ionization is measured in terms
 1727 of dE/dx , which was shown for data and simulated signal events in Figure 38.
 1728 dE/dx is dramatically greater for the high mass signal particles than the back-
 1729 grounds, which start to fall immediately after the minimally ionizing peak at 1.1
 1730 $\text{MeV g}^{-1} \text{cm}^2$. The dE/dx for candidate tracks must be greater than a pseudorapidity-
 1731 dependent threshold, specifically $1.80 - 0.11|\eta| + 0.17\eta^2 - 0.05\eta^3 \text{ MeV g}^{-1} \text{ cm}^{-2}$,
 1732 in order to correct for an approximately 5% dependence of the MIP peak on η .
 1733 The requirement was chosen as part of the signal region optimization, and man-

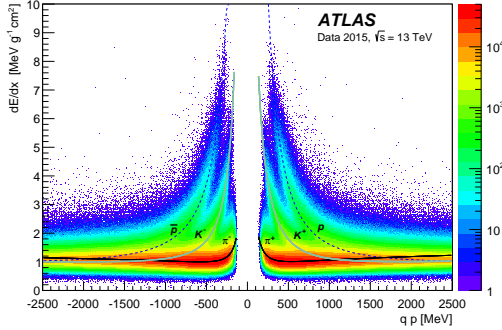


Figure 43: Two-dimensional distribution of dE/dx versus charge signed momentum (qp) for minimum-bias tracks. The fitted distributions of the most probable values for pions, kaons and protons are superimposed.

ages to reduce the backgrounds by a factor of 100 while remaining 70-90% efficient for simulated signal events depending on the mass.

11.4.1 MASS ESTIMATION

The mean value of ionization in silicon is governed by the Bethe equation and the most probable value follows a Landau-Vavilov distribution [55]. Those forms inspire a parametric description of dE/dx in terms of $\beta\gamma$,

$$(dE/dx)_{MPV}(\beta\gamma) = \frac{p_1}{\beta^{p_3}} \ln(1 + [p_2 \beta\gamma]^{p_5}) - p_4 \quad (2)$$

which performs well in the range $0.3 < \beta\gamma < 1.5$. This range includes the expected range of $\beta\gamma$ for the particles targeted for this search, with $\beta\gamma \approx 2.0$ for lower mass particles ($O(100 \text{ GeV})$) and up to $\beta\gamma \approx 0.5$ for higher mass particles ($O(1000 \text{ GeV})$). The parameters, p_i , are fit using a 2015 data sample of low-momentum pions, kaons, and protons as described in Ref. [76]. Figure 43 shows the two-dimensional distribution of dE/dx and momentum along with the above fitted values for $(dE/dx)_{MPV}$.

The above equation (2) is then numerically inverted to estimate $\beta\gamma$ and the mass for each candidate track. In simulated signal events, the mean of this mass value reproduces the generated mass up to around 1800 GeV to within 3%, and 3% shift is applied to correct for this difference. The mass distributions prior to this correction are shown for a few stable mass points in Figure 44. The large widths of these distributions come from the high variability in energy deposits in the pixel detector as well as the uncertainty on momentum measurements at high momentum, but the means converge to the expected values.

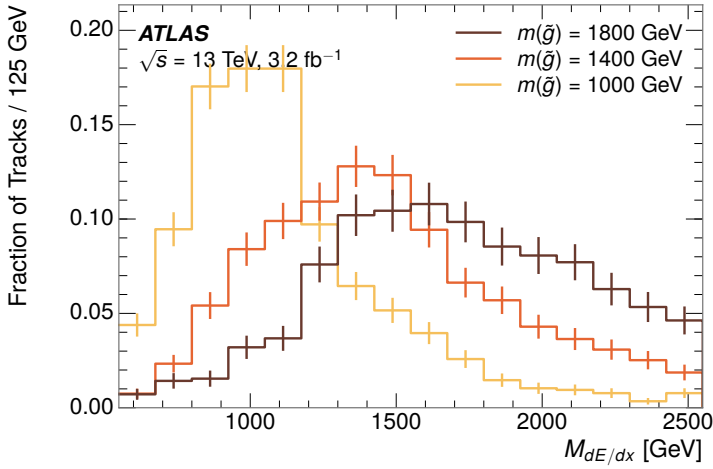


Figure 44: The distribution of mass estimated using dE/dx for simulated stable R-Hadrons with masses between 1000 and 1600 GeV.

1755 This analysis evaluates expected yields and the resulting cross sectional limits
 1756 using windows in this mass variable. The windows are formed by fitting mass
 1757 distributions in simulated signal events like those in Figure 44 to Gaussian distri-
 1758 butions and taking all events that fall within $\pm 1.4\sigma$ of the mean. As can be seen
 1759 in Figure 44, typical values for this width are $\sigma \approx 300 - 500$ GeV depending on
 1760 the generated mass.

1761 11.5 EFFICIENCY

1762 The numbers of events passing each requirement through ionization are shown
 1763 in Table 3 for the full 2015 dataset and a simulated 1600 GeV, 10 ns lifetime R-
 1764 Hadron sample. The table highlights the overall acceptance \times efficiency for sig-
 1765 nal events, which for this example is 19%. Between SM rejection and ionization,
 1766 this signal region reduces the background of tracks which pass the kinematic
 1767 requirements down by an additional factor of almost 2000.

1768 There is a strong dependence of this efficiency on lifetime and mass, with effi-
 1769 ciencies dropping to under 1% at low lifetimes. Figure 45 shows the dependence
 1770 on both mass and lifetime for all signal samples considered in this search. The
 1771 dependence on mass is relatively slight and comes predominantly from the in-
 1772 creasing fraction of R-Hadrons which pass the ionization cut with increasing
 1773 mass. The trigger and E_T^{miss} requirements are most efficient for particles that
 1774 decay before reaching the calorimeters. However, the chance of a particle to be
 1775 reconstructed as a high-quality track decreases significantly at low lifetimes as
 1776 the particle does not propagate sufficiently through the inner detector. These
 1777 effects lead to a maximum in the selection efficiency for lifetimes around 10-30
 1778 ns.

1779 The inefficiency of this signal region at short lifetimes comes almost exclu-
 1780 sively from an acceptance effect, in that the particles do not reach the necessary

Selection	Exp. Signal Events	Observed Events in 3.2 fb^{-1}
Generated	26.0 ± 0.3	
E_T^{miss} Trigger	24.8 ± 0.3 (95%)	
$E_T^{\text{miss}} > 130 \text{ GeV}$	23.9 ± 0.3 (92%)	
Track Quality and $p_T > 50$	10.7 ± 0.2 (41%)	368324
Isolation Requirement	9.0 ± 0.2 (35%)	108079
Track $p > 150 \text{ GeV}$	6.6 ± 0.2 (25%)	47463
$M_T > 130 \text{ GeV}$	5.8 ± 0.2 (22%)	18746
Electron and Hadron Veto	5.5 ± 0.2 (21%)	3612
Muon Veto	5.5 ± 0.2 (21%)	1668
Ionization Requirement	5.0 ± 0.1 (19%)	11

Table 3: The expected number of events at each level of the selection for metastable $1600 \text{ GeV}, 10 \text{ ns}$ R-Hadrons, along with the number of events observed in data, for 3.2 fb^{-1} . The simulated yields are shown with statistical uncertainties only. The total efficiency \times acceptance is also shown for the signal.

1781 layers of the SCT. This can be seen more clearly by defining a fiducial region
 1782 which includes events with at least one R-Hadron that is produced with non-
 1783 zero charge, $p_T > 50 \text{ GeV}$, $p > 150 \text{ GeV}$, $|\eta| < 2.5$, and a decay distance greater
 1784 than 37 cm in the transverse plane. At short (1 ns) lifetimes, the acceptance into
 1785 this region is as low as 4%. Once this acceptance is accounted for, the selection
 1786 efficiency ranges from 25% at lifetimes of 1 ns up to 45% at lifetimes of 10 ns.

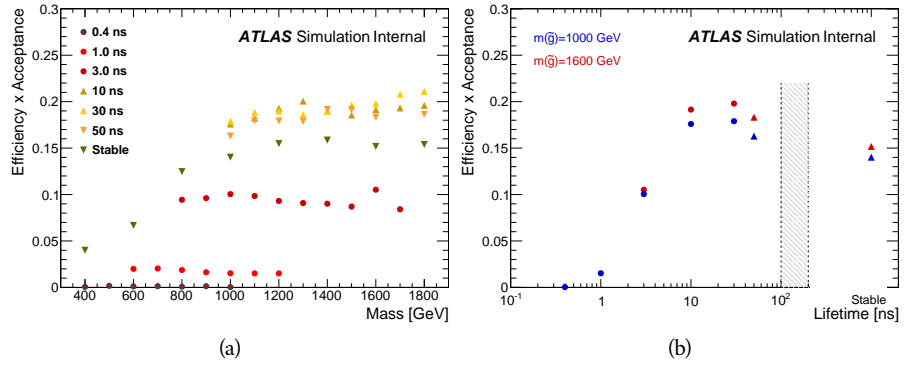


Figure 45: The acceptance \times efficiency as a function of R-Hadron (a) mass and (b) lifetime. (a) shows all of the combinations of mass and lifetime considered in this search, and (b) highlights the lifetime dependence for 1000 GeV and 1600 GeV R-Hadrons.

1787

1788 BACKGROUND ESTIMATION

1789 The event selection discussed in the previous section focuses on detector sig-
 1790 natures, emphasizing a single high-momentum, highly-ionizing track. That track
 1791 is then required to be in some way inconsistent with the expected properties
 1792 of SM particles, with various requirements designed to reject jets, hadrons,
 1793 electrons, and muons (Section 11.3). Therefore the background for this search comes
 1794 entirely from reducible backgrounds that are outliers of various distributions in-
 1795 cluding dE/dx , f_{EM} , and p_T^{Cone} . The simulation can be tuned in various ways to
 1796 do an excellent job of modeling the average properties of each particle type [77],
 1797 but it is not necessarily expected to accurately reproduce outliers. For this rea-
 1798 sons, the background estimation used for this search is estimated entirely using
 1799 data.

1800 12.1 BACKGROUND SOURCES

1801 SM charged particles with lifetimes long enough to form tracks in the inner de-
 1802 tector can be grouped into three major categories based on their detector inter-
 1803 actions: hadrons, electrons, and muons. Every particle that enters into the back-
 1804 ground for this search belongs to one of these types. Relatively pure samples of
 1805 tracks from each of these types can be formed in data by inverting the various
 1806 rejection techniques in Section 11.3. Specifically, muons are selected requiring
 1807 medium muon identification, electrons requiring $E/p > 1.0$ and $f_{EM} > 0.95$,
 1808 and hadrons requiring $E/p > 1.0$ and $f_{EM} < 0.95$.

1809 Figure 46 shows the distributions of momentum and dE/dx for these cate-
 1810 gories in data, after requiring the event level selection as well as the track re-
 1811 quirements on p_T , hits, and N_{split} , as discussed in Section 11.2. Simulated signal
 1812 events are included for reference. These distribution are only illustrative of the
 1813 differences between types, as the rejection requirements could alter their shape.
 1814 This is especially significant for momentum which enters directly into E/p and
 1815 can indirectly affect muon identification. However the various types show clear
 1816 differences in both distributions. The distributions of momentum are not nec-
 1817 essarily expected to match between the various types because the production
 1818 mechanisms for each type result in different kinematic distributions. dE/dx is
 1819 also different between types because of incomplete isolation; although the re-
 1820 quirement on N_{split} helps to reduce the contribution of nearby particles it does
 1821 not completely remove the effect of overlaps. Muons are better isolated because
 1822 they do not have the additional particle from hadronization present for hadrons
 1823 and they are significantly less likely do interact with the detector and produce
 1824 secondary particles compared to hadrons and electrons. Thus muons have the
 1825 smallest fraction of dE/dx above the threshold of $1.8 \text{ MeVg}^{-1}\text{cm}^2$; hadrons and
 1826 electrons have a larger fraction above this threshold.

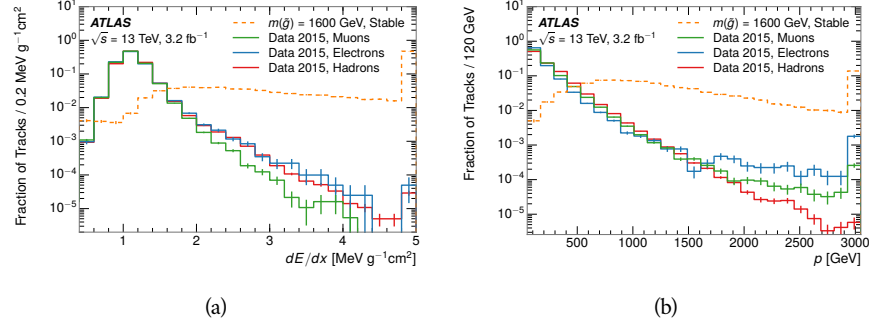


Figure 46: The distribution of (a) dE/dx and (b) momentum for tracks in data and simulated signal after requiring the event level selection and the track selection on p_T , hits, and N_{split} . Each sub-figure shows the normalized distributions for tracks classified as hadrons, electrons, and muons in data and R-Hadrons in the simulated signal.

1827 It is difficult to determine what fraction of each particle type enters into the fi-
 1828 nal signal region. The background method will not have significant dependence
 1829 on the relative contributions of each species, but it is useful to understand the
 1830 differences between each when considering the various tests of the method.

1831 12.2 PREDICTION METHOD

1832 The data-driven background estimation relies on the independence between ion-
 1833 ization and other kinematic variables in the event. For standard model particles
 1834 with momenta above 50 GeV, dE/dx is not correlated with momentum; though
 1835 there is a slight relativistic rise as momentum increases, the effect is small com-
 1836 pared to the width of the distribution of ionization energy deposits.. So, the
 1837 proposed method to estimate the mass distribution of the signal region is to use
 1838 momentum from a track with low dE/dx (below the threshold value) and to com-
 1839 bine it with a random dE/dx value from a dE/dx template. The resulting track is
 1840 just as likely as the original, so a number of such random generations provide the
 1841 expected distributions of momentum and ionization. These are then combined
 1842 using the parametrization described in Section 11.4.1 to form a distribution of
 1843 mass for the signal region.

1844 Algorithmically this method is implemented by forming two distinct Control
 1845 Regions (**CR**s). The first **CR**, CR1, is formed by applying the entire event selec-
 1846 tion from Chapter 11 up to the dE/dx and mass requirements. The dE/dx re-
 1847 quirement is instead inverted for this region. Because of the independence of
 1848 dE/dx , the tracks in this control region have the same kinematic distribution
 1849 as the tracks in the signal region, and are used to measure a two-dimensional
 1850 template of p and η . The second **CR**, CR2, is formed from the event selection
 1851 through the dE/dx requirement, but with an inverted E_T^{miss} requirement. The
 1852 tracks in this control region are expected to have similar dE/dx distributions to
 1853 the signal region before the ionization requirement, and so this region is used to
 1854 measure a two-dimensional template of dE/dx and η .

1855 The contribution of any signal to the control regions is minimized by the in-
 1856 verted selection requirements. Only less than 10% of simulated signal events
 1857 have either dE/dx or E_T^{miss} below the threshold values in the original signal re-
 1858 gion, while the backgrounds are significantly enhanced by inverting those re-
 1859 quirements. The signal contamination is less than 1% in both control regions
 1860 for all of the simulated masses and lifetimes considered in this analysis.

1861 With those measured templates, the shape of the mass estimation is generated
 1862 by first selecting a random (p, η) combination from CR1. This momentum
 1863 value is combined with a dE/dx value taken from the appropriate distribution
 1864 of dE/dx for the selected η from CR2. The use of η in both random samplings
 1865 controls for any correlation between p , dE/dx , and η . Those values are then
 1866 used to calculate a mass in the same way that is done for regular tracks in data,
 1867 see Section 11.4.1. As this procedure includes all dE/dx values, the cut at 1.8
 1868 MeVg $^{-1}$ cm 2 is then enforced to fully model the signal region. The generated
 1869 mass distribution is then normalized by scaling the background estimate to the
 1870 data in the region $M < 160$ GeV, where signals of this type have already been
 1871 excluded [61]. This normalization uses the distributions of mass generated with-
 1872 out the ionization requirement.

1873 The statistical uncertainties on these background distributions are calculated
 1874 by independently fluctuating each bin of the input templates according to their
 1875 Poisson uncertainties. These fluctuations are repeated a large number of times,
 1876 and the uncertainty on the resulting distribution is taken as the root mean square
 1877 (RMS) deviation of the fluctuations from the average. As the procedure uses one
 1878 million random combinations to generate the distributions, The statistical un-
 1879 certainty from the actual random generations is negligible compared to the un-
 1880 certainty from measuring the templates.

1881 12.3 VALIDATION

1882 The validity of the background estimation technique can be evaluated in both
 1883 data and simulation. The underlying assumption that random combinations of
 1884 dE/dx and momentum can predict a mass distribution in an orthogonal region
 1885 can be tested using simulated samples where concerns like multiple particle types
 1886 can be controlled. Using the same technique in another set of signal-depleted
 1887 regions in data then extends this confidence to the more complicated case where
 1888 several particle species are inherently included.

1889 12.3.1 CLOSURE IN SIMULATION

1890 The first test of the procedure is done using a simulated sample of $W \rightarrow \mu\nu$
 1891 decays. These types of events provide the ingredients required to test the back-
 1892 ground estimate, E_T^{miss} and isolated tracks, with high statistics. In this example
 1893 there is no signal, so simulated events in the orthogonal CRs are used to estimate
 1894 the shape of the mass distribution of the simulated events in the signal region. To
 1895 reflect the different topology for W boson decays, the CRs use slightly modified
 1896 definitions. In all CRs, the requirement of $p > 150$ GeV and the SM rejection

1897 requirements are removed. Additionally, for the signal region the requirement
 1898 on E_T^{miss} is relaxed to 30 GeV and the corresponding inverted requirement on
 1899 CR2 is also set at 30 GeV.

1900 With these modified selections, the simulated and randomly generated distri-
 1901 butions of $M_{dE/dx}$ are shown in Figure 47. This figure includes the mass distri-
 1902 butions before and after the requirement on dE/dx , which significantly shapes
 1903 the distributions. In both cases the background estimation technique repro-
 1904 duces the shape of $M_{dE/dx}$ in the signal region. There is a small difference in the pos-
 1905 itive tail of the mass distribution prior to the ionization cut, where the random
 1906 events underestimate the fraction of tracks with mass above 150 GeV by about
 1907 20%. After the ionization requirement, however, this discrepancy is not present
 1908 and the two distributions agree to within statistical uncertainties.

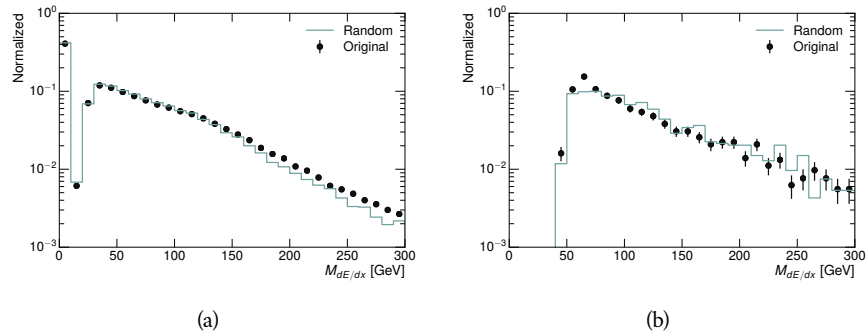


Figure 47: The distribution of $M_{dE/dx}$ (a) before and (b) after the ionization requirement for tracks in simulated W boson decays and for the randomly generated back-
 ground estimate.

1909 This ability to reproduce the shape of the mass distribution in simulated events
 1910 shows that the technique works as expected. No significant biases are acquired
 1911 in using low dE/dx events to select kinematic templates or in using low E_T^{miss}
 1912 events to select ionization templates, as either would result in a mismodeling of
 1913 the shape of the mass distribution. The simulated events contain only one par-
 1914 ticle type, however, so this test only establishes that the technique works well
 1915 when the the CRs are populated by exactly the same species.

1916 12.3.2 VALIDATION REGION IN DATA

1917 The second test of the background estimate is performed using data in an or-
 1918 thogonal validation region. The validation region, and the corresponding CRs,
 1919 are formed using the same selection requirements as in the nominal method but
 1920 with a modified requirement on momentum, $50 < p[\text{GeV}] < 150$. This allows
 1921 the technique to be checked in a region with very similar properties but where
 1922 the signal is depleted, as the majority of the signal has momentum above 150
 1923 GeV while the backgrounds are enhanced below that threshold. Any biases on
 1924 the particle composition of the CRs for the signal region will be reflected in the
 1925 CRs used to estimate the mass distribution in the validation region.

1926 Figure 48 shows the measured and randomly generated mass distributions for
 1927 data before and after the ionization requirement. The background estimate does
 1928 an excellent job of modeling the actual background before the ionization require-
 1929 ment, with good agreement to within the statistical uncertainties out to the limit
 1930 of the mass distribution. There are very few events in the validation region after
 1931 the ionization requirement, but the few observed events are consistent with the
 1932 background prediction. The good agreement in this validation region provides
 1933 a confirmation that the technique works even in the full-complexity case with
 1934 multiple particle types entering the distributions. Any bias from changes in par-
 1935 ticle composition between regions is small compared to statistical uncertainties.

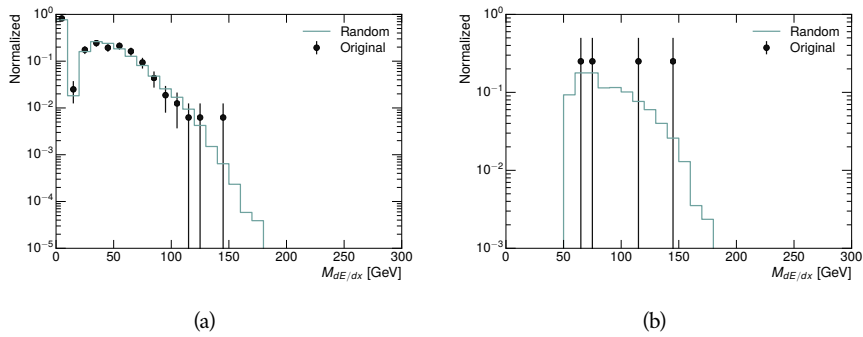


Figure 48: The distribution of $M_{dE/dx}$ (a) before and (b) after the ionization require-
 ment for tracks in the validation region and for the randomly generated back-
 ground estimate.

1936

1937 SYSTEMATIC UNCERTAINTIES AND RESULTS

1938 13.1 SYSTEMATIC UNCERTAINTIES

1939 A number of systematic uncertainties affect the interpretation of the results of
 1940 the search. These uncertainties can broken down into two major categories,
 1941 those which affect the estimate of the background using data and those which
 1942 affect the measurement of the signal yield estimated with simulated events. The
 1943 total measured systematic uncertainties are 7% for the background estimation
 1944 and approximately 32% for the signal yield depending on lifetime. These system-
 1945atic uncertainties are expected to be small compared to the statistical fluctuations
 1946 of the measured yields so that measured cross-sectional limits will be dominated
 1947 by statistical uncertainties. The following sections describe each source of sys-
 1948 tematic uncertainty for each of the two types.

1949 13.1.1 BACKGROUND ESTIMATE

1950 The systematic uncertainties on the background estimate come primarily from
 1951 considering alternative methods for generating the background distributions.
 1952 These uncertainties are small compared to the statistical uncertainties on the
 1953 background estimate which come from the limited statistics in measuring the
 1954 template distributions, as described in Section 12.2. They are summarized in
 1955 Table 4.

Source of Uncertainty:	Value [%]
Analytic Description of dE/dx	4.0
Muon Fraction (Stable Region only)	3.0
IBL Ionization Correction	3.8
Normalization	3.0
Total (Metastable Region):	6.3
Total (Stable Region):	7.0

Table 4: A summary of the sources of systematic uncertainty for the data-driven background in the signal region. If the uncertainty depends on the mass, the maximum values are reported.

1956 13.1.1.1 ANALYTIC DESCRIPTION OF DE/DX

1957 The background estimate uses a binned template distribution to estimate the
 1958 dE/dx of tracks in the signal region, as described in Section 12.2. It is also possi-

ble to fit that measured distribution to a functional form to help smooth the distribution in the tails of dE/dx where the template is driven by a small number of tracks. Both Landau convolved with a Gaussian and Crystal Ball functions are considered as the functional form and used to re-estimate the background distribution. The deviations compared to the nominal method are found to be 4%, and this is taken as a systematic uncertainty to cover the inability carefully predict the contribution from the long tail of dE/dx where there are few measurements available in data.

13.1.1.2 MUON FRACTION

The stable region of the analysis explicitly includes tracks identified as muons, which have a known difference in their dE/dx distributions compared to non-muon tracks (Section 12.1). To account for a difference in muon fraction between the background region and the signal region for this selection, the dE/dx templates for muons and non-muons are measured separately and then the relative fraction of each is varied in the random generation. The muon fraction is varied by its statistical uncertainty and the resulting difference of 3% in background yield is taken as the systematic uncertainty.

13.1.1.3 IBL CORRECTIONS

The Insertible B-Layer (IBL), described in Section 6.3.1, received a significant dose of radiation during the data collection in 2015. The irradiation can cause a drift in the frontend electronics and thus alter the dE/dx measurement which includes the ToT output by the IBL. These effects are corrected for in the nominal analysis by scaling the dE/dx measurements by a constant factor derived for each run to match the average dE/dx value to a reference run where the IBL was known to be stable to this effect. However, this corrective factor does not account for inter-run variations. To account for this potential drift of dE/dx , the correction procedure is repeated by varying the corrections up and down by the maximal run-to-run variation from the full data-taking period, which results in an uncertainty of 3.8%.

13.1.1.4 NORMALIZATION

As described in Section 12.2, the generated distribution of masses is normalized in a shoulder region ($M < 160$ GeV) where signals have been excluded by previous analyses. That normalization factor is varied by its statistical uncertainty and the resulting fluctuation in the mass distribution of 3% is taken as a systematic uncertainty on the background estimate.

13.1.2 SIGNAL YIELD

The systematic uncertainties on the signal yield can be divided into three categories; those on the simulation process, those on the modeling of the detector efficiency or calibration, and those affecting the overall signal yield. They are summarized in Table 4. The largest uncertainty comes from the uncertainty on

1999 the production cross section for gluinos, which is the dominant systematic un-
 2000 certainty in this analysis.

Source of Uncertainty	-[%]	+[%]
ISR Modeling (Metastable Region)	1.5	1.5
ISR Modeling (Stable Region)	14	14
Pile-up Reweighting	1.1	1.1
Trigger Efficiency Reweighting	0.9	0.9
E_T^{miss} Scale	1.1	2.2
Ionization Parametrization	7.1	0
Momentum Parametrization	0.3	0.0
Electron Rejection	0.0	0.0
Hadron Rejection	0.0	0.0
μ Identification	4.3	4.3
Luminosity	5	5
Signal size uncertainty	28	28
Total (Metastable Region)	30	29
Total (Stable Region)	33	32

Table 5: A summary of the sources of systematic uncertainty for the simulated signal yield. The uncertainty depends on the mass and lifetime, and the maximum negative and positive values are reported in the table.

2001 13.1.2.1 ISR MODELING

2002 As discussed in Section 10.2, MadGraph is expected to reproduce the distribution
 2003 of ISR in signal events more accurately than the nominal Pythia samples. The
 2004 analysis reweights the distribution of ISR in the simulated signal events to match
 2005 the distribution found in generated MadGraph samples. This has an effect on the
 2006 selection efficiency in the signal samples, where ISR contributes to the generation
 2007 of E_T^{miss} . To account for the potential inaccuracy on the simulation of ISR at high
 2008 energies, half of the difference between the signal efficiency with the reweighted
 2009 distribution and the original distribution is taken as a systematic uncertainty.

2010 13.1.2.2 PILEUP REWEIGHTING

2011 The simulated events were generated prior to data collection with an estimate of
 2012 the average number of interactions per bunch crossing. This estimate does not
 2013 match the value of pileup during actual data collection, but a large fraction of the
 2014 simulated events would be discarded in order to match the distribution in data.
 2015 Therefore the simulated signal events are not reweighted for pileup by default
 2016 in the analysis. The effect of the pileup on signal efficiency is not expected to
 2017 depend on the mass or lifetime of the generated signal events, which allows all

2018 of the generated signal events to be used together to assess the pileup dependence.
 2019 To account for the potential effect of the difference in the number of interactions
 2020 per bunch crossing between data and simulation, the difference in yield between
 2021 the nominal signal events and the reweighted events averaged over all masses
 2022 and lifetimes is taken as a systematic uncertainty on the yield for each mass and
 2023 lifetime (1.1%).

2024 13.1.2.3 TRIGGER EFFICIENCY REWEIGHTING

2025 As described in Section 11.2, the selection for this analysis does not require a suf-
 2026 ficiently large value of E_T^{miss} to be above the plateau of trigger efficiency. There-
 2027 fore, some signal events which would otherwise pass the event selection can be
 2028 excluded because of the trigger requirement. These effects can be difficult to es-
 2029 timate in simulation, and thus are constrained by comparing data and simulated
 2030 events in an alternative W boson region which uses decays to muons to find a rel-
 2031 atively pure sample of events with missing energy. The trigger efficiency for data
 2032 and simulated W events are shown in Figure 49. The comparison between data
 2033 and MC in this region constrains the simulation of the trigger efficiency. The
 2034 simulated signal events are reweighted by the ratio of data to simulation in the
 2035 W boson decays, while the difference between the data and simulation in those
 2036 decays is taken as a systematic uncertainty. This results in an uncertainty of only
 2037 0.9% as the majority of events are well above the plateau and the disagreement
 2038 between data and simulation is small even below that plateau.

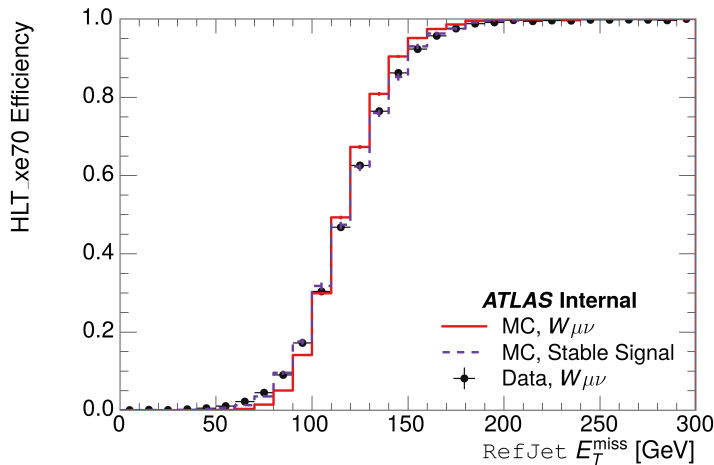


Figure 49: The trigger efficiency for the HLT_xe70 trigger requirement as a function of Calorimeter E_T^{miss} for simulated data events with a W boson selection. Simulated signal events and simulated W boson events are also included.

2039 13.1.2.4 MISSING TRANSVERSE MOMENTUM SCALE

2040 The ATLAS Combined Performance (CP) group provides a default recommenda-
 2041 tion for systematic variations of jets and missing energy (**note: I'm not quite**
 2042 **sure what to cite for this - I don't see any papers from the jet/met group**

Systematic Variation	-[%]	+[%]
JET_GroupedNP_1	-0.7	1.3
JET_GroupedNP_2	-0.7	1.2
JET_GroupedNP_3	-0.5	1.3

Table 6: Example of the contributing systematic variations to the total systematic for the E_T^{miss} Scale, as measured in a 1200 GeV, Stable R-Hadron signal sample.

2043 **after this was implemented).** These variations enter into this analysis only in
 2044 the requirement on E_T^{miss} . The effect of the measured scale of E_T^{miss} is evaluated
 2045 by varying the E_T^{miss} scale according to the one sigma variations provided by all
 2046 **CP** recommendations on objects affecting event kinematics in simulated signal
 2047 events. Missing energy is reconstructed from fully reconstructed objects so any
 2048 systematic uncertainties affecting jets, muons, electrons, or the E_T^{miss} soft terms
 2049 are included. The only non-negligible contributions found using this method are
 2050 itemized in Table 6 for an example signal sample (1200 GeV, Stable R-Hadron),
 2051 where the systematic is measured as the relative difference in the final signal ef-
 2052 ficiency after applying the associated variation through the CP tools. The only
 2053 variations that are significant are the grouped jet systematic variations, which
 2054 combine recommended jet systematic uncertainties into linearly independent
 2055 variations.

2056 As the peak of the reconstructed E_T^{miss} distribution in the signal is significantly
 2057 above the current threshold for events which pass the trigger requirement, the
 2058 effect of scale variation is expected to be small, which is consistent with the mea-
 2059 sured systematic of approximately 2%. Events which do not pass the trigger re-
 2060 quirement usually fail because there are no ISR jets in the event to balance the
 2061 R -hadrons' transverse momentum, so the reconstructed E_T^{miss} is low and there-
 2062 fore also expected to be not very sensitive to scale changes.

2063 13.1.2.5 MOMENTUM PARAMETRIZATION

2064 The uncertainty on the signal efficiency from track momentum is calculated us-
 2065 ing the **CP** group recommendations for tracks. In particular, only one recom-
 2066 mended systematic variation affects track momentum, the sagitta bias for q/P .
 2067 This uncertainty is propagated to the final selection efficiency by varying the
 2068 track momentum by the recommended one sigma variation, and the associated
 2069 uncertainty is found to be negligible (0.3%).

2070 13.1.2.6 IONIZATION REQUIREMENT

2071 The dE/dx distributions in data and simulated events have different most prob-
 2072 able values, which is due in part to radiation effects in the detector that are not
 2073 fully accounted for in the simulation. The difference does not affect the mass
 2074 measurement used in this analysis, as independent calibrations are done in sim-
 2075 ulation and in data. However, it does affect the efficiency of the high dE/dx
 2076 selection requirement. To calculate the size of the effect on the signal efficiency,

2077 the dE/dx distribution in signal simulation is scaled by a scale factor obtained
 2078 from comparing the dE/dx distribution of inclusive tracks in data and in sim-
 2079 ulation. The difference in efficiency for this sample with a scaled dE/dx dis-
 2080 tribution, relative to the nominal case, is taken as a systematic uncertainty on
 2081 signal efficiency. The uncertainty is as large as 7% for low masses and falls to a
 2082 negligible effect for large masses.

2083 13.1.2.7 ELECTRON AND JET REJECTION

2084 The systematic uncertainty on the electron rejection is measured by varying the
 2085 EM fraction requirement significantly, from 0.95 to 0.9. This is found to have
 2086 a less than 0.04% effect on signal acceptance, on average, and so is completely
 2087 negligible. Similarly, the uncertainty on jet rejection is measured by tightening
 2088 the E/p requirement from 0.5 to 0.4. This is found to have no effect on signal
 2089 acceptance, so again the systematic is again negligible.

2090 13.1.2.8 MUON VETO

2091 The metastable signal region requires that the candidate tracks are not identi-
 2092 fied as medium muons because the majority of R-Hadrons in the lifetime range
 2093 included in that region do not reach the muon spectrometers before they de-
 2094 cay. However, the exponential tail of the R-Hadron lifetime distribution results
 2095 in some R-Hadrons traversing the muon spectrometer. These can still fail the
 2096 muon medium identification because they can fail on the requirement on the
 2097 number of precision hits required to pass the loose selection because they ar-
 2098 rive late to the muon spectrometer. This can be seen in Figure 50, which shows
 2099 the efficiency of the muon veto as a function of $1/\beta$, for two simulated stable
 2100 R-Hadron samples.

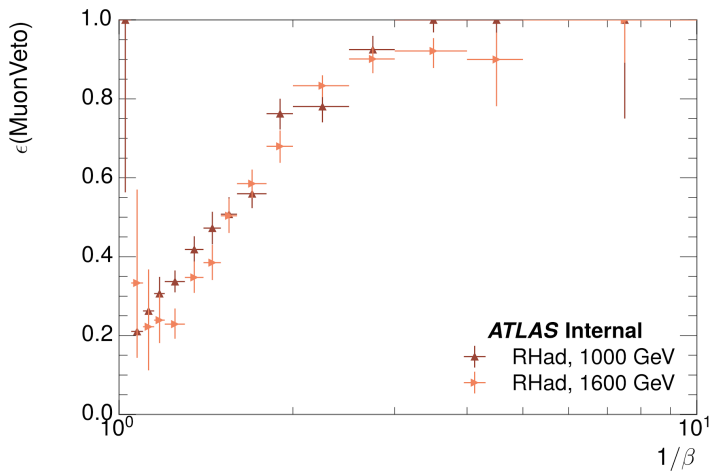
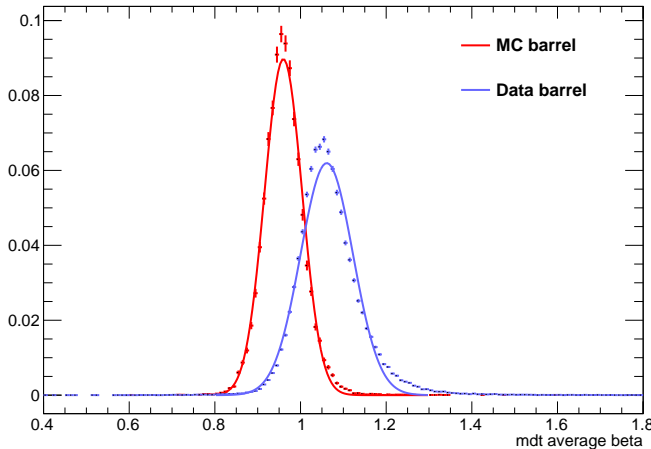


Figure 50: The efficiency of the muon veto for R -hadrons of two different masses, as a function of $\frac{1}{\beta}$ for simulated R-Hadron tracks.

2101 Thus, the efficiency of the muon veto depends on the timing resolution of the
 2102 spectrometer, so an uncertainty is applied to the signal efficiency to cover dif-

2103 differences in timing resolution between data and simulation. First, a sample of
 2104 $Z \rightarrow \mu\mu$ events is selected in data in which one of the muons has a late arrival
 2105 time measured in the Monitored Drift Tube ([MDT](#)). Then the reconstructed β
 2106 distribution is compared to the distribution in simulated $Z \rightarrow \mu\mu$ events; the
 2107 difference between these two distributions reflects the difference in timing res-
 2108 olution between data and simulation. To emulate this difference in simulated
 2109 signal events, the magnitude of the difference is used to scale and shift the true
 2110 β distribution of R-Hadrons in simulation. Signal events are then reweighted
 2111 based on this varied β distribution, and the difference in the efficiency of the
 2112 muon veto selection is compared with the nominal and reweighted true β distri-
 2113 butions. The difference in muon veto efficiency is taken as a systematic uncer-
 2114 tainty of the muon veto.

2115 The comparison of reconstructed β between data and simulation is performed
 2116 separately in the barrel, transition, and endcap regions of the spectrometer, and
 2117 the reweighting of the true β distribution in signal is done per region. The com-
 2118 parison of average reconstructed [MDT](#) β between data and simulation for the
 2119 barrel region is shown in Figure 51 for $Z \rightarrow \mu\mu$ events. As expected, The uncer-
 2120 tainty is found to be negligible for R-hadrons with short lifetimes, and is only
 2121 significant for lifetimes above 30 ns.



2122 Figure 51: The average reconstructed MDT β distribution for $Z \rightarrow \mu\mu$ events in which
 2123 one of the muons is reconstructed as a slow muon, for both data and simula-
 2124 tion. A gaussian fit is superimposed.

2122 13.1.2.9 LUMINOSITY

2123 The luminosity uncertainty is provided by a luminosity measurement on [ATLAS](#)
 2124 and was measured to be 5% at the time of the publication of this analysis.

2125 13.1.2.10 SIGNAL SIZE

2126 As discussed in Section 10.2, the signal cross sections are calculated at [NLO](#) in the
 2127 strong coupling constant with a resummation of soft-gluon emission at [NLL](#). The

Selection Region	Expected Background	Data
Stable	$17.2 \pm 2.6 \pm 1.2$	16
Metastable	$11.1 \pm 1.7 \pm 0.7$	11

Table 7: The estimated number of background events and the number of observed events in data for the specified selection regions prior to the requirement on mass. The background estimates show statistical and systematic uncertainties.

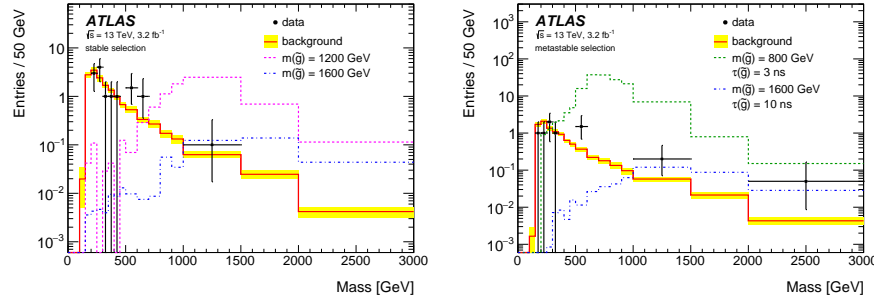


Figure 52: The observed mass distribution of events in data and the generated background distribution in (a) the stable and (b) the metastable signal region. A few example simulated signal distributions are superimposed.

uncertainties on those cross sections are between 14% to 28% for the R-Hadrons in the range of 400 to 1800 GeV [73, 74], where the uncertainty increases with the mass.

13.2 FINAL YIELDS

This full analysis was performed using the 3.2 fb^{-1} from the 2015 data-taking. Using the selections discussed in Chapter 11, sixteen events were observed in the stable signal region and eleven events were observed in the metastable signal region, prior to requirements on the candidate track mass. The background estimate discussed in Chapter 12 predicts $17 \pm 2.6(\text{stat}) \pm 1.2(\text{syst})$ events for the stable region and $11.1 \pm 1.7(\text{stat}) \pm 0.7(\text{syst})$ events for the metastable region. These counts are summarized in Table 7.

The mass estimated using dE/dx (Section 11.4.1) provides the final discriminating variable, where the signal would be expected as an excess in the falling exponential tail of the expected background. The observed distribution of masses is shown in Figure 52, along with the predicted distribution from the background estimate for each signal region. Both include a few example simulated signal distributions, which show the scale of an excess were the R-Hadron signals present. There is no statistically significant evidence of an excess in the data over the background estimation. From this distribution it is clearly possible to rule out signals with lower masses, around 1200 GeV, which have larger cross sections.

2148 13.3 CROSS SECTIONAL LIMITS

2149 Because there is no observed significant excess of events in the signal region, this
 2150 analysis sets upper limits on the allowed cross section for R-Hadron production.
 2151 These limits are set for each mass point by counting the observed events in data,
 2152 along with the expected background and simulated signal events, in windows of
 2153 mass. The mass windows are formed by fitting the distribution of signal events to
 2154 a Gaussian distribution, and the window is then $\pm 1.4\sigma$ around the center of that
 2155 Gaussian. Two examples of the windows formed by this procedure are shown in
 2156 Tables 8-9, for the stable and 10 ns working points. The corresponding counts of
 2157 observed data, expected background, and simulated signal for those same work-
 2158 ing points are shown in Tables 10-11. Appendix B includes the mass windows
 2159 and counts for all of the considered signal points.

$m(\tilde{g})$ [GeV]	Left Extremum [GeV]	Right Extremum [GeV]
1000	655	1349
1100	734	1455
1200	712	1631
1300	792	1737
1400	717	1926
1500	815	2117
1600	824	2122
1700	900	2274
1800	919	2344

Table 8: The left and right extremum of the mass window for each generated mass point with a 10 ns lifetime.

$m(\tilde{g})$ [GeV]	Left Extremum [GeV]	Right Extremum [GeV]
800	627	1053
1000	726	1277
1200	857	1584
1400	924	1937
1600	993	2308
1800	1004	2554

Table 9: The left and right extremum of the mass window used for each generated stable mass point.

2160 The 95% confidence level upper limits on the cross sections for a large grid of
 2161 masses (between 800 and 1800 GeV) and lifetimes (between 0.4 and stable) are
 2162 extracted from these counts with the CL_S method using the profile likelihood

$m(\tilde{g})$ [GeV]	Expected Signal	Expected Background	Observed Data
800	462.83 ± 14.86	1.764 ± 0.080	2.0
1000	108.73 ± 3.38	1.458 ± 0.070	1.0
1200	31.74 ± 0.95	1.137 ± 0.060	1.0
1400	10.22 ± 0.29	1.058 ± 0.058	1.0
1600	3.07 ± 0.09	0.947 ± 0.054	1.0
1800	1.08 ± 0.05	0.940 ± 0.054	1.0

Table 10: The expected number of signal events, the expected number of background events, and the observed number of events in data with their respective statistical errors within the respective mass window for each generated stable mass point

$m(\tilde{g})$ [GeV]	Expected Signal	Expected Background	Observed Data
1000	144.48 ± 5.14	1.499 ± 0.069	2.0
1100	73.19 ± 2.61	1.260 ± 0.060	2.0
1200	41.54 ± 1.41	1.456 ± 0.067	2.0
1300	22.58 ± 0.77	1.201 ± 0.058	2.0
1400	12.70 ± 0.42	1.558 ± 0.071	2.0
1500	6.73 ± 0.24	1.237 ± 0.060	2.0
1600	3.90 ± 0.13	1.201 ± 0.058	2.0
1700	2.27 ± 0.07	1.027 ± 0.052	2.0
1800	1.34 ± 0.04	1.019 ± 0.052	2.0

Table 11: The expected number of signal events, the expected number of background events, and the observed number of events in data with their respective statistical errors within the respective mass window for each generated mass point with a lifetime of 10 ns.

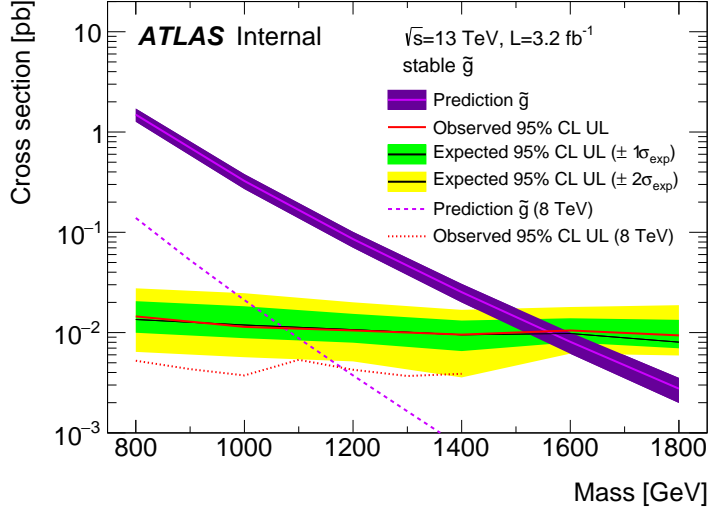


Figure 53: The observed and expected cross section limits as a function of mass for the stable simulated signal. The predicted cross section values for the corresponding signals are included.

ratio as a test statistic [78]. For this procedure, the systematic uncertainties estimated for the signal and background yields are treated as Gaussian-distributed nuisance parameters. The uncertainty on the normalization of the expected background distribution is included in the expected background events. At this point the expected cross section limit is calculated for both the metastable and stable signal region for each lifetime point, and the region with the best expected limit is selected for each lifetime. Using that procedure, the metastable region is used for lifetimes up to and including 30 ns, and the stable region for lifetimes above it.

The resulting cross-sectional upper limits are shown as a function of mass in Figure 53 and Figure 54 for each lifetime considered. The limits are interpolated linearly between each mass point, and the dependence of the limit on the mass is small as the efficiency is relatively constant for large R-Hadron masses. There is however a strong dependence on lifetime, as discussed in Section 11.5, where the probability to form a fully reconstructed track and the kinematic freedom to produce E_T^{miss} result in a local maximum in the limit at 10–30 ns. The figures also include the expected cross section for pair-produced gluino R-Hadrons for reference. For the 10 ns and stable cross section limits, both the observed limit and expected cross section for the Run 1, 8 TeV version of this analysis are included. There the cross sectional limits are lower because of the increased available luminosity, while the signal cross sections were also much lower because of the lower collision energy.

13.4 MASS LIMITS

The cross-sectional limits can then be used to derive a lower mass limit for gluino R-Hadrons by comparing them to the theoretically predicted production cross

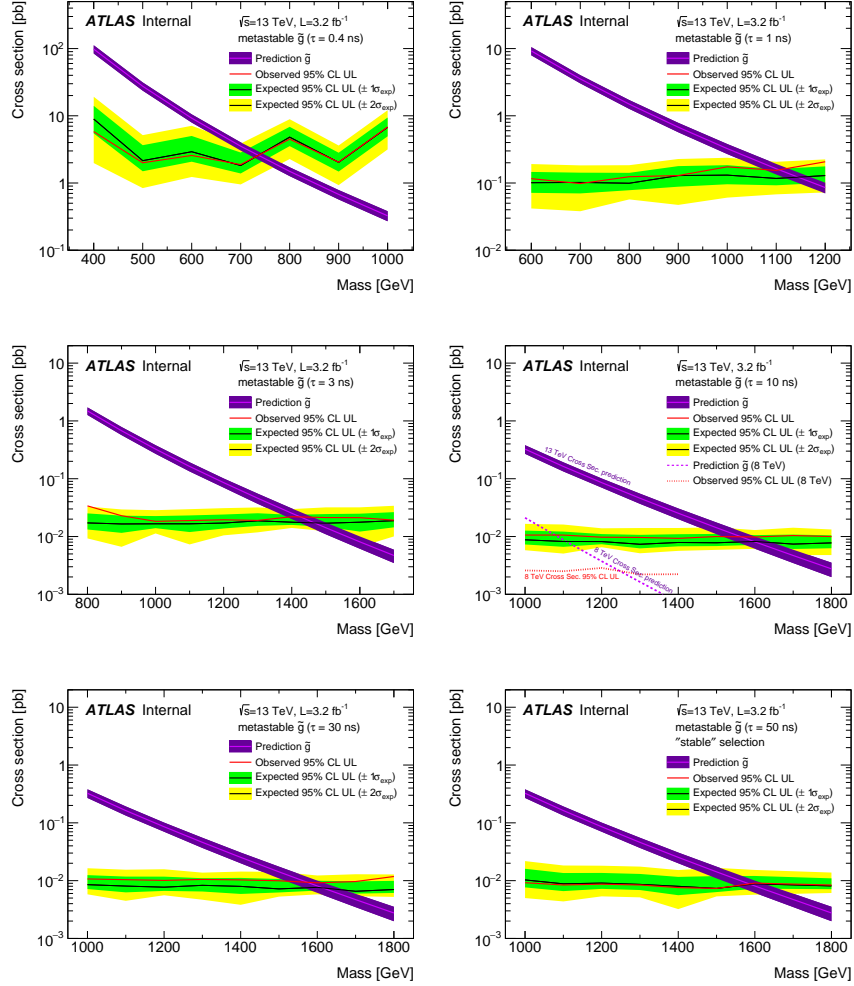


Figure 54: The observed and expected cross section limits as a function of mass for each generated lifetime. The predicted cross section values for the corresponding signals are included.

2188 sections. These mass limits range from only 740 GeV at the lowest lifetimes con-
 2189 sidered, where the selection efficiency is very low, to up to 1580 GeV at 30 ns
 2190 where the selection efficiency is maximized. The observed and expected mass
 2191 limits for each lifetime point are detailed in Table 12, which also lists which se-
 2192 lection region was used for each lifetime. These excluded range of masses as a
 2193 function of lifetime is also shown in Figure 55. The Run 1 limits are included for
 2194 comparison; the limits have increased by about 200 GeV on average. The search
 2195 has also improved since the previous incarnation from Run 1 in optimizing the
 2196 region between 30 GeV and detector-stable lifetimes by introducing the second
 2197 signal region. The definition of the stable region prevents the significant drop
 2198 in mass limit that occurred above 30 GeV in the Run 1 analysis.

Selection	τ [ns]	$M_{\text{obs}} > [\text{GeV}]$	$M_{\text{exp}} > [\text{GeV}]$
Metastable	0.4	740	730
"	1.0	1110	1150
"	3.0	1430	1470
"	10	1570	1600
"	30	1580	1620
Stable	50	1590	1590
"	stable	1570	1580

Table 12: The observed and expected 95% CL lower limit on mass for gluino R-Hadrons for each considered lifetime.

2199 13.5 CONTEXT FOR LONG-LIVED SEARCHES

2200 This search plays an important role in the current, combined [ATLAS](#) search for
 2201 long lived particles. The mass limits provided by various [ATLAS](#) searches for
 2202 long-lived gluino R-Hadrons can be seen in Figure 56. This search provides the
 2203 most competitive limit for lifetimes between 3 ns up through very long lifetimes,
 2204 where it is still competitive with dedicated searches for stable particles. The lim-
 2205 its placed on gluino production are very similar to the limits on promptly decay-
 2206 ing models.

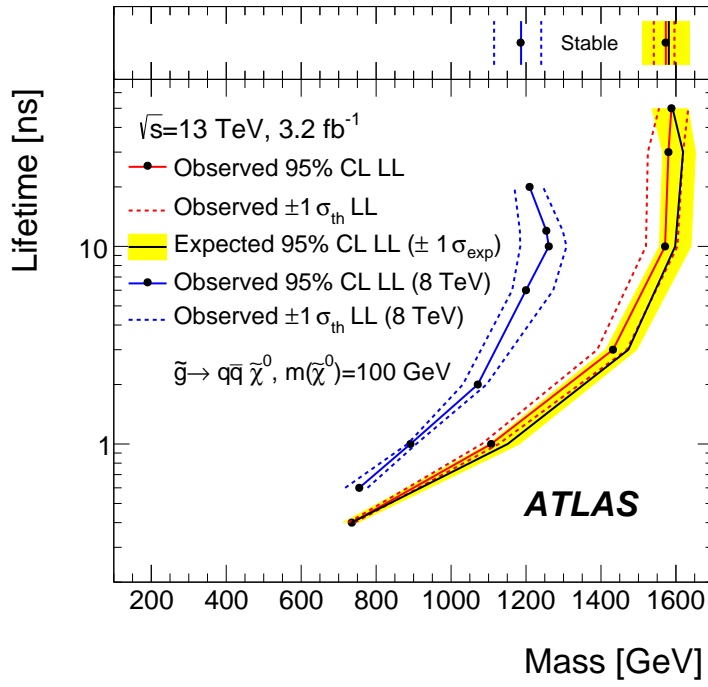


Figure 55: The excluded range of masses as a function of gluino lifetime. The expected lower limit (LL), with its experimental $\pm 1\sigma$ band, is given with respect to the nominal theoretical cross-section. The observed 95% LL obtained at $\sqrt{s} = 8 \text{ TeV}$ [61] is also shown for comparison.

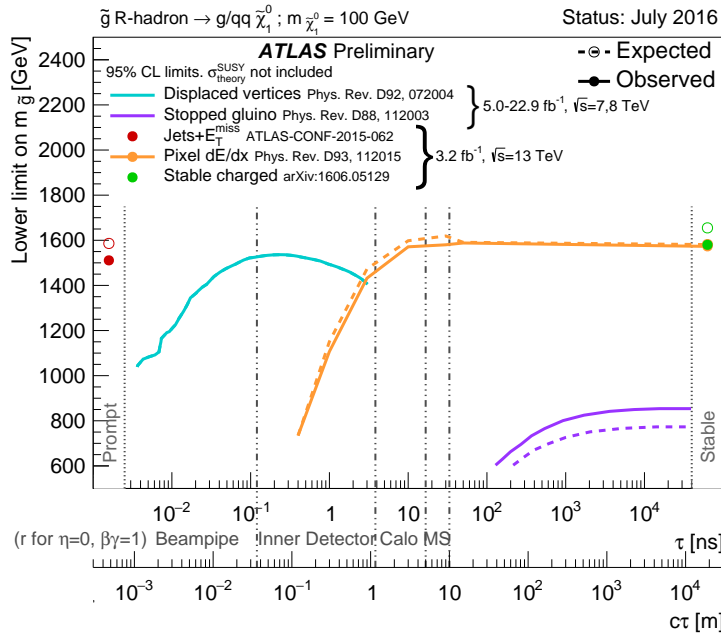


Figure 56: The constraints on the gluino mass as a function of lifetime for a split-supersymmetry model with the gluino R-Hadrons decaying into a gluon or light quarks and a neutralino with mass of 100 GeV. The solid lines indicate the observed limits, while the dashed lines indicate the expected limits. The area below the curves is excluded. The dots represent results for which the particle is assumed to be prompt or stable.

2207

PART VI

2208

CONCLUSIONS

2209

You can put some informational part preamble text here.

14

2210

2211 SUMMARY AND OUTLOOK

2212 14.1 SUMMARY

2213 14.2 OUTLOOK

2214

PART VII

2215

APPENDIX

2216

A

2217

2218 INELASTIC CROSS SECTION

B

2219

2220 EXPANDED R-HADRON YIELDS AND LIMITS

$m(\tilde{g})$ [GeV]	Left Extremum [GeV]	Right Extremum [GeV]
1000	682	1387
1100	763	1478
1200	801	1606
1300	809	1841
1400	861	2011
1500	920	2032
1600	952	2173
1800	1017	2422

Table 13: The left and right extremum of the mass window for each generated mass point with a 50 ns lifetime.

$m(\tilde{g})$ [GeV]	Left Extremum [GeV]	Right Extremum [GeV]
1000	689	1321
1100	746	1513
1200	788	1670
1300	860	1734
1400	833	1925
1500	852	2048
1600	833	2283
1700	946	2379
1800	869	2505

Table 14: The left and right extremum of the mass window for each generated mass point with a 30 ns lifetime.

$m(\tilde{g})$ [GeV]	Left Extremum [GeV]	Right Extremum [GeV]
1000	655	1349
1100	734	1455
1200	712	1631
1300	792	1737
1400	717	1926
1500	815	2117
1600	824	2122
1700	900	2274
1800	919	2344

Table 15: The left and right extremum of the mass window for each generated mass point with a 10 ns lifetime.

$m(\tilde{g})$ [GeV]	Left Extremum [GeV]	Right Extremum [GeV]
800	531	1065
900	576	1165
1000	610	1345
1100	635	1432
1200	663	1563
1300	620	1667
1400	742	1727
1500	761	1937
1600	573	2000
1700	621	2182

Table 16: The left and right extremum of the mass window used for each generated mass point with a lifetime of 3 ns.

$m(\tilde{g})$ [GeV]	Left Extremum [GeV]	Right Extremum [GeV]
600	411	758
700	385	876
800	486	970
900	406	987
1000	408	1136
1100	555	1196
1200	516	1378

Table 17: The left and right extremum of the mass window used for each mass point with a lifetime of 1 ns.

$m(\tilde{g})$ [GeV]	Left Extremum [GeV]	Right Extremum [GeV]
400	204	510
500	295	639
600	288	702
700	323	701
800	190	771
900	277	677
1000	249	688

Table 18: The left and right extremum of the mass window for each generated mass point with a lifetime of 0.4 ns.

$m(\tilde{g})$ [GeV]	Left Extremum [GeV]	Right Extremum [GeV]
800	627	1053
1000	726	1277
1200	857	1584
1400	924	1937
1600	993	2308
1800	1004	2554

Table 19: The left and right extremum of the mass window used for each generated stable mass point.

$m(\tilde{g})$ [GeV]	Expected Signal	Expected Background	Observed Data
1000	131.18 ± 6.35	1.803 ± 0.081	1.0 ± 1.0
1100	71.11 ± 3.35	1.409 ± 0.069	1.0 ± 1.0
1200	37.18 ± 1.75	1.310 ± 0.066	1.0 ± 1.0
1300	20.76 ± 0.95	1.431 ± 0.069	1.0 ± 1.0
1400	12.63 ± 0.57	1.273 ± 0.065	1.0 ± 1.0
1500	6.57 ± 0.29	1.115 ± 0.059	1.0 ± 1.0
1600	3.56 ± 0.16	1.041 ± 0.057	1.0 ± 1.0
1800	1.27 ± 0.05	0.918 ± 0.053	1.0 ± 1.0

Table 20: The expected number of signal events, the expected number of background events, and the observed number of events in data with their respective statistical errors within the respective mass window for each generated mass point with a lifetime of 50 ns.

$m(\tilde{g})$ [GeV]	Expected Signal	Expected Background	Observed Data
1000	144.65 ± 6.34	1.328 ± 0.063	2.0 ± 1.4
1100	75.28 ± 3.27	1.255 ± 0.060	2.0 ± 1.4
1200	40.51 ± 1.75	1.193 ± 0.058	2.0 ± 1.4
1300	20.91 ± 0.93	0.997 ± 0.051	2.0 ± 1.4
1400	11.97 ± 0.51	1.131 ± 0.056	2.0 ± 1.4
1500	6.81 ± 0.28	1.111 ± 0.055	2.0 ± 1.4
1600	4.19 ± 0.16	1.193 ± 0.058	2.0 ± 1.4
1700	2.42 ± 0.09	0.963 ± 0.050	2.0 ± 1.4
1800	1.46 ± 0.05	1.138 ± 0.056	3.0 ± 1.7

Table 21: The expected number of signal events, the expected number of background events, and the observed number of events in data with their respective statistical errors within the respective mass window for each generated mass point with a lifetime of 30 ns.

$m(\tilde{g})$ [GeV]	Expected Signal	Expected Background	Observed Data
1000	144.48 ± 5.14	1.499 ± 0.069	2.0 ± 1.4
1100	73.19 ± 2.61	1.260 ± 0.060	2.0 ± 1.4
1200	41.54 ± 1.41	1.456 ± 0.067	2.0 ± 1.4
1300	22.58 ± 0.77	1.201 ± 0.058	2.0 ± 1.4
1400	12.70 ± 0.42	1.558 ± 0.071	2.0 ± 1.4
1500	6.73 ± 0.24	1.237 ± 0.060	2.0 ± 1.4
1600	3.90 ± 0.13	1.201 ± 0.058	2.0 ± 1.4
1700	2.27 ± 0.07	1.027 ± 0.052	2.0 ± 1.4
1800	1.34 ± 0.04	1.019 ± 0.052	2.0 ± 1.4

Table 22: The expected number of signal events, the expected number of background events, and the observed number of events in data with their respective statistical errors within the respective mass window for each generated mass point with a lifetime of 10 ns.

$m(\tilde{g})$ [GeV]	Expected Signal	Expected Background	Observed Data
800	362.97 ± 14.68	1.841 ± 0.080	5.0 ± 2.2
900	169.20 ± 6.69	1.710 ± 0.076	3.0 ± 1.7
1000	84.78 ± 3.23	1.727 ± 0.076	2.0 ± 1.4
1100	40.06 ± 1.60	1.679 ± 0.075	2.0 ± 1.4
1200	20.06 ± 0.81	1.598 ± 0.072	2.0 ± 1.4
1300	10.76 ± 0.43	1.851 ± 0.080	2.0 ± 1.4
1400	5.52 ± 0.22	1.374 ± 0.064	2.0 ± 1.4
1500	3.16 ± 0.13	1.355 ± 0.064	2.0 ± 1.4
1600	2.13 ± 0.11	2.235 ± 0.093	3.0 ± 1.7
1700	1.10 ± 0.06	1.995 ± 0.085	2.0 ± 1.4

Table 23: The expected number of signal events, the expected number of background events, and the observed number of events in data with their respective statistical errors within the respective mass window for each generated mass point with a lifetime of 3 ns.

$m(\tilde{g})$ [GeV]	Expected Signal	Expected Background	Observed Data
600	431.80 ± 36.60	2.418 ± 0.099	3.0 ± 1.7
700	192.77 ± 15.28	3.267 ± 0.126	3.0 ± 1.7
800	69.63 ± 5.90	2.125 ± 0.089	3.0 ± 1.7
900	28.91 ± 2.59	3.114 ± 0.121	3.0 ± 1.7
1000	13.64 ± 1.22	3.359 ± 0.129	5.0 ± 2.2
1100	6.13 ± 0.57	1.879 ± 0.081	3.0 ± 1.7
1200	3.24 ± 0.30	2.387 ± 0.098	5.0 ± 2.2

Table 24: The expected number of signal events, the expected number of background events, and the observed number of events in data with their respective statistical errors within the respective mass window for each generated mass point with a lifetime of 1 ns.

$m(\tilde{g})$ [GeV]	Expected Signal	Expected Background	Observed Data
400	181.71 ± 75.59	6.780 ± 0.238	4.0 ± 2.0
500	103.88 ± 30.05	4.310 ± 0.160	4.0 ± 2.0
600	28.34 ± 9.34	4.868 ± 0.177	4.0 ± 2.0
700	13.62 ± 4.00	3.908 ± 0.147	4.0 ± 2.0
800	2.75 ± 1.15	9.001 ± 0.308	8.0 ± 2.8
900	2.25 ± 0.71	5.045 ± 0.183	5.0 ± 2.2
1000	0.34 ± 0.19	6.026 ± 0.214	6.0 ± 2.4

Table 25: The expected number of signal events, the expected number of background events, and the observed number of events in data with their respective statistical errors within the respective mass window for each generated mass point with a lifetime of p4 ns.

$m(\tilde{g})$ [GeV]	Expected Signal	Expected Background	Observed Data
800	462.83 ± 14.86	1.764 ± 0.080	2.0 ± 1.4
1000	108.73 ± 3.38	1.458 ± 0.070	1.0 ± 1.0
1200	31.74 ± 0.95	1.137 ± 0.060	1.0 ± 1.0
1400	10.22 ± 0.29	1.058 ± 0.058	1.0 ± 1.0
1600	3.07 ± 0.09	0.947 ± 0.054	1.0 ± 1.0
1800	1.08 ± 0.05	0.940 ± 0.054	1.0 ± 1.0

Table 26: The expected number of signal events, the expected number of background events, and the observed number of events in data with their respective statistical errors within the respective mass window for each generated stable mass point

2221 BIBLIOGRAPHY

- 2222 [1] Lyndon Evans and Philip Bryant. "LHC Machine". In: *JINST* 3 (2008), S08001.
2223 doi: [10.1088/1748-0221/3/08/S08001](https://doi.org/10.1088/1748-0221/3/08/S08001).
- 2224 [2] C Lefevre. "LHC: the guide (English version). Guide du LHC (version anglaise)".
2225 2009. URL: <https://cds.cern.ch/record/1165534>.
- 2226 [3] ATLAS Collaboration. "The ATLAS Experiment at the CERN Large Hadron
2227 Collider". In: *JINST* 3 (2008), S08003. doi: [10.1088/1748-0221/3/08/S08003](https://doi.org/10.1088/1748-0221/3/08/S08003).
- 2229 [4] S. Chatrchyan et al. "The CMS experiment at the CERN LHC". In: *JINST*
2230 3 (2008), S08004. doi: [10.1088/1748-0221/3/08/S08004](https://doi.org/10.1088/1748-0221/3/08/S08004).
- 2231 [5] A. Augusto Alves Jr. et al. "The LHCb Detector at the LHC". In: *JINST* 3
2232 (2008), S08005. doi: [10.1088/1748-0221/3/08/S08005](https://doi.org/10.1088/1748-0221/3/08/S08005).
- 2233 [6] K. Aamodt et al. "The ALICE experiment at the CERN LHC". In: *JINST* 3
2234 (2008), S08002. doi: [10.1088/1748-0221/3/08/S08002](https://doi.org/10.1088/1748-0221/3/08/S08002).
- 2235 [7] S. Agostinelli et al. "GEANT4: A simulation toolkit". In: *Nucl. Instrum. Meth.*
2236 A 506 (2003), pp. 250–303. doi: [10.1016/S0168-9002\(03\)01368-8](https://doi.org/10.1016/S0168-9002(03)01368-8).
- 2237 [8] ATLAS Collaboration. "A study of the material in the ATLAS inner de-
2238 tector using secondary hadronic interactions". In: *JINST* 7 (2012), P01013.
2239 doi: [10.1088/1748-0221/7/01/P01013](https://doi.org/10.1088/1748-0221/7/01/P01013). arXiv: [1110.6191 \[hep-ex\]](https://arxiv.org/abs/1110.6191).
2240 PERF-2011-08.
- 2241 [9] ATLAS Collaboration. "Electron and photon energy calibration with the
2242 ATLAS detector using LHC Run 1 data". In: *Eur. Phys. J. C* 74 (2014), p. 3071.
2243 doi: [10.1140/epjc/s10052-014-3071-4](https://doi.org/10.1140/epjc/s10052-014-3071-4). arXiv: [1407.5063](https://arxiv.org/abs/1407.5063)
2244 [hep-ex]. PERF-2013-05.
- 2245 [10] ATLAS Collaboration. "A measurement of the calorimeter response to sin-
2246 ggle hadrons and determination of the jet energy scale uncertainty using
2247 LHC Run-1 pp -collision data with the ATLAS detector". In: (2016). arXiv:
2248 [1607.08842 \[hep-ex\]](https://arxiv.org/abs/1607.08842). PERF-2015-05.
- 2249 [11] ATLAS Collaboration. "Single hadron response measurement and calorime-
2250 ter jet energy scale uncertainty with the ATLAS detector at the LHC". In:
2251 *Eur. Phys. J. C* 73 (2013), p. 2305. doi: [10.1140/epjc/s10052-013-2305-1](https://doi.org/10.1140/epjc/s10052-013-2305-1). arXiv: [1203.1302 \[hep-ex\]](https://arxiv.org/abs/1203.1302). PERF-2011-05.
- 2253 [12] ATLAS Collaboration. "The ATLAS Simulation Infrastructure". In: *Eur.*
2254 *Phys. J. C* 70 (2010), p. 823. doi: [10.1140/epjc/s10052-010-1429-9](https://doi.org/10.1140/epjc/s10052-010-1429-9).
2255 arXiv: [1005.4568 \[hep-ex\]](https://arxiv.org/abs/1005.4568). SOFT-2010-01.
- 2256 [13] T. Sjöstrand, S. Mrenna, and P. Skands. "A Brief Introduction to PYTHIA
2257 8.1". In: *Comput. Phys. Commun.* 178 (2008), pp. 852–867. doi: [10.1016/j.cpc.2008.01.036](https://doi.org/10.1016/j.cpc.2008.01.036). arXiv: [0710.3820](https://arxiv.org/abs/0710.3820).

- 2259 [14] ATLAS Collaboration. *Summary of ATLAS Pythia 8 tunes*. ATL-PHYS-PUB-
 2260 2012-003. 2012. URL: <http://cds.cern.ch/record/1474107>.
- 2261 [15] A.D. Martin, W.J. Stirling, R.S. Thorne, and G. Watt. “Parton distributions
 2262 for the LHC”. In: *Eur. Phys. J. C* 63 (2009). Figures from the MSTW Website,
 2263 pp. 189–285. doi: [10.1140/epjc/s10052-009-1072-5](https://doi.org/10.1140/epjc/s10052-009-1072-5). arXiv: [0901.0002](https://arxiv.org/abs/0901.0002).
- 2264 [16] A. Sherstnev and R.S. Thorne. “Parton Distributions for LO Generators”.
 2265 In: *Eur. Phys. J. C* 55 (2008), pp. 553–575. doi: [10.1140/epjc/s10052-008-0610-x](https://doi.org/10.1140/epjc/s10052-008-0610-x). arXiv: [0711.2473](https://arxiv.org/abs/0711.2473).
- 2266 [17] A. Ribon et al. *Status of Geant4 hadronic physics for the simulation of LHC*
 2267 *experiments at the start of LHC physics program*. CERN-LCGAPP-2010-02.
 2268 2010. URL: <http://lcgapp.cern.ch/project/docs/noteStatusHadronic2010.pdf>.
- 2269 [18] M. P. Guthrie, R. G. Alsmiller, and H. W. Bertini. “Calculation of the cap-
 2270 ture of negative pions in light elements and comparison with experiments
 2271 pertaining to cancer radiotherapy”. In: *Nucl. Instrum. Meth.* 66 (1968), pp. 29–
 2272 36. doi: [10.1016/0029-554X\(68\)90054-2](https://doi.org/10.1016/0029-554X(68)90054-2).
- 2273 [19] H. W. Bertini and P. Guthrie. “News item results from medium-energy
 2274 intranuclear-cascade calculation”. In: *Nucl. Instr. and Meth. A* 169 (1971),
 2275 p. 670. doi: [10.1016/0375-9474\(71\)90710-X](https://doi.org/10.1016/0375-9474(71)90710-X).
- 2276 [20] V.A. Karmanov. “Light Front Wave Function of Relativistic Composite
 2277 System in Explicitly Solvable Model”. In: *Nucl. Phys. B* 166 (1980), p. 378.
 2278 doi: [10.1016/0550-3213\(80\)90204-7](https://doi.org/10.1016/0550-3213(80)90204-7).
- 2279 [21] H. S. Fesefeldt. *GHEISHA program*. Pitha-85-02, Aachen. 1985.
- 2280 [22] G. Folger and J.P. Wellisch. “String parton models in Geant4”. In: (2003).
 2281 arXiv: [nucl-th/0306007](https://arxiv.org/abs/nucl-th/0306007).
- 2282 [23] N. S. Amelin et al. “Transverse flow and collectivity in ultrarelativistic
 2283 heavy-ion collisions”. In: *Phys. Rev. Lett.* 67 (1991), p. 1523. doi: [10.1103/PhysRevLett.67.1523](https://doi.org/10.1103/PhysRevLett.67.1523).
- 2284 [24] N. S. Amelin et al. “Collectivity in ultrarelativistic heavy ion collisions”. In:
 2285 *Nucl. Phys. A* 544 (1992), p. 463. doi: [10.1016/0375-9474\(92\)90598-E](https://doi.org/10.1016/0375-9474(92)90598-E).
- 2286 [25] L. V. Bravina et al. “Fluid dynamics and Quark Gluon string model - What
 2287 we can expect for Au+Au collisions at 11.6 AGeV/c”. In: *Nucl. Phys. A* 566
 2288 (1994), p. 461. doi: [10.1016/0375-9474\(94\)90669-6](https://doi.org/10.1016/0375-9474(94)90669-6).
- 2289 [26] L. V. Bravin et al. “Scaling violation of transverse flow in heavy ion colli-
 2290 sions at AGS energies”. In: *Phys. Lett. B* 344 (1995), p. 49. doi: [10.1016/0370-2693\(94\)01560-Y](https://doi.org/10.1016/0370-2693(94)01560-Y).
- 2291 [27] B. Andersson et al. “A model for low-pT hadronic reactions with general-
 2292 izations to hadron-nucleus and nucleus-nucleus collisions”. In: *Nucl. Phys.*
 2293 *B* 281 (1987), p. 289. doi: [10.1016/0550-3213\(87\)90257-4](https://doi.org/10.1016/0550-3213(87)90257-4).

- [28] B. Andersson, A. Tai, and B.-H. Sa. “Final state interactions in the (nuclear) FRITIOF string interaction scenario”. In: *Z. Phys. C* 70 (1996), pp. 499–506. doi: [10.1007/s002880050127](https://doi.org/10.1007/s002880050127).
- [29] B. Nilsson-Almqvist and E. Stenlund. “Interactions Between Hadrons and Nuclei: The Lund Monte Carlo, Fritiof Version 1.6”. In: *Comput. Phys. Commun.* 43 (1987), p. 387. doi: [10.1016/0010-4655\(87\)90056-7](https://doi.org/10.1016/0010-4655(87)90056-7).
- [30] B. Ganhuyag and V. Uzhinsky. “Modified FRITIOF code: Negative charged particle production in high energy nucleus nucleus interactions”. In: *Czech. J. Phys.* 47 (1997), pp. 913–918. doi: [10.1023/A:1021296114786](https://doi.org/10.1023/A:1021296114786).
- [31] ATLAS Collaboration. “Topological cell clustering in the ATLAS calorimeters and its performance in LHC Run 1”. In: (2016). arXiv: [1603.02934 \[hep-ex\]](https://arxiv.org/abs/1603.02934).
- [32] Peter Speckmayer. “Energy Measurement of Hadrons with the CERN ATLAS Calorimeter”. Presented on 18 Jun 2008. PhD thesis. Vienna: Vienna, Tech. U., 2008. url: <http://cds.cern.ch/record/1112036>.
- [33] CMS Collaboration. “The CMS barrel calorimeter response to particle beams from 2 to 350 GeV/c”. In: *Eur. Phys. J. C* 60.3 (2009). doi: [10.1140/epjc/s10052-009-0959-5](https://doi.org/10.1140/epjc/s10052-009-0959-5).
- [34] J. Beringer et al. (Particle Data Group). “Review of Particle Physics”. In: *Chin. Phys. C* 38 (2014), p. 090001. url: <http://pdg.lbl.gov>.
- [35] P. Adragna et al. “Measurement of Pion and Proton Response and Longitudinal Shower Profiles up to 20 Nuclear Interaction Lengths with the ATLAS Tile Calorimeter”. In: *Nucl. Instrum. Meth. A* 615 (2010), pp. 158–181. doi: [10.1016/j.nima.2010.01.037](https://doi.org/10.1016/j.nima.2010.01.037).
- [36] ATLAS Collaboration. “Jet energy measurement and its systematic uncertainty in proton–proton collisions at $\sqrt{s} = 7$ TeV with the ATLAS detector”. In: *Eur. Phys. J. C* 75 (2015), p. 17. doi: [10.1140/epjc/s10052-014-3190-y](https://doi.org/10.1140/epjc/s10052-014-3190-y). arXiv: [1406.0076 \[hep-ex\]](https://arxiv.org/abs/1406.0076). PERF-2012-01.
- [37] Hung-Liang Lai, Marco Guzzi, Joey Huston, Zhao Li, Pavel M. Nadolsky, et al. “New parton distributions for collider physics”. In: *Phys. Rev. D* 82 (2010), p. 074024. doi: [10.1103/PhysRevD.82.074024](https://doi.org/10.1103/PhysRevD.82.074024). arXiv: [1007.2241 \[hep-ph\]](https://arxiv.org/abs/1007.2241).
- [38] E. Abat et al. “Study of energy response and resolution of the ATLAS barrel calorimeter to hadrons of energies from 20 to 350 GeV”. In: *Nucl. Instrum. Meth. A* 621.1-3 (2010), pp. 134 –150. doi: <http://dx.doi.org/10.1016/j.nima.2010.04.054>.
- [39] ATLAS Collaboration. “Jet energy measurement with the ATLAS detector in proton–proton collisions at $\sqrt{s} = 7$ TeV”. In: *Eur. Phys. J. C* 73 (2013), p. 2304. doi: [10.1140/epjc/s10052-013-2304-2](https://doi.org/10.1140/epjc/s10052-013-2304-2). arXiv: [1112.6426 \[hep-ex\]](https://arxiv.org/abs/1112.6426). PERF-2011-03.
- [40] Nausheen R. Shah and Carlos E. M. Wagner. “Gravitons and dark matter in universal extra dimensions”. In: *Phys. Rev. D* 74 (2006), p. 104008. doi: [10.1103/PhysRevD.74.104008](https://doi.org/10.1103/PhysRevD.74.104008). arXiv: [hep-ph/0608140 \[hep-ph\]](https://arxiv.org/abs/hep-ph/0608140).

- 2343 [41] Jonathan L. Feng, Arvind Rajaraman, and Fumihiro Takayama. “Graviton
 2344 cosmology in universal extra dimensions”. In: *Phys. Rev.* D68 (2003), p. 085018.
 2345 doi: [10.1103/PhysRevD.68.085018](https://doi.org/10.1103/PhysRevD.68.085018). arXiv: [hep-ph/0307375](https://arxiv.org/abs/hep-ph/0307375)
 2346 [[hep-ph](#)].
- 2347 [42] Paul H. Frampton and Pham Quang Hung. “Long-lived quarks?” In: *Phys.
 2348 Rev. D* 58 (5 1998), p. 057704. doi: [10.1103/PhysRevD.58.057704](https://doi.org/10.1103/PhysRevD.58.057704).
 2349 url: [http://link.aps.org/doi/10.1103/PhysRevD.58.
 2350 057704](http://link.aps.org/doi/10.1103/PhysRevD.58.057704).
- 2351 [43] C. Friberg, E. Norrbin, and T. Sjostrand. “QCD aspects of leptoquark pro-
 2352 duction at HERA”. In: *Phys. Lett.* B403 (1997), pp. 329–334. doi: [10.1016/S0370-2693\(97\)00543-1](https://doi.org/10.1016/S0370-2693(97)00543-1). arXiv: [hep-ph/9704214](https://arxiv.org/abs/hep-ph/9704214) [[hep-ph](#)].
- 2354 [44] Herbert K. Dreiner. “An introduction to explicit R-parity violation”. In:
 2355 (1997). arXiv: [hep-ph/9707435](https://arxiv.org/abs/hep-ph/9707435).
- 2356 [45] Edmond L. Berger and Zack Sullivan. “Lower limits on R-parity-violating
 2357 couplings in supersymmetry”. In: *Phys. Rev. Lett.* 92 (2004), p. 201801. doi:
 2358 [10.1103/PhysRevLett.92.201801](https://doi.org/10.1103/PhysRevLett.92.201801). arXiv: [hep-ph/0310001](https://arxiv.org/abs/hep-ph/0310001).
- 2359 [46] R. Barbieri, C. Berat, M. Besancon, M. Chemtob, A. Deandrea, et al. “R-
 2360 parity violating supersymmetry”. In: *Phys. Rept.* 420 (2005), p. 1. doi: [10.1016/j.physrep.2005.08.006](https://doi.org/10.1016/j.physrep.2005.08.006). arXiv: [hep-ph/0406039](https://arxiv.org/abs/hep-ph/0406039).
- 2362 [47] M. Fairbairn et al. “Stable massive particles at colliders”. In: *Phys. Rept.* 438
 2363 (2007), p. 1. doi: [10.1016/j.physrep.2006.10.002](https://doi.org/10.1016/j.physrep.2006.10.002). arXiv: [hep-ph/0611040](https://arxiv.org/abs/hep-ph/0611040).
- 2365 [48] Christopher F. Kolda. “Gauge-mediated supersymmetry breaking: Intro-
 2366 duction, review and update”. In: *Nucl. Phys. Proc. Suppl.* 62 (1998), p. 266.
 2367 doi: [10.1016/S0920-5632\(97\)00667-1](https://doi.org/10.1016/S0920-5632(97)00667-1). arXiv: [hep-ph/9707450](https://arxiv.org/abs/hep-ph/9707450).
- 2368 [49] Howard Baer, Kingman Cheung, and John F. Gunion. “A Heavy gluino as
 2369 the lightest supersymmetric particle”. In: *Phys. Rev. D* 59 (1999), p. 075002.
 2370 doi: [10.1103/PhysRevD.59.075002](https://doi.org/10.1103/PhysRevD.59.075002). arXiv: [hep-ph/9806361](https://arxiv.org/abs/hep-ph/9806361).
- 2371 [50] S. James Gates Jr. and Oleg Lebedev. “Searching for supersymmetry in
 2372 hadrons”. In: *Phys. Lett. B* 477 (2000), p. 216. doi: [10.1016/S0370-2693\(00\)00172-6](https://doi.org/10.1016/S0370-2693(00)00172-6). arXiv: [hep-ph/9912362](https://arxiv.org/abs/hep-ph/9912362).
- 2374 [51] G. F. Giudice and A. Romanino. “Split supersymmetry”. In: *Nucl. Phys. B*
 2375 699 (2004), p. 65. doi: [10.1016/j.nuclphysb.2004.11.048](https://doi.org/10.1016/j.nuclphysb.2004.11.048). arXiv:
 2376 [hep-ph/0406088](https://arxiv.org/abs/hep-ph/0406088).
- 2377 [52] N. Arkani-Hamed, S. Dimopoulos, G. F. Giudice, and A. Romanino. “As-
 2378 pects of split supersymmetry”. In: *Nucl. Phys. B* 709 (2005), p. 3. doi: [10.1016/j.nuclphysb.2004.12.026](https://doi.org/10.1016/j.nuclphysb.2004.12.026). arXiv: [hep-ph/0409232](https://arxiv.org/abs/hep-ph/0409232).
- 2380 [53] Glennys R. Farrar and Pierre Fayet. “Phenomenology of the Production,
 2381 Decay, and Detection of New Hadronic States Associated with Supersym-
 2382 metry”. In: *Phys. Lett.* B76 (1978), pp. 575–579. doi: [10.1016/0370-2693\(78\)90858-4](https://doi.org/10.1016/0370-2693(78)90858-4).

- 2384 [54] A. C. Kraan, J. B. Hansen, and P. Nevski. “Discovery potential of R-hadrons
 2385 with the ATLAS detector”. In: *Eur. Phys. J.* C49 (2007), pp. 623–640. doi:
 2386 [10.1140/epjc/s10052-006-0162-x](https://doi.org/10.1140/epjc/s10052-006-0162-x). arXiv: [hep-ex/0511014](https://arxiv.org/abs/hep-ex/0511014)
 2387 [[hep-ex](#)].
- 2388 [55] K. A. Olive et al. “Review of Particle Physics”. In: *Chin. Phys.* C38 (2014),
 2389 p. 090001. doi: [10.1088/1674-1137/38/9/090001](https://doi.org/10.1088/1674-1137/38/9/090001).
- 2390 [56] Rasmus Mackeprang and David Milstead. “An Updated Description of
 2391 Heavy-Hadron Interactions in GEANT-4”. In: *Eur. Phys. J.* C66 (2010), pp. 493–
 2392 501. doi: [10.1140/epjc/s10052-010-1262-1](https://doi.org/10.1140/epjc/s10052-010-1262-1). arXiv: [0908.1868](https://arxiv.org/abs/0908.1868)
 2393 [[hep-ph](#)].
- 2394 [57] ATLAS Collaboration. “Search for massive, long-lived particles using mul-
 2395 titrack displaced vertices or displaced lepton pairs in pp collisions at $\sqrt{s} =$
 2396 8 TeV with the ATLAS detector”. In: *Phys. Rev. D* 92 (2015), p. 072004.
 2397 doi: [10.1103/PhysRevD.92.072004](https://doi.org/10.1103/PhysRevD.92.072004). arXiv: [1504.05162](https://arxiv.org/abs/1504.05162) [[hep-ex](#)].
 2398 SUSY-2014-02.
- 2399 [58] ATLAS Collaboration. “Search for charginos nearly mass degenerate with
 2400 the lightest neutralino based on a disappearing-track signature in pp col-
 2401 lisions at $\sqrt{s} = 8$ TeV with the ATLAS detector”. In: *Phys. Rev. D* 88 (2013),
 2402 p. 112006. doi: [10.1103/PhysRevD.88.112006](https://doi.org/10.1103/PhysRevD.88.112006). arXiv: [1310.3675](https://arxiv.org/abs/1310.3675)
 2403 [[hep-ex](#)]. SUSY-2013-01.
- 2404 [59] ATLAS Collaboration. “Searches for heavy long-lived sleptons and R-Hadrons
 2405 with the ATLAS detector in pp collisions at $\sqrt{s} = 7$ TeV”. In: *Phys. Lett. B*
 2406 720 (2013), p. 277. doi: [10.1016/j.physletb.2013.02.015](https://doi.org/10.1016/j.physletb.2013.02.015). arXiv:
 2407 [1211.1597](https://arxiv.org/abs/1211.1597) [[hep-ex](#)]. SUSY-2012-01.
- 2408 [60] ATLAS Collaboration. “Searches for heavy long-lived charged particles
 2409 with the ATLAS detector in proton–proton collisions at $\sqrt{s} = 8$ TeV”.
 2410 In: *JHEP* 01 (2015), p. 068. doi: [10.1007/JHEP01\(2015\)068](https://doi.org/10.1007/JHEP01(2015)068). arXiv:
 2411 [1411.6795](https://arxiv.org/abs/1411.6795) [[hep-ex](#)]. SUSY-2013-22.
- 2412 [61] ATLAS Collaboration. “Search for metastable heavy charged particles with
 2413 large ionisation energy loss in pp collisions at $\sqrt{s} = 8$ TeV using the AT-
 2414 LAS experiment”. In: *Eur. Phys. J.* C 75 (2015), p. 407. doi: [10.1140/epjc/s10052-015-3609-0](https://doi.org/10.1140/epjc/s10052-015-3609-0). arXiv: [1506.05332](https://arxiv.org/abs/1506.05332) [[hep-ex](#)]. SUSY-
 2415 2014-09.
- 2416 [62] ATLAS Collaboration. “Search for heavy long-lived charged R -hadrons
 2417 with the ATLAS detector in 3.2 fb^{-1} of proton–proton collision data at
 2418 $\sqrt{s} = 13$ TeV”. In: *Phys. Lett.* B760 (2016), pp. 647–665. doi: [10.1016/j.physletb.2016.07.042](https://doi.org/10.1016/j.physletb.2016.07.042). arXiv: [1606.05129](https://arxiv.org/abs/1606.05129) [[hep-ex](#)].
- 2419 [63] Torbjorn Sjöstrand, Stephen Mrenna, and Peter Skands. “PYTHIA 6.4 Physics
 2420 and Manual”. In: *JHEP* 0605 (2006), p. 026. doi: [10.1088/1126-6708/2006/05/026](https://doi.org/10.1088/1126-6708/2006/05/026). arXiv: [hep-ph/0603175](https://arxiv.org/abs/hep-ph/0603175).
- 2421 [64] *Further ATLAS tunes of PYTHIA6 and Pythia 8*. Tech. rep. ATL-PHYS-PUB-
 2422 2011-014. Geneva: CERN, 2011. URL: <https://cds.cern.ch/record/1400677>.

- [65] Aafke Christine Kraan. “Interactions of heavy stable hadronizing particles”. In: *Eur. Phys. J.* C37 (2004), pp. 91–104. doi: [10.1140/epjc/s2004-01946-6](https://doi.org/10.1140/epjc/s2004-01946-6). arXiv: [hep-ex/0404001](https://arxiv.org/abs/hep-ex/0404001) [hep-ex].
- [66] M. Fairbairn et al. “Stable massive particles at colliders”. In: *Phys. Rept.* 438 (2007), p. 1. doi: [10.1016/j.physrep.2006.10.002](https://doi.org/10.1016/j.physrep.2006.10.002). arXiv: [hep-ph/0611040](https://arxiv.org/abs/hep-ph/0611040).
- [67] W. Beenakker, R. Hopker, M. Spira, and P. M. Zerwas. “Squark and gluino production at hadron colliders”. In: *Nucl. Phys. B* 492 (1997), p. 51. doi: [10.1016/S0550-3213\(97\)00084-9](https://doi.org/10.1016/S0550-3213(97)00084-9). arXiv: [hep-ph/9610490](https://arxiv.org/abs/hep-ph/9610490).
- [68] A. Kulesza and L. Motyka. “Threshold resummation for squark-antisquark and gluino-pair production at the LHC”. In: *Phys. Rev. Lett.* 102 (2009), p. 111802. doi: [10.1103/PhysRevLett.102.111802](https://doi.org/10.1103/PhysRevLett.102.111802). arXiv: [0807.2405](https://arxiv.org/abs/0807.2405) [hep-ph].
- [69] A. Kulesza and L. Motyka. “Soft gluon resummation for the production of gluino-gluino and squark-antisquark pairs at the LHC”. In: *Phys. Rev. D* 80 (2009), p. 095004. doi: [10.1103/PhysRevD.80.095004](https://doi.org/10.1103/PhysRevD.80.095004). arXiv: [0905.4749](https://arxiv.org/abs/0905.4749) [hep-ph].
- [70] Wim Beenakker, Silja Brensing, Michael Kramer, Anna Kulesza, Eric Laenen, et al. “Soft-gluon resummation for squark and gluino hadroproduction”. In: *JHEP* 0912 (2009), p. 041. doi: [10.1088/1126-6708/2009/12/041](https://doi.org/10.1088/1126-6708/2009/12/041). arXiv: [0909.4418](https://arxiv.org/abs/0909.4418) [hep-ph].
- [71] W. Beenakker, S. Brensing, M.n Kramer, A. Kulesza, E. Laenen, et al. “Squark and Gluino Hadroproduction”. In: *Int. J. Mod. Phys. A* 26 (2011), p. 2637. doi: [10.1142/S0217751X11053560](https://doi.org/10.1142/S0217751X11053560). arXiv: [1105.1110](https://arxiv.org/abs/1105.1110) [hep-ph].
- [72] Michael Krämer et al. *Supersymmetry production cross sections in pp collisions at $\sqrt{s} = 7 \text{ TeV}$* . 2012. arXiv: [1206.2892](https://arxiv.org/abs/1206.2892) [hep-ph].
- [73] Rasmus Mackeprang and Andrea Rizzi. “Interactions of Coloured Heavy Stable Particles in Matter”. In: *Eur. Phys. J.* C50 (2007), pp. 353–362. doi: [10.1140/epjc/s10052-007-0252-4](https://doi.org/10.1140/epjc/s10052-007-0252-4). arXiv: [hep-ph/0612161](https://arxiv.org/abs/hep-ph/0612161) [hep-ph].
- [74] Rasmus Mackeprang and David Milstead. “An Updated Description of Heavy-Hadron Interactions in GEANT-4”. In: *Eur. Phys. J.* C66 (2010), pp. 493–501. doi: [10.1140/epjc/s10052-010-1262-1](https://doi.org/10.1140/epjc/s10052-010-1262-1). arXiv: [0908.1868](https://arxiv.org/abs/0908.1868) [hep-ph].
- [75] J. Alwall, R. Frederix, S. Frixione, V. Hirschi, F. Maltoni, O. Mattelaer, H. S. Shao, T. Stelzer, P. Torrielli, and M. Zaro. “The automated computation of tree-level and next-to-leading order differential cross sections, and their matching to parton shower simulations”. In: *JHEP* 07 (2014), p. 079. doi: [10.1007/JHEP07\(2014\)079](https://doi.org/10.1007/JHEP07(2014)079). arXiv: [1405.0301](https://arxiv.org/abs/1405.0301) [hep-ph].
- [76] “dE/dx measurement in the ATLAS Pixel Detector and its use for particle identification”. In: (2011).

- 2468 [77] ATLAS Collaboration. “The ATLAS Simulation Infrastructure”. In: *Eur.*
2469 *Phys. J.* C70 (2010), pp. 823–874. doi: [10.1140/epjc/s10052-010-1429-9](https://doi.org/10.1140/epjc/s10052-010-1429-9). arXiv: [1005.4568 \[physics.ins-det\]](https://arxiv.org/abs/1005.4568).
- 2471 [78] Alexander L. Read. “Presentation of search results: The CL(s) technique”.
2472 In: *J. Phys.* G28 (2002). [,11(2002)], pp. 2693–2704. doi: [10.1088/0954-3899/28/10/313](https://doi.org/10.1088/0954-3899/28/10/313).
2473

2474 DECLARATION

2475 Put your declaration here.

2476 *Berkeley, CA, September 2016*

2477 Bradley Axen

2478

2479 COLOPHON

2480

Not sure that this is necessary.